Aeronomy of Ice in the Mesosphere (AIM) Mission

Calibration and Measurement Algorithms Document (CMAD)

Signature Page

Aeronomy of Ice in the Mesosphere (AIM) **Calibration and Measurement Algorithms Document**	
Jerry Jason, Project Manager	Date
Scott Bailey, AIM Principal Investigator	Date:
Cora Randall, CIPS Principal Investigator	Date:
Mark Hervig, SOFIE Principal Investigator	Date:
By signing this document, signatories are certifying that the content herein is acceptable direction for managing the project's data and that they will ensure its implementation by those over whom they have authority.	

Change History Log		
Revision	**Effective Date**	**Description of Changes (Reference the CCR & CCB/ERB Approval Date)**
Original	4/22/2020	Original
Revision 1	11/1/2022	Updated

Aeronomy of Ice in the Mesosphere (AIM)

Calibration and Measurement Algorithms Document (CMAD)

1. Scope

AIM was the first satellite mission dedicated to the study of polar mesospheric clouds (PMCs), with the overall goal to resolve why PMCs form and why they vary [*Russell et al.*, 2009]. The AIM experiment includes three instruments: the Solar Occultation For Ice Experiment (SOFIE), the Cloud Imaging and Particle Size experiment (CIPS), and the Cosmic Dust Experiment (CDE).

1.1. Purpose

This CMAD provides a description of the CIPS, SOFIE, and CDE instruments. The scientific rational behind the experiments are described as well as how the objectives have been met through instrument design, testing, and analysis.

1.2. Contents

The following sections describe the three AIM instruments

2. The Cloud Imaging and Particle Size (CIPS) Experiment
3. The Solar Occultation For Ice Experiment (SOFIE)
4. The Cosmic Dust Experiment (CDE)

1.3. Related Documents

This section identifies other project/mission documents that contains higher level guiding requirements or that provides more detail or context (see Table 1.3).

Table 1.3. Relevant AIM Documents.

Document	Location
CIPS instrument overview	lasp.colorado.edu/aim
CIPS data product overview	lasp.colorado.edu/aim
CIPS PMC retrieval algorithm	lasp.colorado.edu/aim
CIPS Level 2 data product details	lasp.colorado.edu/aim
CIPS Level 3A data product details	lasp.colorado.edu/aim
CIPS Level 3B data product details	lasp.colorado.edu/aim
CIPS Level 3C data product details	lasp.colorado.edu/aim
CIPS Level 3D data product details	lasp.colorado.edu/aim
CIPS Level 3E data product details	lasp.colorado.edu/aim

CIPS Level 2 RAA data product details	lasp.colorado.edu/aim
SOFIE Uncertainty analysis	sofie.gats-inc.com
SOFIE_Products_V1.3.pdf	sofie.gats-inc.com
SOFIE_Level0b_to_Level1_ICD_V1.0.pdf	sofie.gats-inc.com
SOFIE_l1_netcdf_file_description_V1.0.pdf	sofie.gats-inc.com
SOFIE_l2_netcdf_file_description_V1.0.pdf	sofie.gats-inc.com
SOFIE_Level3_Product_Description_V1.0.pdf	sofie.gats-inc.com
SOFIE_Calibration_Product_Summary_V1.8.pdf	sofie.gats-inc.com
SOFIE_Electrical_Software_Interface_sdl04-040b.pdf	sofie.gats-inc.com
SOFIE_Users_Guide_sdl06-303.pdf	sofie.gats-inc.com

2. The Cloud Imaging and Particle Size (CIPS) Experiment

2.1. CIPS Overview

CIPS is a four-camera, nadir-viewing panoramic imager designed to measure solar UV radiation (265 nm wavelength) scattered from the earth's atmosphere. The field of view of each four-camera scene spans 120° × 80°, with an average effective spatial resolution in the nadir cameras of 2 km × 2.4 km, increasing to 4.5 km × 3 km at the outside corners of the fore and aft cameras. CIPS measurements enable retrievals of polar mesospheric cloud (PMC) presence and structure, along with cloud albedo, particle radius, and ice water content. They also enable inference of gravity waves (GWs) near the stratopause, via measurements of the Rayleigh albedo anomaly (RAA). The CIPS instrument is described by *McClintock et al.* [2009]. The version 4 PMC retrieval algorithm is described by *Lumpe et al.* [2013] while the version 5 PMC algorithm is described in *Carstens et al*. (in preparation). An introduction to the GW retrievals is given by *Randall et al.* [2017] and the current version of RAA data (v1.10r06) is described by *Carstens et al*. (also in preparation).

CIPS began routine measurements on May 24, 2007 and has operated flawlessly since that time. From launch until 11 February 2016 CIPS acquired images every 43 seconds only over mid to high latitudes in the summer (spring to fall equinox) hemisphere. From 12 February 2016 until 20 September 2018 CIPS images were acquired every three minutes throughout the orbit. CIPS began acquiring images every 2 minutes over the sunlit portion of the orbit beginning 3 November 2018, and continues in this observing mode at the present time.

2.1.1. CIPS Heritage

The CIPS instrument design is based on measurements from the Solar Backscattering Ultraviolet Experiment (SBUV) instruments, which observed PMCs via measurement of scattered UV sunlight. *Thomas and McKay* [1985] used several UV wavelengths to successfully detect large-scale PMCs with the SBUV instrument on the Nimbus-7 spacecraft. Broad spectral coverage, including several wavelengths in the Hartley ozone band, was employed. Spectral measurements enable PMC detections because the wavelength dependence of the residuals from a polynomial fit to the observed radiance is different for PMCs than for the clear-sky background. *DeLand et al.*

[2003] extended this approach using follow-on SBUV instruments. Similarly, CIPS takes advantage of the fact that UV scattering by the clear-sky background differs from scattering by PMCs. But rather than use the wavelength dependence, CIPS employs a technique that takes advantage of the strong angular dependence of PMC scattering, which departs from that of the Rayleigh-scattering background.

2.1.2. CIPS Instrument & Operations Overview

McClintock et al. [2009] describes the CIPS instrument in detail. CIPS consists of four nadir-viewing UV sensitive cameras that together provide an instantaneous field of view of 120° (along-track) by 80° (cross-track). The spectral passband is centered at 265 nm with a width of 15 nm (full-width half-maximum). Fig. 2.1-1 illustrates the orientation of the cameras, which are arranged in a cross pattern with overlapping pixels along the inner edges. We define a spacecraft-centered coordinate system with X-Y-Z axes corresponding to the roll (along-track), pitch (cross-track) axis and yaw (nadir) directions, respectively. The PX and MX cameras are pointed in the +X and -X direction, with similar convention for the Y cameras. The Y cameras are offset by ±19° along the pitch axis and thus are primarily nadir-pointed. The X cameras are offset ±39° along the roll axis and therefore project out to larger off-nadir view angles along the orbit track. Fig. 2.1-2 illustrates the distribution of offset angle across the four cameras, relative to the spacecraft nadir (Z) axis. The resulting geometric footprint of a scene (comprised of simultaneous images from all four cameras), when projected to the nominal 83-km cloud deck altitude, is characterized by the along-track and cross-track distance scales shown in Fig. 2.1-1. During routine science data operations, the AIM satellite is always oriented such that the PX camera is facing the sunward direction.

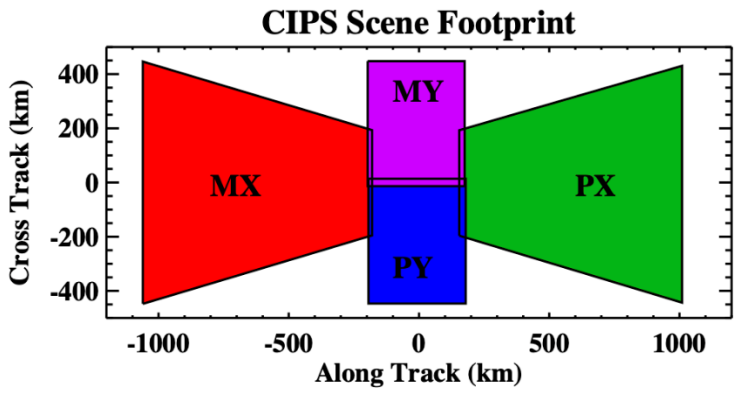

Figure 2.1-1. This diagram illustrates the relative alignment of the four CIPS cameras. The "X" cameras point in the forward and aft direction, which the "Y" cameras are primarily nadir oriented. The distance scales indicate the geometric footprint of a CIPS scene at the nominal PMC cloud deck altitude of 83 km. Note that the color-coding used here for the cameras is preserved in figures to follow.

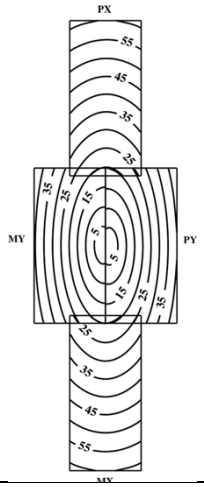

Figure 2.1-2. Distribution of offset angle from the satellite Z (yaw)-axis for the four CIPS cameras. Pointing offsets range from 0-44° for the Y cameras and 18-62° for the X cameras.

The operational data sequences used by CIPS to collect PMC science data have evolved significantly over the life of the mission. These changes have been driven primarily by two factors – the necessity of coping with external changes imposed by precession and degradation of the AIM orbit over time, and a desire to widen the scope of the geophysical sampling space to enable derivation of the new RAA data products in addition to the original PMC retrievals.

The AIM satellite was launched in April 2007 into a 600-km circular, sun-synchronous orbit with a noon/midnight (descending/ascending node) equator crossing time. This orbit was stable, with a β-angle (defined as the angle between the orbit plane the sun vector) less than 25°, until approximately 2014. By this point the orbit began to decay more rapidly, accompanied by an increased rate of orbit precession such that by 2017-2018 the β-angle passed through 90 degrees (dawn/dusk equator crossing). During this period the AIM satellite was in full-sun mode, meaning it never passed into eclipse and all CIPS measurements were made near the terminator, at high solar zenith angle. Continuing its precession, the satellite is expected to again pass through a zero β-angle configuration later in 2022. Thus, it will again be in a noon/midnight orbit, but with the ascending/descending nodes reversed, i.e., with the ascending node equator crossing at noon instead of midnight.

In response to these drastic changes in orbit configuration and solar illumination conditions along the AIM sub-satellite track, a number of different data operations sequences were devised and employed by the CIPS team to maximize the amount and quality of science images obtained each day.

From 24 May 2007 through 11 February 2016 CIPS operated in its original PMC science mode, which is now designated the Summer Pole imaging mode. In this mode, overlapping, four-camera images (scenes) were obtained every 43 seconds over the latitude range from 40° to 85° in the northern hemisphere (NH) from March equinox to September equinox, and in the southern hemisphere (SH) from September equinox to March equinox. This operational mode, and the Version 4.20 algorithms used to derive Level 2 and 3 PMC data products from the densely overlapping Level 1a calibrated images it produced, were described in detail in Lumpe et al. [2013]. The characteristic image sampling pattern for this mode is illustrated in the first column of Figure 2.1-3.

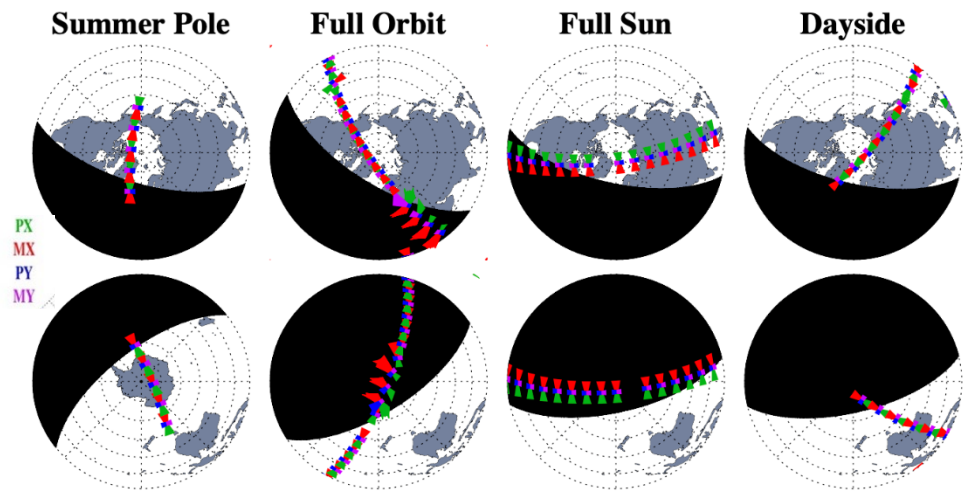

Figure 2.1-3. Polar maps illustrating typical CIPS image sequences at summer solstice in the NH (top row) and SH (bottom row). Image footprints are drawn to scale and the legend on the left identifies the cameras by color. Columns correspond to the four fundamental measurement sequences employed by CIPS to date.

Beginning in March of 2016, and continuing to the present, CIPS has operated in what is called Continuous Imaging (CI) mode. The essence of this change, relative to the original Summer Pole mode, is that imaging is now performed over the entire sunlit portion of the earth on each orbit, rather than concentrated only in the summer hemisphere. Because CIPS is limited by data downlink constraints to a maximum number of images per orbit (~30), this necessarily required a relaxation of the original 43-second measurement cadence, to spread the images out over the entire globe.

In the initial CI implementation, lasting from March 2016 through early November 2018, a 3-minute cadence was used throughout the entire ~90-minute orbit period. This mode is referred to as Full-Orbit Continuous Imaging, since images were collected on both the dayside and nightside portions of the earth. The nightside images are useless for scientific analysis and thus were never processed beyond Level 1a. The second column of Figure 2.1-3 illustrates the image sampling in this mode.

During the Full-Orbit CI time period the orbit β-angle changed significantly, passing through two periods of full-sun conditions, when β~90^o and the satellite never goes into eclipse. These events correspond to the time periods February 24 - November 23, 2017, and February 26 - September 20, 2018. Satellite roll control issues during the first full sun period prevented the acquisition of reliable calibration data, so no science data is available from this period. During the second full sun period CIPS operated in a different "Full Sun" mode, during which the satellite remained nadir-pointed but was yawed almost 90^o off the orbit plane to maintain the required solar pointing. In this configuration, illustrated in column 3 of Figure 2.1-3, the image orientation is very different from any other period, with no overlaps at all between consecutive scenes.

Beginning on November 3, 2018, CIPS was put into a mode where all images are taken over a period of ~70 minutes and confined to the sunlit portion of the globe. This required that the image cadence be changed again, from three minutes to two minutes. By October 2019, the orbit

eclipse duration had lengthened, and the data sequence duration was compressed from 70 to 60 minutes to cover the sunlit part of the orbit. The image sampling pattern of this so-called "Dayside" CI mode is illustrated in the final column of Figure 2.1-3.

Figure 2.1-4 illustrates the variation in in latitude, solar zenith angle and local time sampling for all CIPS science images through November, 2022, representing more than 2.2 million processed images. One notable feature in the top panel is the transition from mid- to high-latitude sampling in summer hemispheres only through 2015 (the Summer Pole mode) to pole-to-pole sampling when the CI mode begins early in 2016. The solar zenith angle plot in the middle panel shows that prior to 2016, and then again since the beginning of Dayside mode late in 2018, only dayside images were obtained. From 2016 through 2018, corresponding to Full Orbit and Full Sun modes, the images were approximately equally distributed between sunlit and dark conditions. Also evident is the migration of the image sampling space to higher solar zenith angles, i.e., nearer the terminator, beginning in 2015 as the AIM orbit approached and passed through the full sun phase. Finally, the lower panel shows that prior to 2016, in Summer Pole mode, CIPS measurements were confined to local times after noon in the NH and before noon in the SH, with a gradual shift to later local times beginning in ~2013. From 2016 through 2018 all local times were sampled equally, while in the Dayside mode starting late-2018 local times vary seasonally between morning and afternoon.

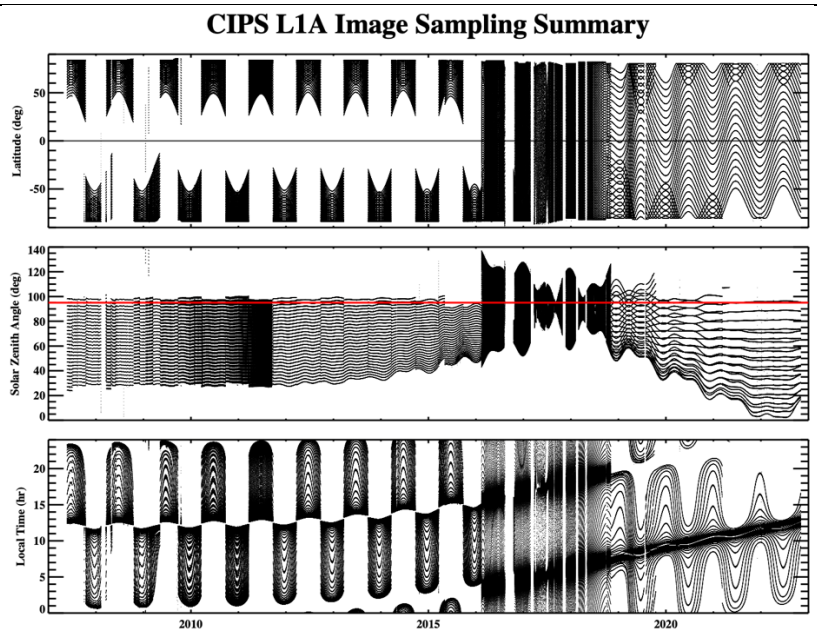

Figure 2.1-4. Mean latitude (top), solar zenith angle (middle) and local time (bottom) for all Level 1A images from the PY camera through October 2022. More than 2.2 million individual images are represented in these plots The red horizontal line in the middle panel denotes the nominal terminator solar zenith angle of 95°.

An important consequence of the reduced image cadence in the CI modes is that the dense camera pixel overlaps obtained by combining sequential images in the original Summer Pole sequence is no longer available. This overlap, obtained when the individual Level 1a images are combined into the "orbit strips" (Level 2 PMC and 2A RAA), was key to constructing the PMC scattering phase function used to derive both particle size and ice water content (IWC) parameters, as described in Lumpe et al [2013]. In CI mode, this spatial overlap is sparse or non-existent, depending on the actual measurement sequence. Figure 2.1-5 summarizes this difference for the four primary measurement sequences described above. This plot shows the fraction of Level 2 pixels for a single orbit having a given value of NLAYERS, defined as the number of independent data points per pixel. The dominant value in the original Summer Pole mode was 7, with all values up to 8 present at lower levels, whereas in the three CI modes it's either 1 or 2, with no values >3 present at all. The Dayside case has the best sampling overlap of the CI modes, a direct consequence of the 2-second image cadence compared to 3-seconds for the other two modes.

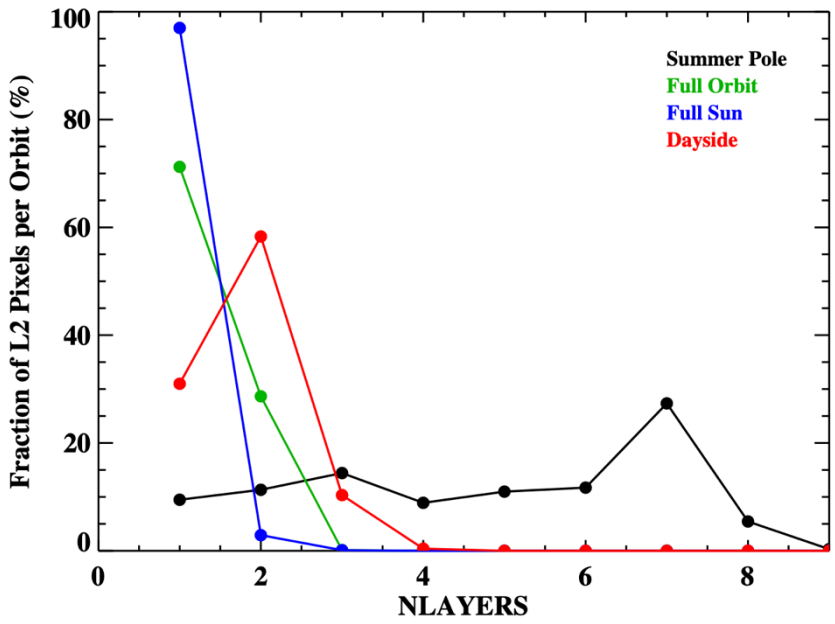

Figure 2.1-5. Fractional distribution of NLAYERS, the # of independent scattering angles per Level 2 pixel for v5 PMC data. Numbers are expressed as mean fraction of total L2 pixels in an orbit and the four curves represent typical results for each of the CIPS primary measurement sequences.

Figure 2.1-6 illustrates the basic CIPS viewing geometry and defines some fundamental quantities that will appear in the following discussion and the algorithm descriptions in subsequent sections. This figure shows a ray-trace for a single CIPS camera pixel through the atmosphere intersecting a scattering volume at geometric altitude z. The spacecraft view angle ψ, defined as the angle between the line-of-sight (LOS) vector and the spacecraft nadir, is equivalent to the pixel offset angle plotted in Fig. 2.1-2 when the satellite Z-axis is pointed to true nadir. The most important quantities for describing the scattering geometry, and hence the relevant CIPS radiative transfer problem, are the solar zenith angle, φ, view angle, θ, and scattering angle, Φ. Note that "view angle", as defined here and used in the remainder of this document, is the angle between the

LOS vector and the local zenith at the scattering point. All these quantities are dependent on the altitude of the scattering point, z. Two physically distinct altitudes are important to the CIPS measurements and retrievals – the cloud altitude at ~83 km and the peak altitude of the Rayleigh scattering contribution function, which is typically ~55 km but rapidly shifts to higher altitudes at solar zenith angles greater than ~85°.

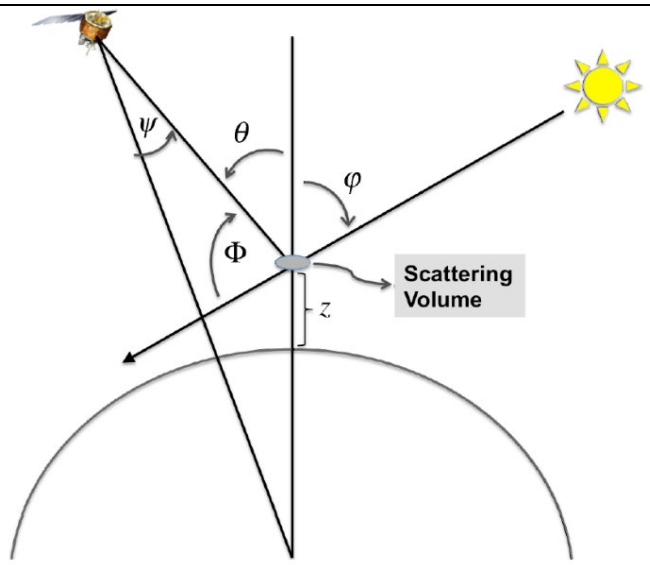

Figure 2.1-6. Schematic depiction of CIPS viewing geometry, showing the line-of-sight (LOS) of a single CIPS camera pixel projected to a scattering volume at a reference height z. This picture is simplified in that it shows the sun as coplanar with the satellite, scattering point and earth center (i.e., zero solar azimuth angle), which is not generally the case. The offset angle ψ is the angle between the LOS vector and the satellite nadir. The solar zenith angle φ and view angle θ are the angles between the local zenith (at the scattering point) and the sun and satellite directions, respectively. The symbol Φ is used to denote the solar scattering angle.

The combination of changes in the AIM orbit configuration and measurement sequences affects the scattering angle space sampled in the CIPS data. This aspect of the measurement geometry is critical because the primary characteristic distinguishing PMC scattering from the background Rayleigh albedo is the enhanced brightness at forward scattering angles. Without adequate sampling of the forward scattering portion of the scattering phase function (i.e., < 90°) it becomes difficult to accurately remove the Rayleigh background and detect PMCs in the CIPS data. Figure 2.1-7 shows the distribution of scattering angles, plotted as a function of solar zenith angle, for representative orbits on the Northern Hemisphere summer solstice for the four different measurement modes. These plots clearly show the following trends: denser image sampling in the original Summer Pole mode; shift towards higher SZA in Full Orbit and Full Sun modes (though mostly recovered by 2021 Dayside mode); a general trend towards more forward scattering at high SZA in all modes; and finally, larger minimum scattering angles, i.e., less forward scattering, in all CI mode data compared to Summer Pole mode.

2.1.3. CIPS Data Product Overview

The current version of CIPS PMC data is v5.20r05, which is available for the entire CIPS mission. A paper describing the version 5 algorithm is in preparation. *Lumpe et al*. (2013) described the retrieval algorithm for version 4 PMC data, and the v4.20r06 data are still publicly available through the 2013 (NH) and 2014/15 (SH) seasons. As explained by *Randall et al*. (2017), GW information is derived from CIPS measurements of Rayleigh Albedo Anomaly (RAA). The current version of RAA data is v1.10r06, which is described by *Carstens et al*. (in preparation).

The PMC and RAA data products for all levels are listed below. More details can be found in documentation specific to the individual levels. CIPS data for levels 2 and above are available

online at the AIM CIPS website (http://lasp.colorado.edu/aim/index.php) and at the NASA Space Physics Data Facility (SPDF; https://spdf.gsfc.nasa.gov/).

Internal (not publicly released) Data Products:

Level 0:

Raw, uncalibrated images. Images are binned on-chip to 170 × 340 pixels (cross-track by along-track) for each camera. Effective spatial resolution varies from ~2.4 km × 2 km (nadir) to ~4.5 km × 3 km (forward & aft cameras). This is common to both PMC and RAA retrievals.

Level 1A:

Calibrated and geolocated albedo. NetCDF files contain all images from a single camera over one orbit, so there are 4 files per orbit (one per camera). This is common to both PMC and RAA retrievals.

Level 1B:

Map-projected albedo at 25 km^2 resolution, calculated from level 1a data. One NetCDF file per orbit. These files register all measurements of a single location into data "stacks" to facilitate level 2 retrievals. This is used only for PMC retrievals for v4.20 and earlier versions.

Level 1P:

Level 1P consists of intermediate data files that contain corrections to systematic errors in the level 1A data. These corrections are implemented during production of the Level 2 v5 PMC and v1.1 RAA data products.

Publicly Available PMC Data Products:

Level 2:

Retrieved cloud parameters at 25 km^2 resolution for v4 and earlier versions, and at 56.25 km^2 resolution for v5 and later versions. Three NetCDF files per orbit containing, respectively:

(1) Geolocation ("catalog") data (e.g., latitude, longitude, time, etc.). The file name extension is _cat.nc.

(2) Cloud properties, including albedo, particle radius, and ice water content. The file name extension is _cld.nc.

(3) Cloud phase function (cloud albedo vs. scattering angle). The file name extension is _psf.nc.

Cloud albedo in file #2 is normalized to 90° scattering angle and nadir view. Most users of level 2 data will only require files #1 and #2. Images (png files) of cloud albedo, particle radius and ice water content for each orbit are also available.

Level 3A:

Daily cloud albedo maps, produced by combining level 2 data from all individual orbits on a given day. Where pixels from different orbits overlap, the brightest pixel (not the average) is used. Same resolution as level 2. One NetCDF and one png file per day. Each individual png file uses a color scale appropriate for that day.

Level 3B:

Movies of daily cloud albedo maps for an entire PMC season. One MPEG4 file per season. Same resolution as level 3A. Each individual MPEG4 file uses a single color scale appropriate for that season.

Level 3C:

Season-long files of level 2 data. Retrievals of cloud albedo, particle size, and ice water content from each orbit are binned in one-degree latitude bins and output for an entire PMC season. Files are available in NetCDF and IDL save formats.

Level 3D:

Season-long files of level 2 data in the "common volume" viewed by both CIPS and SOFIE. The CIPS Level 3D data are pulled directly from the Level 2 data files and consist of the subset of pixels that are co-located with the SOFIE line-of-sight. The CIPS level 3D file contains the primary CIPS level 2 retrieval products and associated auxiliary data, in the CV, for each orbit over an entire PMC season. This data product is available only for the years 2007-2009, and the file format is ASCII text.

Level 3E:

Analogous to Level 3d, but these files contain data that are coincident with a selected group of ground stations.

Publicly Available RAA Data Products:

Level 2A:

Retrieved CIPS RAA data in a scene-by-scene format. A CIPS scene contains simultaneous images from the four CIPS cameras, with a footprint of approximately 2000 km by 900 km, as described in *Lumpe et al*. (2013). Three NetCDF files are provided, with each file containing data (or plots) for all scenes in a given orbit. In addition, png image files are provided for each scene separately:

(1) Geolocation: Includes variables such as date, time, latitude, longitude, solar zenith angle, etc. The file name is *cat.nc.

(2) RAA: Includes RAA, FFT-filtered RAA, FFT-filtered RAA variance, and corresponding uncertainties. These files also include the 2D FFT wave amplitudes vs. wavelength (1/wavenumber) and wave orientation. The signal-to-noise ratio (SNR) for wave detections must be user-calculated as the ratio of [filtered RAA variance] to [filtered RAA variance uncertainty]. The file name is *alb.nc.

(3) Measurement geometry: Includes satellite view angles and scattering angles for each scene. The file name is *ang.nc.

(4) Plots of RAA, FFT filtered RAA, and RAA variance for each scene in a given orbit. Regions of significant wave detections (SNR>3) are indicated. The file name is *.png.

Level 2B:

Retrieved RAA in an orbit-by-orbit format. All scenes from an orbit are merged together by averaging overlapping pixels from different cameras. Three level 2B files for each orbit are provided:

(1) Geolocation: Includes variables such as date, time, latitude, longitude, solar zenith angle, etc. File content is similar to the Level 2a cat file. The file name is *cat.nc.

(2) RAA: Includes RAA, FFT-filtered, RAA variance, and corresponding uncertainties. The file name is *alb.nc.

(3) Plots of RAA and RAA variance for each orbit. Regions of significant wave detections (SNR>3) are indicated. The file name is *.png.

Level 2C:

Daily, global maps of RAA and of RAA variance, produced by over-plotting level 2B RAA and RAA variance data for all orbits each day; file format is png.

Level 3A:

Daily, global maps of gridded (1° × 1°) RAA variance. Both one-day and five-day maps are provided in a single file for each day, in numerical (*.nc) and graphical (*.png) formats. The 5-day map corresponding to day "x" contains mean variances in each grid cell from days "x-4" to day "x". If data for day "x" is missing, the 5-day map for day "x" is also missing.

2.2. CIPS Theoretical Description

This section presents the underlying theoretical basis and describes the algorithms used to generate the CIPS data products, starting with Level 1P (see Fig. 2.2-1). The Level 1A data processing is covered in the Calibration description in Section 2.3.

Figure 2.2-1 illustrates the CIPS data processing flow and the functional dependencies between the data products described in Section 2.1.3. The older v4 PMC processing steps are outlined in panel (a) while panel (b) illustrates the processing flow for the combined v5 PMC and RAA data stream. The PMC and RAA data streams split after the Level 1P is produced, so this is the last data level in common to both. Merging of the single-image data by averaging overlapping pixels from different cameras occurs at Level 2(2B) in the PMC(RAA) data flow.

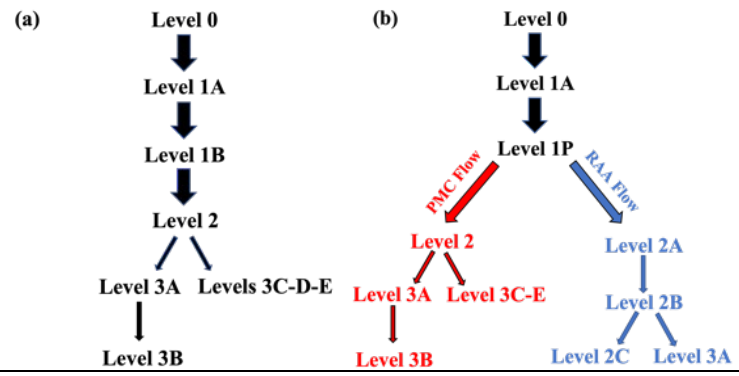

Figure 2.2-1. CIS data processing flow for (a) Version 4 PMC processing and (b) Version 5 PMC and RAA processing.

2.2.1. Forward Model

The albedo measured by CIPS at a given location is a sum of contributions due to the background atmosphere plus cloud scattering if a cloud is present:

$$A_{meas}(\theta, \varphi, \Phi, C, \sigma) = A_{Ray}(\theta, \varphi, \Phi, C, \sigma) + A_{cloud}(\theta, \Phi, r_o) \quad (2\text{-}1)$$

where θ, φ, and Φ are the view angle, solar zenith angle and scattering angle, respectively (see Figure 2.1-6), r_o is some measure of cloud particle radius, C is the ozone vertical column density above a reference altitude and σ is the ratio of the ozone to atmospheric scale.

The second term in Equation (2-1) is of course irrelevant for RAA retrievals in the absence of PMCs. In this scenario, Equation (2-1) can be written more simply as the product of two terms:

$$A_{meas}(\theta, \varphi, \Phi) = A_{Ray\_n}(N_{O_3}, N_{tot}, \sigma) \times G(\theta, \varphi, \Phi, \sigma) \quad (2\text{-}2)$$

Here G is a geometric factor for the 7.5 km × 7.5 km RAA pixel bin with geometric factors of θ, φ, and Φ; note that θ (view angle) and φ (solar zenith angle) vary along the line of sight. All parameters in G except for σ are known for every RAA bin. The RAA retrieval assumes monthly mean climatological values for σ in 10° latitude bins as calculated by *McPeters and Labow* (2012) from MLS ozone. Geophysical variability in σ, as observed by MLS, is insignificant for the purposes of the CIPS retrievals, justifying the use of climatological data. A_{Ray_n} is the Rayleigh albedo that would be observed at Φ=90° and θ=0° and is essentially a scaling factor on the Rayleigh scattering phase function. A_{Ray_n} depends on σ as well as N_{O_3} and N_{tot}, the ozone and atmospheric column densities, respectively, above the peak of the Rayleigh scattering source function.

With an assumed value of σ, G is known, so A_{Ray_n} can be calculated for each RAA bin as A_{meas}/G. A spherical harmonic fit is then performed on the A_{Ray_n} values for each day to construct a smooth surface which serves as the baseline, A_{Ray_base}, upon which we define our anomalies so that the final RAA in each bin, expressed as a percent, is given by:

$$RAA = 100\,(A_{Ray\_n} - A_{Ray\_base}) / A_{Ray\_base} \quad (2\text{-}3)$$

This forward model is generally accurate enough to describe about 99% of the Rayleigh albedo variance observed in a CIPS scene as shown by the solid lines in Figure 2.2.1-1. However, even in that 1% residual variance, the waves and random noise typically make up less than 0.1% of that variance. Most of this variance is due to correctable systematic errors that are described in section 2.2.2. After correcting for these errors, the model describes ~99.9% of the variance in the data as shown in the dotted lines.

Dictated by the RAA bin size and CIPS scene size, the RAA retrievals are most sensitive to perturbations from GWs with horizontal wavelengths of ~15-600 km; detection of longer-wavelength GWs is possible but requires that the wave crests be aligned along-track or nearly so. The RAA retrievals are most sensitive to GWs with vertical wavelengths ≥15 km, which is determined by the vertical weighting function for the ozone absorption contribution to the observed albedo.

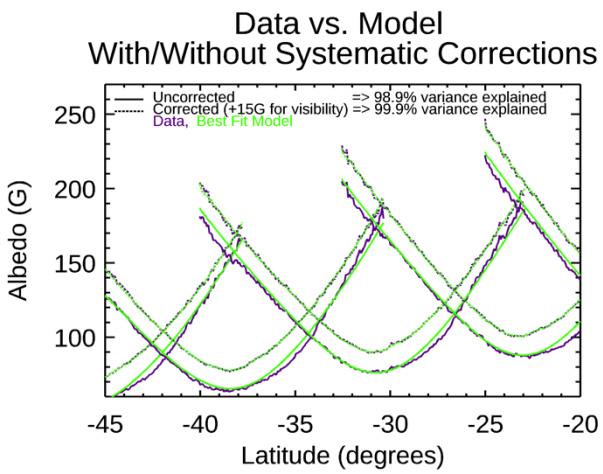

Figure 2.2.1-1. Example best fit Rayleigh numerical C-σ model to the observations for a row of pixels down the middle of an orbit strip. Even before applying the systematic corrections necessary for the RAA retrievals, the single parameter model fit explains ~99% of the variance in the data. However, most of this residual ~1% variance is still systematic instrument artifacts. It is only after correcting for these errors (dashed lines) where the gravity waves contribute meaningfully to the final ~0.1% of the observed albedo variance.

2.2.2. Post-Calibration Level 1 Algorithm and Error Analysis

The algorithm and processing steps required to produce L1A data are described in the calibration summary in section 2.3, since L1A essentially consists of calibrated, geolocated directional albedo for each individual camera image. The analysis and processing steps outlined in sections 2.2.2.1 – 2.2.2.3 below describe the post-L1A processing required to produce the intermediate L1P data product. As discussed previously, this data level is the fundamental input to the downstream PMC Level 2 products for both PMC and RAA data. In this section we motivate this series of Level 1 processing steps solely by illustrating their impact on the Level 2 RAA data.

In the absence of PMCs, the Rayleigh scattering source function for the 265 nm radiance observed by CIPS peaks near an altitude of 50–55 km [*Bailey et al.*, 2009]. Since the observed Rayleigh scattering signal is controlled by the atmospheric neutral density and is modulated strongly by ozone absorption [*Bailey et al.*, 2009; *McPeters*, 1980], coherent perturbations to the observed Rayleigh scattering signal on scales of tens to hundreds of kilometers are generally indicative of gravity wave (GW)-induced variations in the neutral density and/or ozone near 50–55 km. To quantify these perturbations, we calculate the Rayleigh Albedo Anomaly (RAA), which is defined as the residual difference between the observed Rayleigh scattering albedo and a "baseline" albedo that would be observed in the absence of any small-scale atmospheric variations.

In theory, the baseline albedo could be calculated by smoothing the observed albedo to average out perturbations. Because each CIPS pixel is characterized by a unique observation geometry, and this geometric dependence tends to be significantly larger than the GW induced fluctuations, such a smoothing is not feasible in practice. Instead, the baseline albedo is calculated using a numerical generalization of the so-called C-σ Rayleigh model [*McPeters*, 1980; *Bailey et al.*, 2009; Lumpe *et al*., 2013]. Thus, the algorithm for deriving RAA data is similar to that for PMC data as far as the background Rayleigh scattering determination. However, the residuals (observed signal minus Rayleigh background) are interpreted for an altitude of ~55 km, not ~83 km as in the case for PMCs.

The largest sources of error that need to be corrected to retrieve GW signals in the CIPS RAA are systematic. The largest of these is the Delta Flat Field (DFF) error corrections which measure the average difference between smoothed best fit C-σ modeled albedo images and

observed albedo images after the ground calculated flat fields have been applied (see section 2.3). These DFF corrections are assumed constant over long periods of time and are recalculated on an as needed basis when significant changes are noticed or forced by significant changes in the operating mode of the instrument. On top of these average errors, there are higher order systematic modes and linear gradients to the errors which vary over time and over the course of the orbit. These modes are determined via Principal Component Analysis (PCA) that is run on a 1- to 2-week cadence. Structures in the RAA images which are consistent with linear combinations of the PCA components are removed. While the PCA corrected errors are significantly smaller than the DFF corrections, they can still be similar in magnitude to wave structures that are readily identifiable over the noise, so it is important to correct for these errors as well.

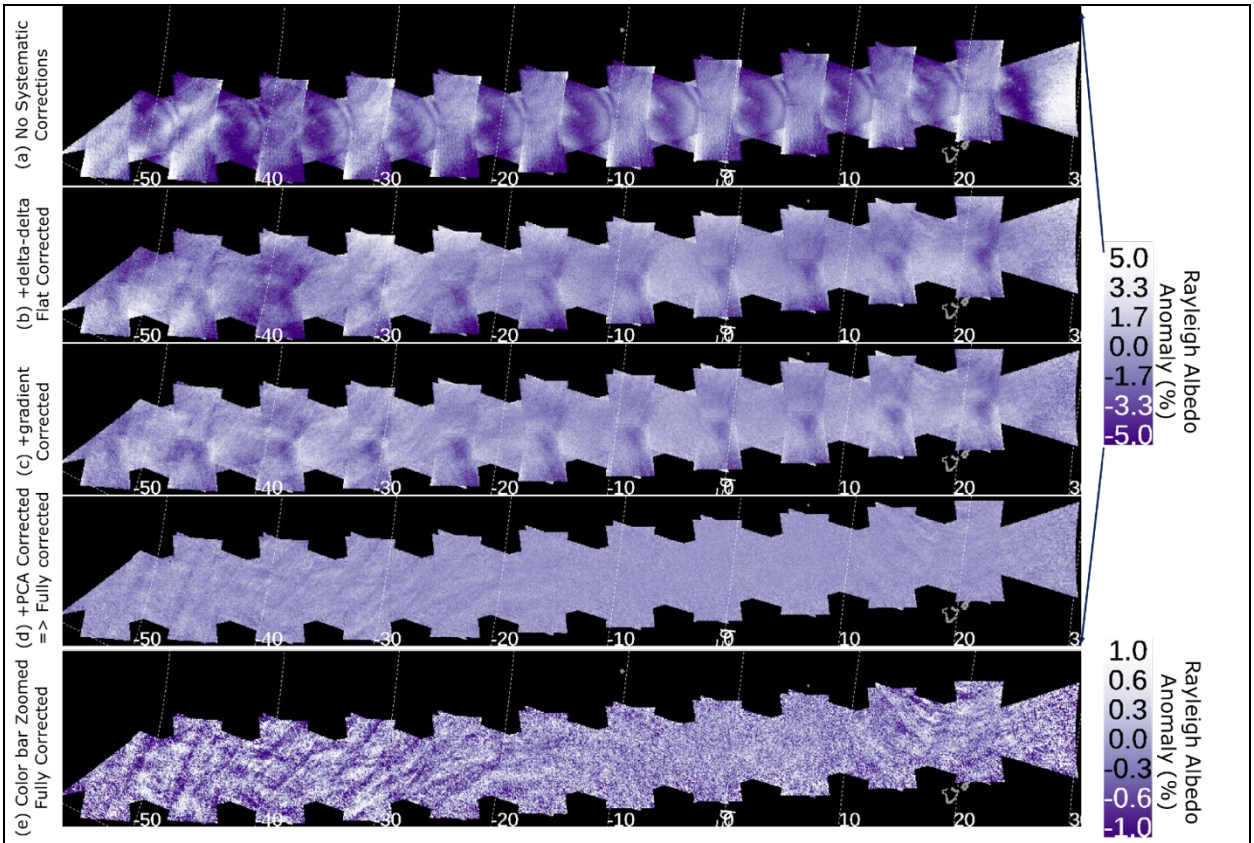

Figure 2.2.2-1. Impact of each systematic correction step on the orbit strip. (a) Best fit data-model RAA without any systematic corrections applied. (b) Delta-delta flat corrections applied. (c) Ozone gradient consistent corrections additionally applied. (d) PCA corrections additionally applied (final). (e) Same as (d) but with the color bar zoomed to bring out the detail uncovered by the systematic corrections.

After removing the above systematic sources of error, the largest remaining source of error is pixel noise, which we characterize in the sections below. The GW amplitudes are usually on the same order as the pixel noise, but the waves are nonetheless easy to extract because of their spatial coherence. In the frequency domain for example, the waves are well above the noise.

Figure 2.2.2-1 shows the progression of an RAA orbit strip after each systematic error correction step is applied. It is only after correcting for the systematic errors that the waves become apparent in the data. These steps are described in more detail in the following sections.

2.2.2.1. Delta-Delta-Flat-Field Corrections

The CIPS Level 1A data has a pre-flight ground calibrated flat field as well as a delta flat field calculated using a legacy technique described in section 2.3. However, for the purposes of the RAA retrievals, this technique does not remove enough of the average residual average error seen between the Rayleigh model (calculated as described above) over the whole range of solar zenith angles and latitudes. To account for this, we calculate an additional Delta-Delta-Flat-field (DDFF) correction to be applied on top of the two initial flat-field corrections. These DDFF corrections are derived on as needed basis throughout the mission.

The DDFF algorithm uses an iterative gradient decent approach to simultaneously derive a least squares best fit DDFF for each camera and any average model correction as a function of solar zenith angle or view angle. These latter two dependences are added in case there is any component of the error which correlates better with a model error rather than a camera calibration error. The view angle dependence was only separable from the flat field dependence during the full sun period in 2017. During this period, the spacecraft was rolling about the sun vector, so the view angles observed by each pixel varied. At other times during the mission, the field of view is fixed relative to nadir, so the same pixels always see approximately the same view angles, therefore any view angle dependence to the error was inseparable from a pixel calibration error.

The resulting DDFF for each camera are shown in Figure 2.2.2.1-2 and the average error attributable to the view angle and solar zenith angle are shown in Figure 2.2.2.1-1. Approximately an order of magnitude larger error is associated with the DDFF than is attributed to the average angular dependence model error, with the exception of high zenith angles. The majority of the average difference between model and data are camera calibration related. Outside of full sun, the view angle dependence derived here is assumed since it cannot be derived in other modes.

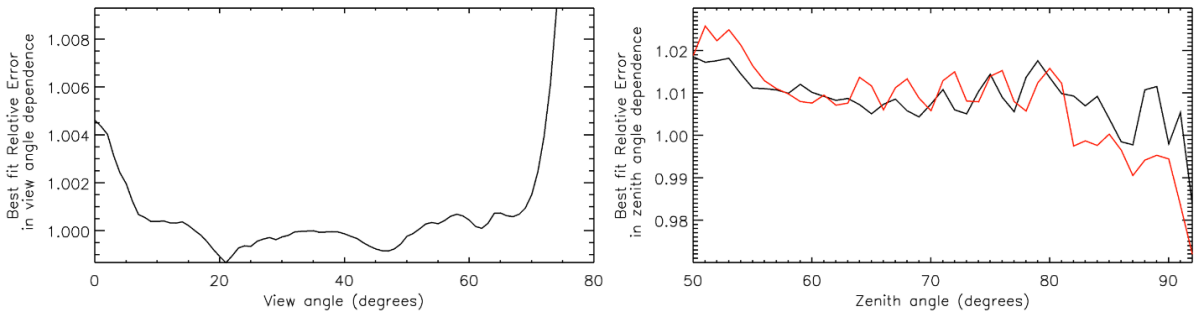

Figure 2.2.2.1-1. SZA and VWA attributed errors. For the SZA dependence, red indicates sunrise and black indicates sunset data.

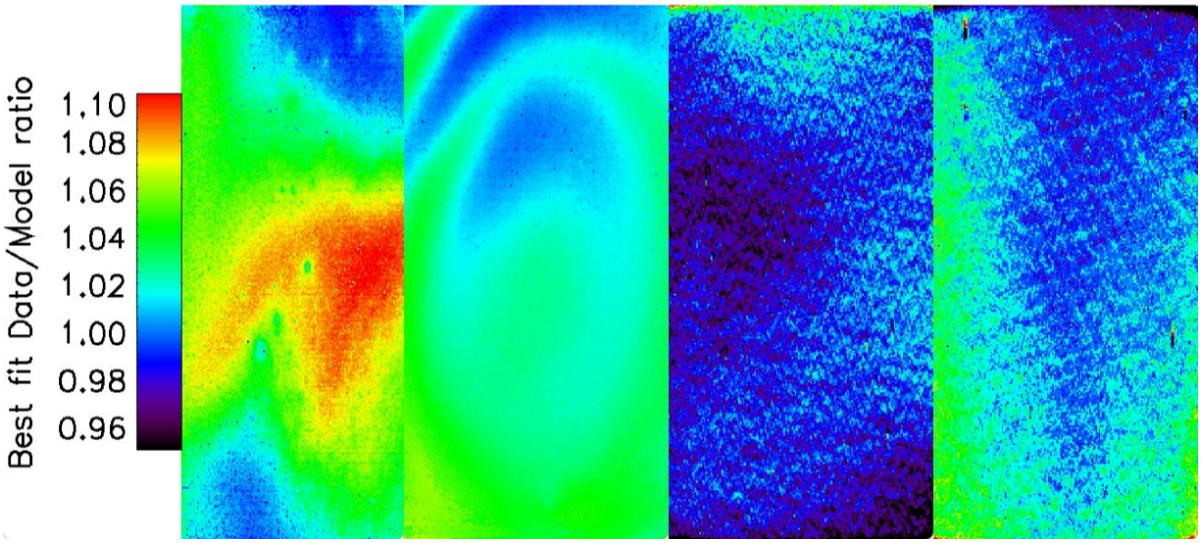

Figure 2.2.2.1-2. Example Delta-delta-flat (70-minute sequence) for PX, MX, PY and MY (left to right).

2.2.2.2. Principal component analysis and planar ozone gradient consistent corrections

As can be seen in Figure 2.2.2-1 (panel a vs. b), the majority of the systematic error can be attributed to a constant flat field correction. However, as we can see in panel b, significant repeating systematic artifacts remain in the data which contaminate any attempt to extract gravity wave signatures. These residual artifacts can be represented using linear combinations of error modes identified using a principal component analysis (PCA) and gradients consistent with residual variations in the ozone that are larger in scale than a camera footprint.

It is necessary to separate out the gradient component because such gradients are common in the data for geophysical reasons, but consistent patterns can occur which causes them to become ingrained in the non-geophysical PCA components. Some component of the camera errors we are attempting to correct in the PCA may be consistent with linear gradients in the ozone, but this component is difficult to separate from a potential geophysical gradient. When we leave these

gradients for the PCA to correct, the effectiveness of the PCA corrections degrades any time the large-scale ozone patterns drift.

The PCA components are derived using 100-orbit sets repeating every 100 orbits (~1 week). Additional special case runs are often needed when we have an operating mode change in the satellite. During the PMC season, we blank out the region poleward of 60^o latitude to prevent PMC contamination. We often force special runs directly before and after the cloud season so that we have fully sampled PCAs covering as many days as possible. Data processed using an in-season PCA are plotted using an alternate red colored color bar in the PMC region in the operationally produced plots.

As one can see looking at Figure 2.2.2-1(b) vs. (d), the PCA and gradient corrections remove pretty much all the remaining systematic artifacts from the images, finally revealing the wave structures in the data. Panel (e) shows the same data plotted with a more appropriate color range to better see the wave structures.

2.2.2.3. Noise Level Characterization

The behavior of the noise was characterized using the standard deviations in small neighborhoods about a smooth modeled background as a function of albedo (during periods of low GW activity). An example of one of the results of this analysis for an example camera neighborhood can be seen in Figure 2.2.2.3-1.

For the most part, the noise follows the expected Poisson distribution. A notable departure is that the reduction in noise one would expect from binning pixels is not quite as large as expected, particularly for small numbers of neighboring pixels. An explanation for this effect is that some component of the noise in neighboring pixels is correlated due to the point spread function of the optical system. To account for this we fit proportionally constants, B, assuming a Poisson noise curve like, $\sigma = \sqrt{A/(BN_{1A})}$. Where A is the neighborhood albedo, and N_{1A} is the number of 1A pixels contained in the level 2 bin. For small numbers of pixels binned the constant decreases because each additional pixel added doesn't reduce the noise as much as expected; however, for larger numbers of pixels binned the curves are much flatter as expected when the additional pixels are uncorrelated (i.e., the behavior becomes much more Poisson-like).

Typical noise levels produce variances on the order of $(0.25\%)^2$ in the RAA. These levels are actually similar to typical wave amplitudes including those seen in Figure 2.2.2-1, but since the wave variances are much more spectrally coherent, the waves are nonetheless easy to pick out down to variances as low as ~$(0.01\%)^2$.

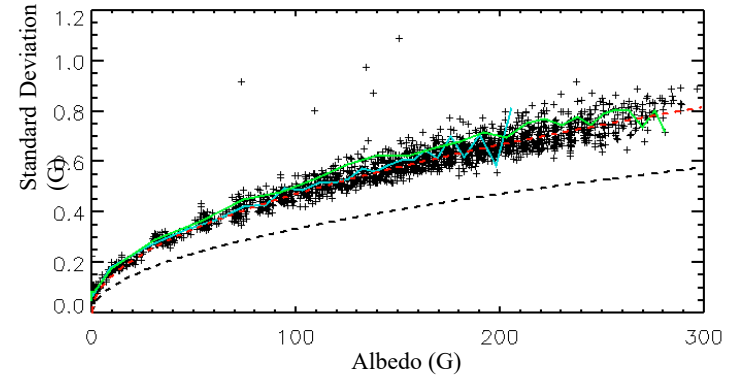

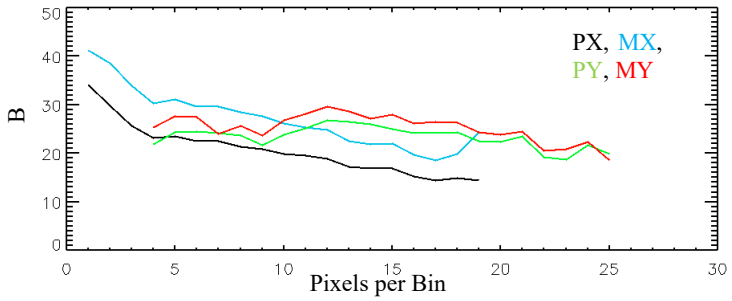

Figure 2.2.2.3-1. (top) The scatter plot shows the standard deviations for all 17 pixel per bin neighborhoods on the PY camera. The green and blue lines show the same for two distinct regions of the camera. The dashed line is the theoretical expectation for a proportionality constant B=25, and the dashed line is for B=50.

(bottom) Best fit proportionality constants for all 4 cameras as a function of pixels per bin.

2.2.3. RAA Retrieval Algorithm and Error Analysis

Using the same set of wave free orbits, the spectral domain noise was analyzed to determine the median noise level and the probability distributions of higher noise amplitudes. The spectral amplitudes are determined using a Fast Fourier Transform (FFT) of the RAA in a scene. Each scene is cropped to 90 pixels (675 km) from the nadir pixel to reduce noise levels in the spectral domain that result from the highest view angle points in the scene. The crop window is large enough to avoid data gaps between scenes even in the lowest cadence imaging modes. Pixels outside the camera FOV or the crop window are set to zero and padding is added to the outside edges of the scene to smooth the transition to zero.

For spectral significance determination, the FFT amplitudes are smoothed into 5x5 neighborhoods. This increases the statistical contrast between real waves and noise because, for a real wave packet, neighboring spectral elements are highly correlated whereas noise spikes are relatively uncorrelated between neighboring spectral elements. An exception is a perfect monochromatic planewave covering the entire scene, but waves tend to be much more complicated in observations, with wide wave packets in the spectral domain.

This smoothed FFT is only used to determine statistically significant neighborhoods. The smooth is not applied to the spectral amplitudes themselves in the variance analysis described below. The spectral amplitudes are normalized by the expected average amplitude per wave number element needed to explain the average spatial domain noise level. This removes almost all the differences between different SZA bins, which have different noise levels due to having different average albedos had this normalization not occurred. The data is partitioned into separate

sets based on SZA and the space craft yaw state to account for any systematic differences along the orbit track. These tend to be small except at very high SZA.

The results of the analysis for one SZA bin are shown in Figure 2.2.3-1. The dots are the individual wavelength bin amplitudes reaching the 50th (purple) and 100th percentile (black) and the green and red curves are fits to those sets of points, respectively. The average ratio of the red line to the green line is the threshold used in the spectral significance filter below. The purple line is the fit for the ~99th percentile amplitude. Note that it is closer to the red curve for high wavelengths than for low wavelengths. This is because there are more observations in the lower wavelength bins (~3000) than the high wavelength bins (~150) so the highest observed amplitude (100th percentile) corresponds to a lower probability event for lower wavelengths.

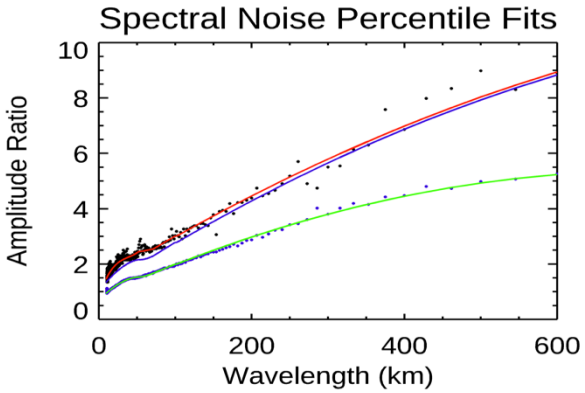

Figure 2.2.3-1 Spectral noise amplitude ratio vs wavelength for 50th (green line), 99th (purple line) and 100th (red line) percentile amplitudes. The solid lines are fits to the scatter plot in the 50th and 100th percentile bins.

The FFT for each scene computed following the procedure described above is provided in the RAA L2a "_alb" data files. The 5x5 neighborhood is also computed for filtering purposes. However, this is not the FFT which is saved in the data files. See panels (b) of Figures 2.2.3-1 and 2.2.3-2. Neighborhoods exceeding the threshold defined in above are deemed significant for variance analysis. A 9th order Butterworth filter is further applied to the variance analysis to screen wavelengths longer than 400 km or shorter than 20 km. The long wavelength end removes large scale structure which the noise levels have difficulty characterizing. The short wavelength end is probably mostly superfluous since waves of such small scale are rarely seen, but it guarantees no noise spikes from ~half of the spectral domain will contaminate the variance analysis.

Spectral elements that are not filtered above are inverted back into the spatial domain to obtain the spectrally filtered RAA. See panels (c) of Figures 2.2.3-1 and 2.2.3-2. The expected spatial domain noise level to be allowed through the filter is computed. If no components are deemed significant as is (nearly) the case in Figure 2.2.3-2, this uncertainty will be zero (as will be the filtered RAA variance). For more complex waves with many spectral components, as in Figure 1, more noise variance will be let in along with the waves so the expected noise variance will increase along with the wave variance, although generally not by as much. This can have the effect of making it more difficult for smaller waves in the same scene as a larger wave to pass the significance threshold. Spatial domain variances exceeding a signal to noise ratio (SNR) of 3 over the expected noise variance are deemed significant.

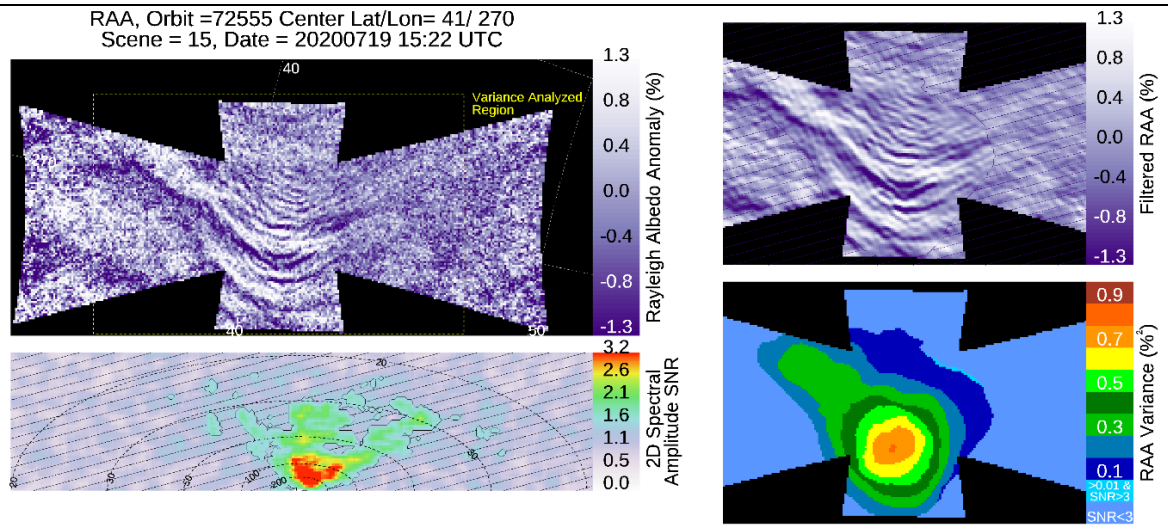

Figure 2.2.3-1 Wave example spectral filter variance analyzed scene. (a) RAA scene. (b) Smoothed (5x5) FFT amplitude ratio (relative to median noise). Insignificant filtered components are indicated by the diagonal filled regions. (c) Spectrally filtered RAA. Regions with an SNR<3 are indicated by the diagonal filled regions. (d) Filtered RAA Variance of the statistically significant regions in circular 155 km radius neighborhoods.

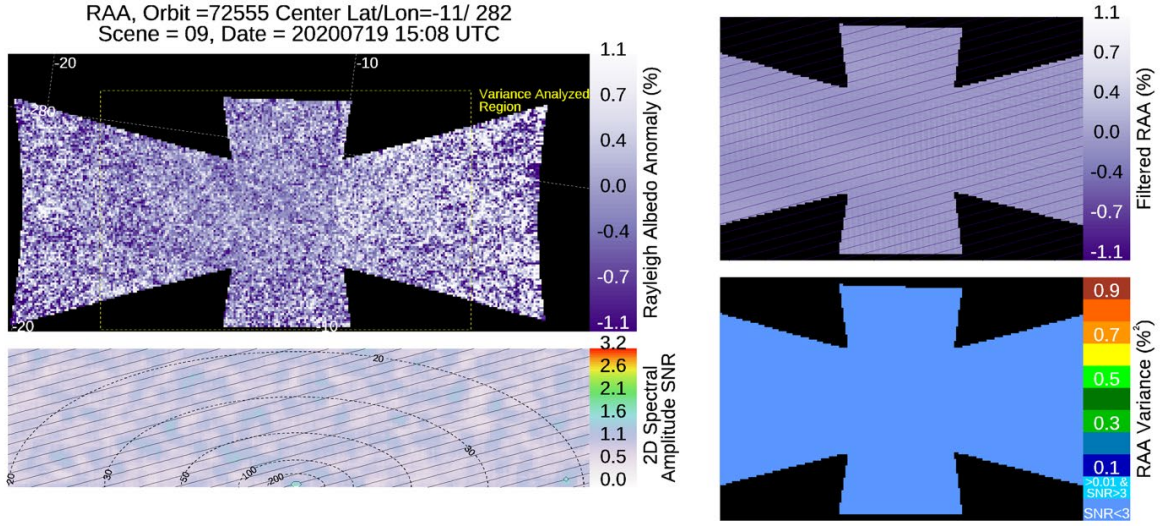

Figure 2.2.3-2 Wave example spectral filter variance analyzed scene. (a) RAA scene. (b) Smoothed (5x5) FFT amplitude ratio (relative to median noise). Insignificant filtered components are indicated by the diagonal filled regions. (c) Spectrally filtered RAA. Regions with an SNR<3 are indicated by the diagonal filled regions. (d) Filtered RAA Variance of the statistically significant regions in circular 155 km radius neighborhoods.

There are two sources of error associated with filtering spectral components based on significance. For each element let through the filter, the noise associated with those elements is also let through the filter. Particularly in the case of spectral filters encompassing fewer spectral components, this noise can look deceptively wavelike in the regions outside the wave envelope. Caution is needed when interpreting wave structures with variances on the order of the expected noise. See Figure 2.2.3-3. Since only neighborhoods above our noise threshold are kept, wave components outside of a significant neighborhood will be missing from the filtered RAA. Edges of larger wave packets can be missed, which results in a small net drop in the total variance of the packet. Truncating the edges can also result in a loss in containment of the wave packet from the original envelope. This error can artificially leak variance from inside the wave envelope to a region of the scene outside the envelope. However, this additional error is generally significantly smaller than the unavoidable noise error resulting from the spectral elements we do not filter (see the bottom two images in Figure 2.2.3-3). Some vary faint or very small envelope wave packets can be missed.

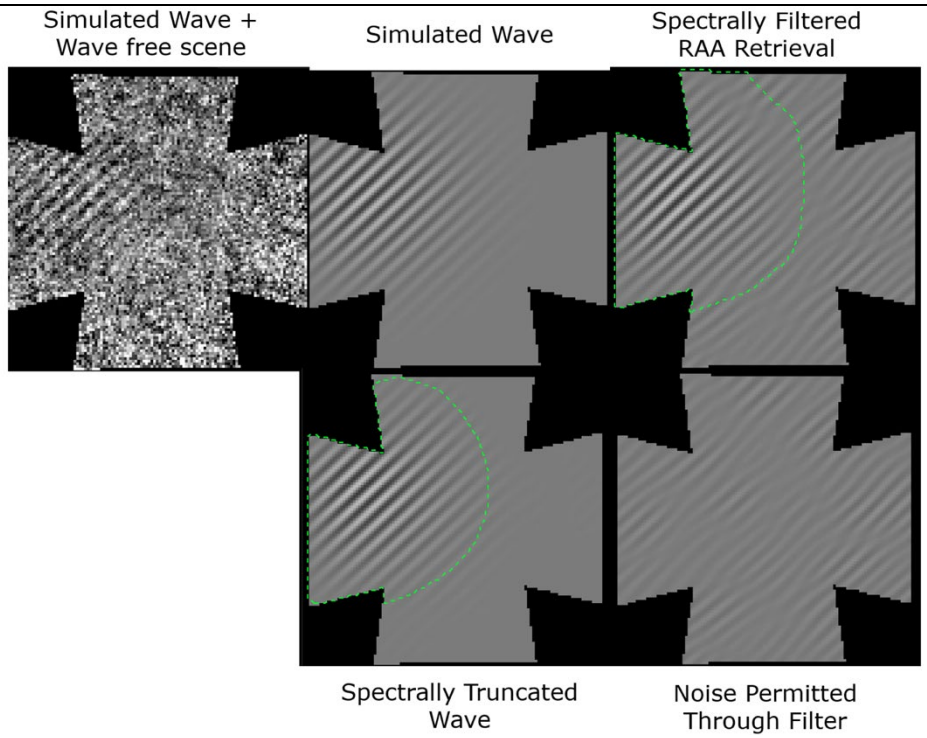

Figure 2.2.3-3 Simulated wave packet added to an observed wave free scene.

2.2.4. PMC Retrieval Algorithm and Error Analysis

The description provided in this section pertains only to the CIPS version 5 PMC data. The version 4 PMC algorithms were described in detail in *Lumpe et al.,* [2013]. In 2016, the drift of the AIM satellite's sun-synchronous orbit towards higher beta angles demanded changes to the operating mode of the CIPS instrument. It went from taking images every 42 seconds and getting ~7 overlapping observations per observed cloud parcel to taking images every 2-3 minutes and

only getting 1-3 overlapping observations per cloud parcel. The method of the version 4 retrieval relied on the PMC phase function shape to separate the cloud signal from the Rayleigh background. It could no longer be used with so few observations per parcel. This prompted the development of the level 5 algorithm whose description follows. The version 5 algorithm does not rely on the phase function shape to determine the Rayleigh background, so it is able to operate across all CIPS operating modes.

Since the version 5 algorithm was built on top of the level 1 post-calibration steps outlined above (section 2.2.2), those improvements to the systematic error corrections developed for the RAA product are also used in the version 5 PMC product. Version 5 also incorporates a more detailed characterization and propagation of errors, which allows for better informed maximum likelihood estimates of the cloud parameters and their uncertainties. Combining the above improvements with the fact that version 5 is capable of being applied to the whole data set, version 5 replaces version 4 for the entire data set, including 2007-2015 prior to the CIPS operating mode change.

2.2.4.1 PMC Rayleigh background determination

The version 5 algorithm was designed around the goal of determining the Rayleigh background level with as few as one observations per phase function. We do that by leveraging the ability to identify cloud-free regions within an image using relative residual histograms of the form,

$$residuals = \frac{(data-model)}{model} \times 100, \tag{2-4}$$

where the model uses a climatological value for the Rayleigh magnitude.

Figure 2.2.4.1-1 shows an example of such a residual image and histogram in the absence of clouds. In the absence of strong GW activity, which is common at PMC latitudes and times, the histogram shape of cloud-free pixels is very predictable and distinctly different from the distribution added by the presence of clouds seen in Figure 2.2.4.1-2. The width of this Rayleigh peak distribution is determined in the cloud-free pre- and post-season data. This width is used to define the width of the theoretical Gaussian distribution (green curves in Figures 2.2.4.1-1 and 2.2.4.1-2) used in the fits. Clouds add a positive-definite and broad tail to the histogram, but the distinctly narrow Rayleigh peak is still visible when there are enough cloud-free pixels in the image.

We use an autocorrelation-like algorithm to fit the theoretical Gaussians to partly cloudy images. The shift offset of the theoretical Gaussian derived from the best fit to the residual distribution seen in the data (MFIT variable) tells us how much brighter or dimmer the Rayleigh background was relative to the model used in the image/histogram residual calculation, thus yielding a measurement of the Rayleigh background magnitude in an image.

Note, the x-axis ranges in the histogram panels of Figures 2.2.4.1-1 and 2.2.4.1-2 are not absolute. They have been shifted to approximately center the histograms about zero. The absolute shift for the best fit is indicated by the MFIT parameter displayed in the top right corner of the figures. For the example in Figure 2.2.4.1-1, the Rayleigh magnitude, Rn, was shown to be 8.5% dimmer than the model used in the calculations of the residuals. For Figure 2.2.4.1-2, the measured Rayleigh magnitude was 9.25% dimmer than the model.

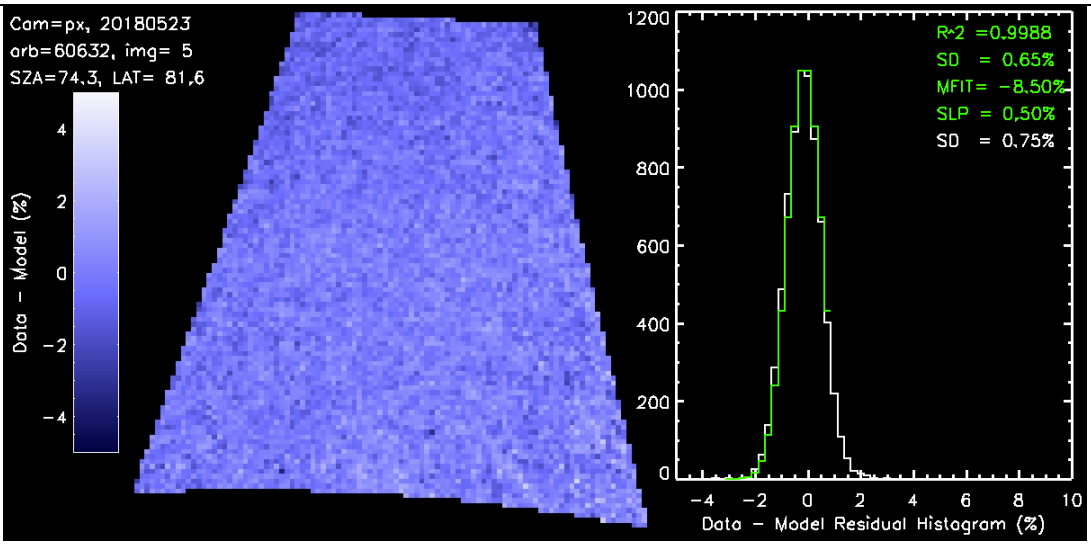

Figure 2.2.4.1-1 Cloud free example of a residual image (eq 2-4) and histogram used in identifying the Rayleigh background pixels within an image. The white curve is the histogram from the image on the left, and the green curve is a fit using a theoretical gaussian distribution with a width determined using an analysis of cloud free pre-season data.

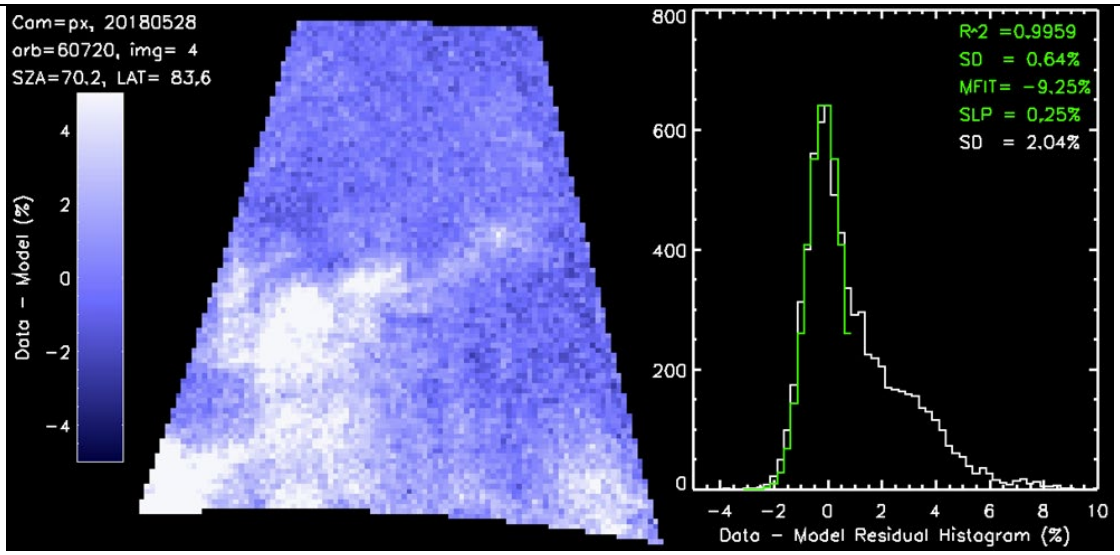

Figure 2.2.4.1-2 Partly cloudy example of a residual image (eq 2-4) and histogram used in identifying the Rayleigh background pixels within an image. The white curve is the histogram from the image on the left, and the green curve is a fit using a theoretical gaussian distribution with a width determined using an analysis of cloud free pre-season data.

Acceptance of measurements as valid requires R^2 values greater than 99% and at least 30% of the image to be cloud free (as determined by the mode height of the model Gaussian fit). These thresholds were chosen conservatively using analysis of the resulting biases of the Rn values retrieved vs. quality of fit. Because of the positive-definite nature of the cloud residuals, they tend

to artificially inflate the retrieved Rn values when they contaminate the measurement. For Rn measurements with fit parameters better than the above, there is no significant systematic bias compared to those with better fit parameters (higher correlation and/or more cloud-free pixels). As long as there are sufficient statistics to determine the average Rn and its variance in a given grid cell, there is no detriment to throwing away potentially accurate measurements. The conservative thresholds chosen here make that possible in general.

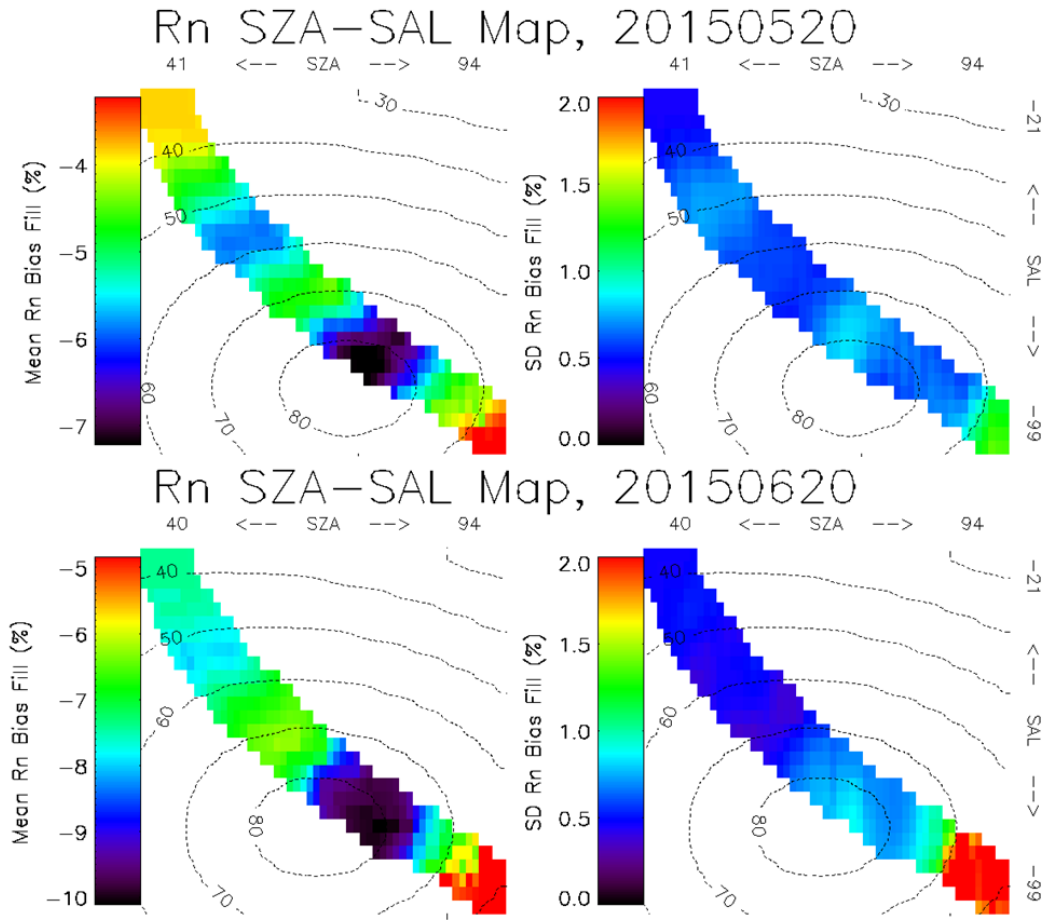

Figure 2.2.4.1-3 Pre- (top) and mid-season (bottom) examples of the daily grid of Rn used in the background subtraction. The left column are the average anomalies from the climatological value and the right column is the standard deviation. The data is gridded by position within an orbit using SZA as an elevation angle and SAL as an azimuthal angle. The latitude contours are shown for reference.

All valid Rn measurements are collected into a daily global grid going back 1 week. To account for any simple temporal trend while gathering more statistics on the variance, the data in each cell is fit to a line as a function of time rather than performing a simple average. The evaluation of that line on the current day is used as the magnitude for the Rn values. The variability about the trend line is used as the uncertainty in the magnitude of the background removal. It is driven more by real variability in the atmosphere (stratospheric PW) than by measurement errors,

but for the purposes of the PMC retrieval, it is a source of error (generally the largest source). Examples of these gridded Rn retrievals are shown in Figure 2.2.4.1-3. The grid is constructed using Solar Zenith Angle (SZA) as an elevation angle mapping of the globe centered on the sub-solar point and Solar Azimuth Longitude (SAL), which maps out the azimuthal position on the globe perpendicular to the SZA. The SAL grid origin is arbitrarily set to zero at the midpoint of the orbit where the observed SZA are the smallest, resulting in SAL values of approximately -90^{o} and +90^{o} at the terminator crossings.

A flow chart for the Rayleigh background retrieval is shown in Figure 2.2.4.1-4.

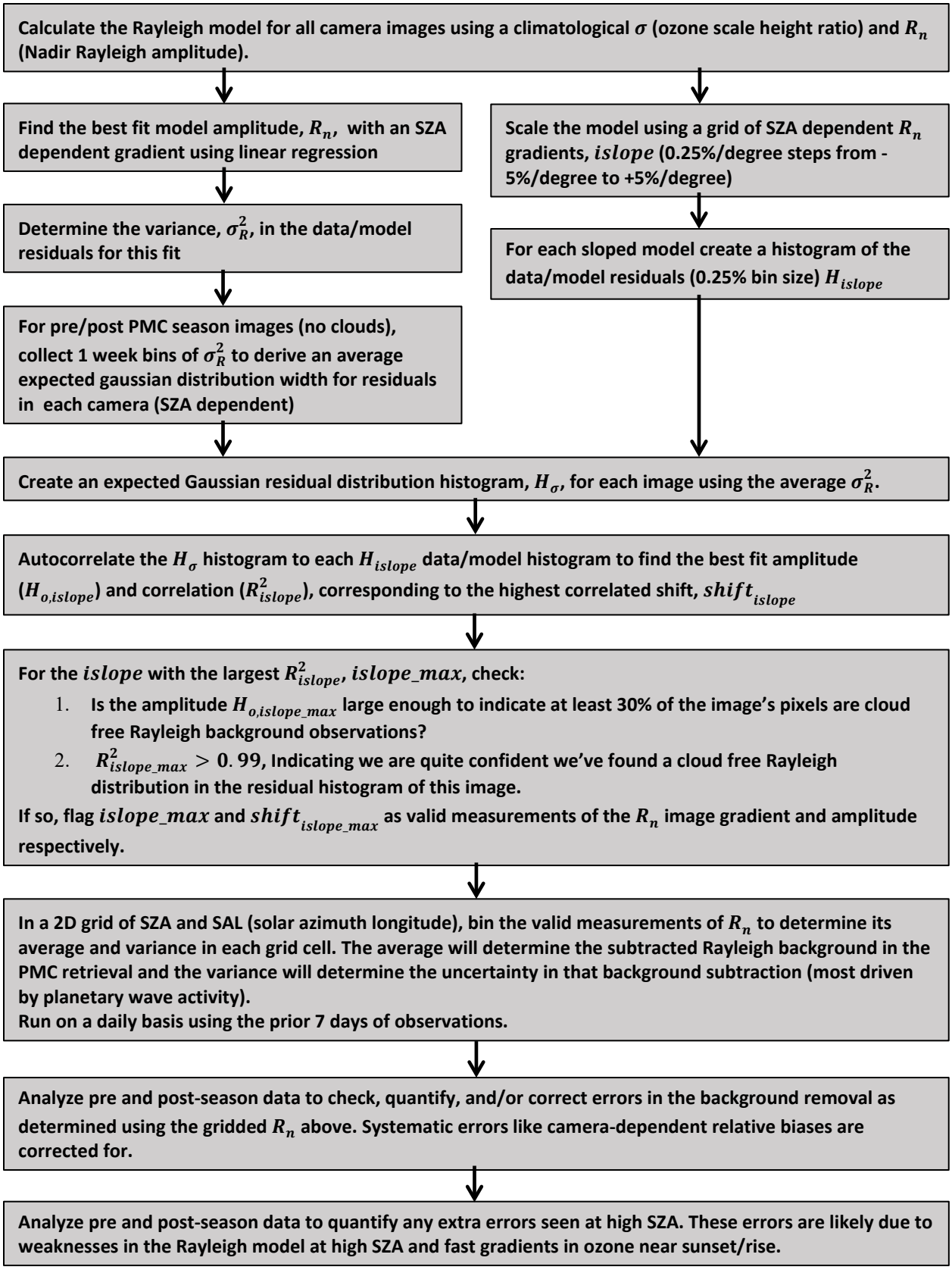

Figure 2.2.4.1-4 Flow diagram for the Rayleigh background determination algorithm.

2.2.4.2 PMC Cloud parameter retrieval

With the Rayleigh background removed, overlapping observations at different scattering angles in the same cloud parcels are collected into scattering profiles (or phase functions), P_{obs}. In order to retrieve cloud parameters such as the mode radius of the particle size distribution, *r*, and PMC cloud albedo (normalized to a scattering angle of 90 degrees), *A*, P_{obs} is fit to model phase functions, P_i, on a grid of potential mode radii, r_i, from 10 to 100 nm. The width assumptions used in these distributions are the same as described in *Lumpe et al.* [2013] for version 4.

The error due the background removal is highly correlated across the phase function, so a fitting algorithm that treats the errors at each scattering angle as independent will vastly underestimate the uncertainty. Further, as discussed in *Carstens et al. [2013]*, the radius retrieval is highly correlated with the error in the amplitude of the Rayleigh background subtraction. Subtracting too little Rayleigh will result in a flatter residual phase function consistent with a smaller *r*, and subtracting too much Rayleigh will have the opposite effect, so ignoring this correlated error effect will strongly lock in a radius bias associated with background subtraction errors.

To account for both of these problems, the phase functions are rotated into an alternate basis which isolates the component with the same shape as (parallel to) the Rayleigh background. This decorrelates the errors across the phase functions (P_i' and P_{obs}') since all of the uncertainty associated with Rn resides in a single component. The errors in the other components are smaller and mostly due to the uncorrelated pixel noise (Figure 2.2.2.3-1). χ^2 probability functions can be used in this alternate basis to compute retrievals that accurately reflect the errors we have quantified.

The optimal albedo for each radius, A_i, is calculated using a minimization of the χ^2 statistic. The χ^2 statistics are inverted into a relative probability function as a function of radius, p_i. The fits will give more latitude to deviations in the Rayleigh component while being more stringent in fitting the aspects of the phase functions which are independent of a background subtraction error. For the mode radius retrieval, *r*, and uncertainty, we can straightforwardly calculate the expectation values from p_i. For the albedo, we have uncertainty in each A_i and additional uncertainty propagating from the radius uncertainty because A_i can have a strong dependence on *r*. Both of those error terms are accounted for in the expectation value retrieval and uncertainty of the cloud albedo, *A*.

Cloud parameters are retrieved for every P_{obs} regardless of whether or not a cloud was present. Cloud identification is done by performing a χ^2 significance test of P_{obs} and computing a probability p_s that P_{obs} could have been created by the errors alone. This probability is stored in the Level 2 data files in the "*significance"* field and can be used for custom cloud identification thresholding. The default threshold is set very conservatively to a value of 10^{-7}.

The cloud albedo required to meet the detection threshold can be quite variable. Clouds with larger *r* are generally easier to detect for constant *A* because, while they have the same albedo at 90 degrees scattering angle, they will have larger directional albedos at smaller scattering angles. The scattering angle sampling of a given air parcel can impact the sensitivity for similar reasons. If we observe smaller scattering angles in a given parcel, the directional albedo will be larger allowing for clouds with smaller *A* to achieve significance. Further, variability exists in the

uncertainties such as larger Rn uncertainty in the presence of PW activity and higher noise uncertainty at higher view angles and solar zenith angles.

To quantify this variation in the sensitivity, we compute the minimum albedo required to meet the detection threshold for a grid of mode radii ([30, 45, 60, 75] nm) using the model phase functions, P_i. These sensitivities are output in the *cloud_albedo_sensitivity* field of the Level 2 files. Note that because of the uncertainties, a cloud meeting these albedo thresholds is not guaranteed to be detected. However, the errors are just as likely to make the significance value, p_s, artificially small as they are to make it artificially large, so the sensitivity values approximately mark the 50% probability of detection point. An example orbit strip of the sensitivity (*cloud_albedo_sensitivity* corresponding to the "worst-case" radius, usually the 30 nm value, and the "best-case", usually 75 nm) is shown in Figure 2.2.4.2-1. The general pattern of these sensitivity fields are fairly static from orbit to orbit because the sampling patterns change only with changes in the orbit (which happen slowly) or satellite operating mode (which happen infrequently), and sampling patterns are the main driver. However, small changes can occur more quickly in response to variations in planetary wave activity.

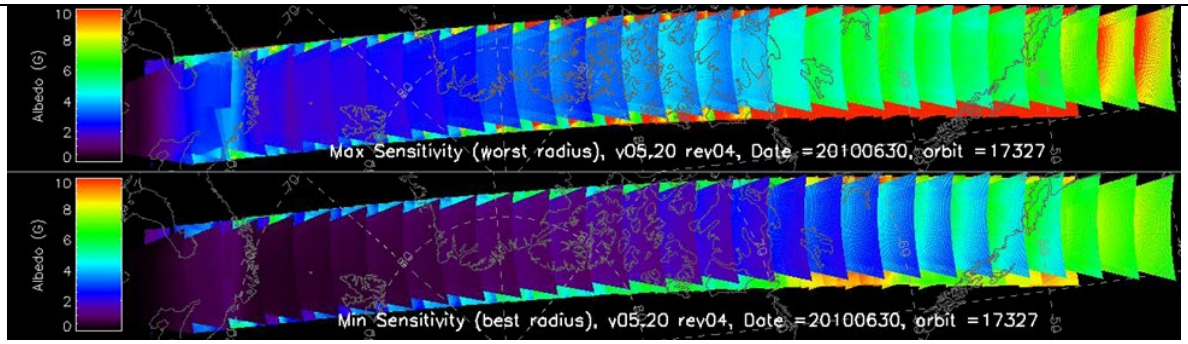

Figure 2.2.4.2-1 Example orbit strip of the minimum and maximum cloud albedo detection sensitivities.

These sensitivities are useful in interpreting metrics like frequency of occurrence for clouds above a given albedo threshold. For example, if you attempt to calculate a 2G frequency of occurrence using air parcels with sensitivities of only 5G, the contribution from these parcels is going to be artificially low because they are unable to detect any cloud that may be present for albedos in the 2-5G range. Instead, you should only use air parcels with sensitivities that meet the desired frequency threshold. The level 3C frequencies account for biases like these by ignoring insufficiently sensitive parcels in the calculations. For example, a parcel with a 5G sensitivity will only be used in frequency calculations with albedo thresholds of 5G or greater regardless of whether or not we have detected a cloud in it.

See Figure 2.2.4.2-2 for a flow diagram of the cloud parameter retrieval.

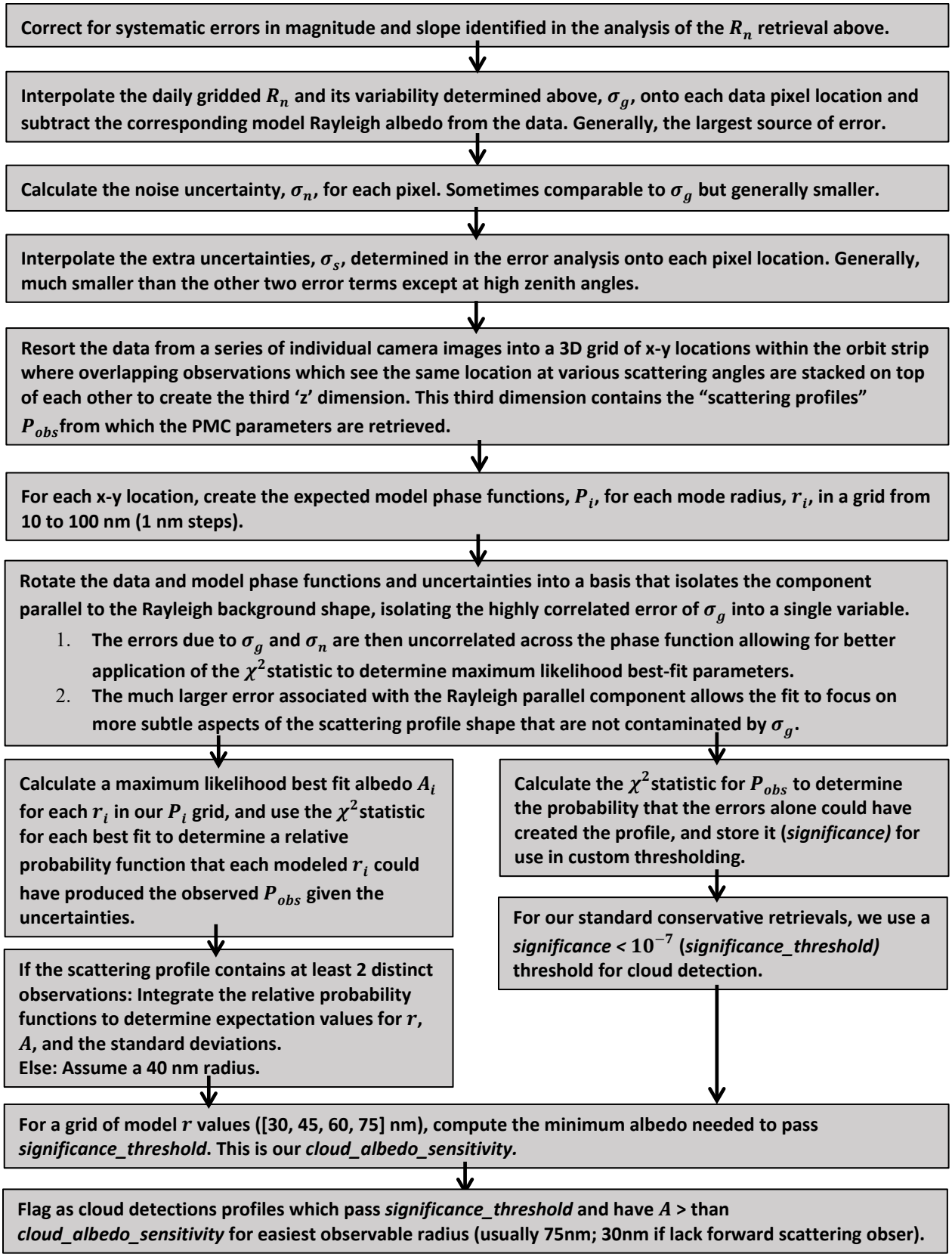

Figure 2.2.4.2-2 Flow diagram for the PMC parameter retrieval algorithm.

2.3. CIPS Calibration & Level 1A Processing

This section outlines the CIPS calibration process; more descriptions of the CIPS instrument and calibration are given by *McClintock et al.* [2009] and *Lumpe et al.* [2013]. Each image from each camera is calibrated separately, and the resulting calibrated images are stored in the level 1A data product. The calibration process is described by the equation and flowchart depicted in Figure 2.3-1. Note that while the fundamental steps of this process never change, some specific methods used to implement the calibration have changed over the AIM mission in response to changes in measurement sequences and satellite commanding constraints. These changes are noted in the description contained here.

The four CIPS cameras are denoted as PX, MX, MY and PY. As diagrammed in Figure 2.3-1, for most of the mission the X cameras are aligned fore and aft in the X (along-track) direction, while the nadir Y cameras are aligned in the Y (cross-track) direction (P represents "plus" and M represents "minus" relative to this coordinate system). While in full sun operations (~2017 - 2018), however, the cameras were yawed approximately 90° such that the X cameras were oriented cross-track with PX pointed toward the sunward side of the orbit track.

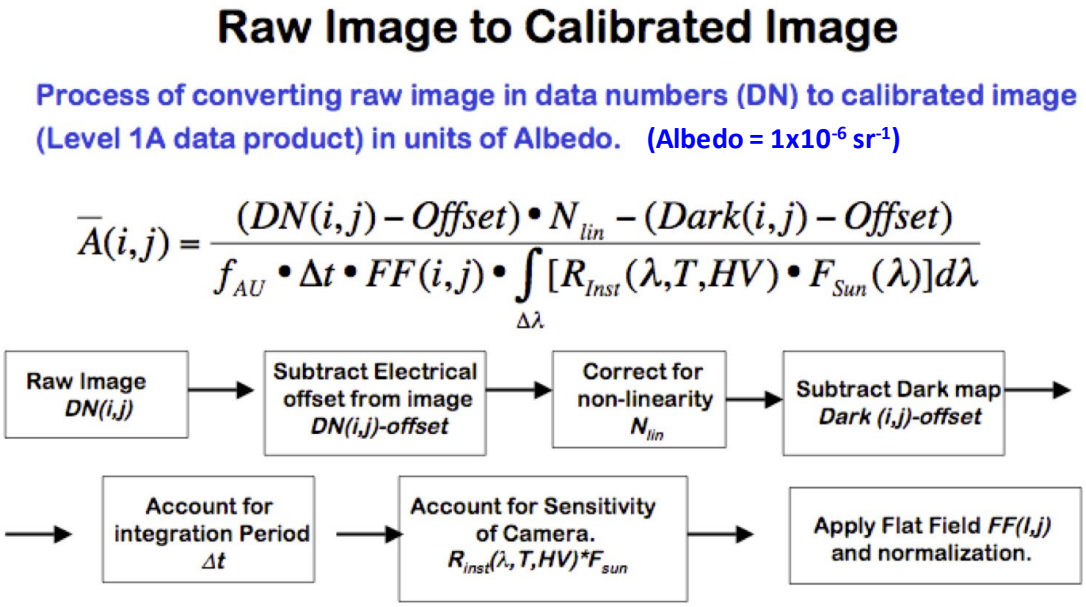

Figure 2.3-1. Flow chart illustrating the steps in the calibration analysis for converting level 0 data into level 1A, represented by DN(I,j) and A(I,j), respectively, in the equation at the top.

2.3.1. Dark Correction Maps

The first step in the calibration process is to subtract a dark image from each data image. Prior to 15 September 2011 one dark image (which is taken with the electrotonic shutter off) was obtained for each camera at the beginning and end of every third orbit, forming a pair. After this date, the CIPS data sequence was modified to obtain three dark images on every single orbit. To process each science image in an orbit, we first obtain from the Level 0 database a pair of "good"

dark images for each camera. To be "good", the pair cannot have missing data packets and must have a valid CCD temperature (obtained from housekeeping data) tagged to the image.

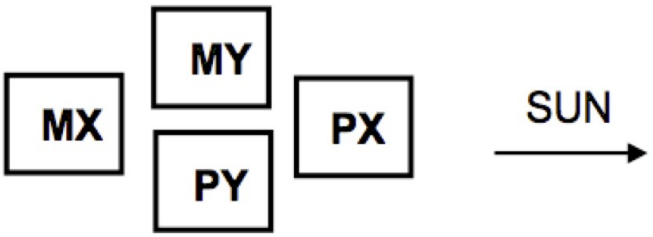

Figure 2.3-2. Orientation and definition of CIPS cameras.

Sometimes one or more of the dark images from a given orbit are noisy (have a higher standard deviation than normal). This can be caused by random particle hits, for example, or by the enhanced radiation environment if the orbit passes through the South Atlantic Anomaly. To avoid propagating dark image noise into the science data, the V4.20 algorithms have implemented a filtering technique to remove this noise. A smooth representation of the dark data is produced by performing a 2D (planar) fit to each image, which captures the magnitude and gradient of the dark image while eliminating the random noise component. This fit is then used to correct for the dark levels in the calibration analysis. Figure 2.3-3 shows an example of a relatively noisy dark image from one CIPS orbit, along with the smoothed representation used in the analysis.

Pre-flight testing of the camera dark characteristics indicated that the electrical offset and dark current are temperature dependent. Each camera CCD warms from usage, with the final image in an orbit taken at a temperature ~3° warmer than the cold first image. Therefore, the dark image pairs, with their associated temperatures, are used to linearly interpolate in temperature to determine an appropriate dark image to subtract from each science image in an orbit.

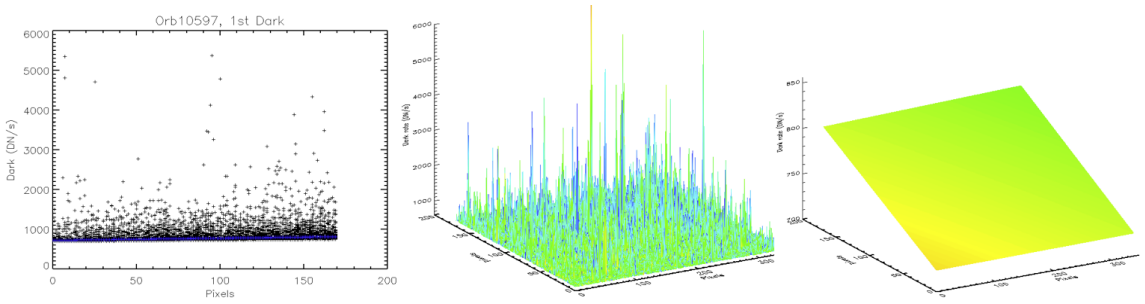

Figure 2.3-3. Sample dark image from CIPS orbit 10597. Left panel: scatter plot of the dark signal; black symbols are measured data and blue points are fitted representation. Middle panel: 3D representation of measured dark image. Right panel: fitted dark image used in the calibration.

2.3.2. Dark image electrical offset correction

The electrical offset is a baseline signal that is electronically added to each image on-board to avoid a negative readout. The electrical offset is added at the readout register on the CCD. Each dark image electrical offset is calculated using the minimum value from the dark image's first readable row. We subtract this electrical offset from each science image.

2.3.3. Dark map

The dark map is defined as the dark image with the electrical offset subtracted from it. The residual dark counts are random in nature, but there is a systematic increase of counts along the axis of the CCD readout direction in the readout register. The additional noise source is due to thermal noise that accumulates as the CCD is read out and is referred to as readout noise. In the image processing the dark offset is subtracted from the dark image to produce a dark map, which is then subtracted from the science image.

2.3.4. Non-Linearity

The "summing well" is the limiting charge collecting structure on the detector CCD. Pre-flight characterizations indicated that the CCD has a non-linear structure when the summing well exceeds the limiting charge. Therefore, we apply a non-linearity correction to the observed detector signal ($DN_{Observed}$):

$$DN_{true} = \frac{DN_{observed}}{1+\alpha \cdot DN_{observed}^2} \tag{2-13}$$

This relationship is valid for $DN_{Observed} < 1.5\times10^4$. The nonlinearity correction is applied to the science image after the electrical offset is subtracted. Values of α for a 4×8 binning for the individual cameras are shown in Table 2.3-1.

Table 2.3-1. Nonlinearity coefficients for 4×8 binning.

Camera	**Nonlinearity coefficient**
PX	-4.65×10^{-12}
PY	-6.28×10^{-12}
MX	-6.67×10^{-12}
MY	-6.14×10^{-12}

2.3.5. Integration period

The dark map and the science images are divided by the integration period (Δt in Fig. 2.3-1) to produce a unit detector count rate (DN/s). The nominal integration period is 1.024 seconds for the X cameras and 0.714 seconds for the Y cameras. At the same time a correction (f_{AU} in Fig. 2.3-1) is applied to compensate for the seasonal change in the Earth-Sun distance in normalizing to a standard solar flux.

2.3.6. Camera Radiometric Sensitivity and Micro-Channel Plate (MCP) gain correction

The radiometric sensitivity of each camera was determined in pre-flight testing. The radiometric sensitivity factors convert the detector count rate (DN/s) into albedo units (1 albedo unit = 10^{-6} sr^{-1}). Table 2.3-2 lists the camera radiometric sensitivity factors corresponding to intensifier voltage V=700 volts and a temperature of 22ºC.

Table 2.3-2. Radiometric sensitivity factors for converting detector signals (DN/s) to albedo units. These factors correspond to lab conditions of V=700 volts, T=22ºC.

Camera	**4×8 binning (DN/sec/albedo)**
PX	742.7
MX	1300.5
PY	618.7
MY	596.5

Preflight testing determined that the MCP gain correction varies with the CCD temperature and the high voltage. A correction of the functional form below was determined from laboratory calculations. The best-fit parameters for each camera are listed in Table 2.3-3. Each science image is divided by the radiometric sensitivity correction and multiplied by the MCP gain correction. At this point all images are in albedo units.

$$G(HV,T) = A_0(\alpha_{3+}\alpha_4 \cdot T) \cdot e^{\alpha_1 \cdot (HV-700)+\alpha_2 \cdot (HV-700)^2}$$
$$A_0 = (\alpha_3 + 25.0 \cdot \alpha_4)^{-1} \quad (2\text{-}14)$$

Table 2.3-3. Best-fit parameters for correcting the radiometric gain factors for dependence on detector high voltage and temperature.

Camera	**MCP Gain Coefficients**		**Temperature Gain Coefficients**	
	a_1	**a_2**	**a_3**	**a_4**
PX	0.0161378	-9.61494e-06	1.02859	-0.00418869
PY	0.0153218	-1.02052e-05	1.01431	-0.00450727
MX	0.0163646	-9.77719e-06	1.02406	-0.00441509
MY	0.0149232	-9.55688e-06	1.03924	-0.00477110

2.3.7. Flat Field correction and camera-to-camera normalization

Flat Field

The flat field is the pixel-to-pixel variation of the camera due to the lens system and the photocathode. Each raw camera image is dominated by the flat field variation, as illustrated in Figure 2.3-4, which shows both laboratory and non-calibrated flight images for uniform illumination scenes. The non-calibrated scene looks very similar to the lab flat field scene. The flat field variation was mapped out in pre-flight laboratory testing. The variation is normalized to unity in the center of the image, providing a pixel-by-pixel correction factor that is divided out of each science image in the calibration process.

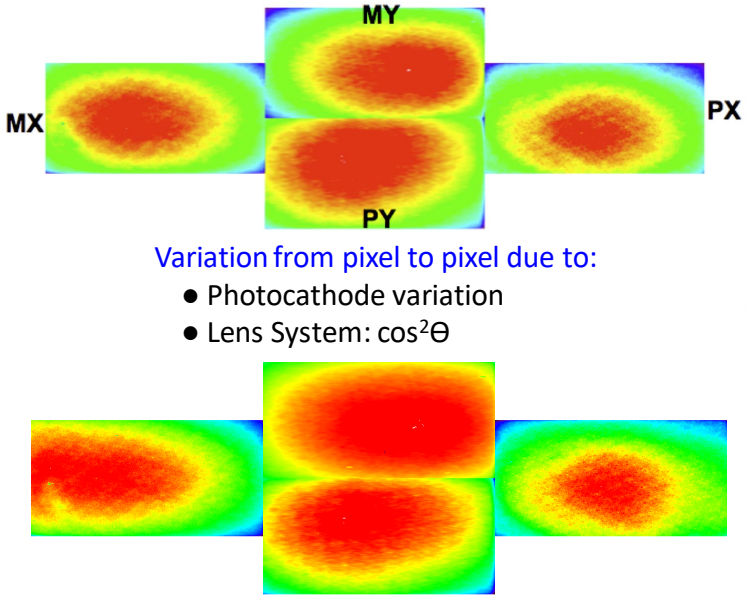

Figure 2.3-4. Flat field images obtained in the laboratory pre-flight calibration (top). Un-calibrated in-flight images (bottom).

Delta Flat Field

The laboratory flat field correction described above should have removed all instrument-induced pixel-to-pixel variation from the cameras. However, when the first on-orbit science images were processed it was evident that there was residual variability across the detector. We refer to this residual as the Delta Flat Field (or Δ-flat for short), as it is a secondary correction to the laboratory flat fielding. This residual non-uniformity must be corrected in the calibration procedure to avoid systematic biases in the CIPS cloud retrievals. The CIPS team has developed additional calibration procedures that make use of special operational datasets obtained on-orbit to characterize and remove this residual variation.

To obtain an accurate estimate of the Δ-flat field we require a uniformly illuminated camera image, a condition that, on orbit, is best realized at the subsolar point in nadir viewing geometry. This scenario has the advantage of minimizing the solar zenith and satellite view angles (thus minimizing scattering angle variation) as well as atmospheric (e.g., ozone) variation across the

image. New satellite and instrument commands were devised to obtain CIPS images from each camera at the subsolar point on consecutive orbits at different times during the year. These "special_1a" images are taken either before (SH) or after (NH) the normal science data sequence. The AIM satellite is rotated so that one camera is pointed directly nadir for a series of images, and the sequence is rotated through the four cameras on sequential orbits. These nadir subsolar images are calibrated and then compared to a simulated albedo image calculated from a Rayleigh scattering atmospheric model using the identical viewing geometry (for more details on the model see the level 2 algorithm documentation).

This so-called C/σ Rayleigh model is characterized by two parameters – the ozone column density above a reference altitude (C) and the ratio of the ozone and atmospheric scale heights (σ). Both are assumed constant across the image in the model calculation. The measured subsolar image is then divided by the model image and the resulting ratio is normalized to unity at the image center, to isolate the pixel-to-pixel variation and eliminate any absolute offset between model and data. This process is performed for all subsolar images separately, and the results are averaged to beat down random noise. The result is a final Δ-flat image for each camera for each season, which is then multiplied by each science image at the last stage in the calibration process. The residual variation observed is on the order of 4% for PY, MY and MX and up to 11% for PX, and shows significant structure across the camera. A sample set of Δ-flat images is shown in Figure 2.3-5.

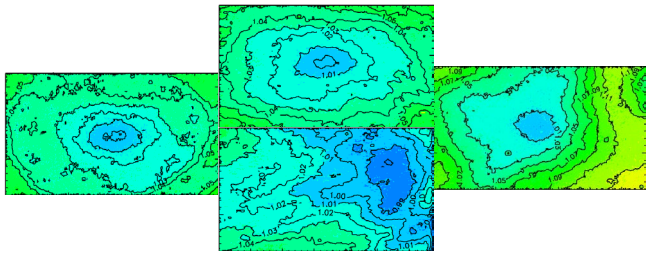

Figure 2.3-5. Delta flat field images used for the NH 2009 season. Observed patterns in the pixel-to-pixel structure are similar from year to year.

The assumption of constant ozone across the camera field of view in the model calculations necessarily introduces some error into this analysis. Comparison with results from an independent technique based on statistical analysis of overlapping pixels obtained from special fast-cadence images indicates that the operational V4.20 calibration could still have systematic flat field errors up to 1.5% across the cameras (along track direction). While this error seems small, it does affect the retrieval of the dimmest clouds. Because 1.5% of 200 albedo units (a typical background albedo measured by CIPS) is 3 albedo units, the threshold for cloud detection can vary by 3 albedo units across the detector. This is significant compared to the brightness of the dimmest clouds CIPS detects, which are less than 10 albedo units. We are currently working on new calibration methods with the goal of reducing the systematic flat fielding errors to better than 0.5% in the next CIPS data version.

2.3.8. Camera-to-Camera normalization

The instantaneous field of view of each camera overlaps that of other cameras as illustrated in Figure 2.3-6. The basic CIPS measurement technique involves combining spatially coincident measurements from different cameras, made at different scattering angles, to construct a measured scattering profile (albedo vs. scattering angle). Hence it is critical that the calibration enforce consistent normalization between the cameras. The flat field correction described above is solely

concerned with fixing the correct pixel-to-pixel variation across each camera, and thus leaves undetermined an overall calibration constant. The final step of the calibration procedure is then to normalize the relative sensitivity of each camera to the others, which we do by forcing the ratios of observed albedo in these overlapping pixels to be equal. This requires that one camera be used as a standard against which to normalize the others, and the MY camera is chosen because it exhibits the most stable long-term trends.

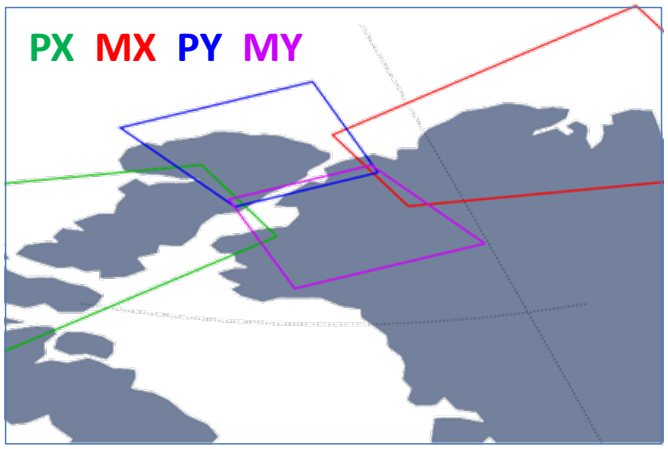

Figure 2.3-6. CIPS camera footprints at clod deck altitude from a typical scene. A CIPS scene consists of images from all four cameras taken simultaneously. Each of the nadir (Y) cameras overlaps all other cameras along some edge pixels, while the PX and MX cameras overlap both Y cameras.

CIPS measures one extra scene every sixth orbit at low latitudes, outside the normal range of science images where PMCs occur. These images are referred to as "low latitude flats" (LL Flats). Similar to the subsolar images described above, these images are obtained in conditions of relatively uniform illumination and low atmospheric variability. Using this data a normalization factor is obtained for each camera (PX/MX/PY) from each scene by calculating the mean albedo ratio in all overlapping MY pixels. Figure 2.3-7 shows these normalization factors over the entire AIM mission to date. Each vertical line represents a separation of PMC seasons (NH to SH measurements or vice versa). The red circles represent the median normalization in each PMC season and are the factors used in the final calibration process. Obviously, this full season average, while always available for reprocessing of past data, is not available for routine operational processing of the current season. For each new season the V4.20 algorithm starts out using □-flat and normalization factors obtained from preseason subsolar data, if available. It is sometimes the case that new calibration data has not been obtained before the start of a cloud season, since commanding for these special measurements requires satellite bitlock to uplink commands, and this has been problematic for the AIM mission. In this situation we start operations with the previous year's calibration data (the situation has changed as of September 2011 – please see the discussion that follows). This does not generally present a problem as the Δ-flats are consistent year-to-year. (The normalization factors, as Figure 2.3-7 shows, do exhibit trends at the 1-2%/year level, so this is more problematic). At the end of each season we re-calculate a final calibration using all available data and re-process the full season for consistency. Because each season uses a different set of delta flats (defined above) there can be jumps in the normalizations between seasons. We are investigating the decreasing trend of the PX and MX normalizations. In addition, we are investigating the relatively larger discontinuities in the MX and PY normalization in the transition from NH to SH observations.

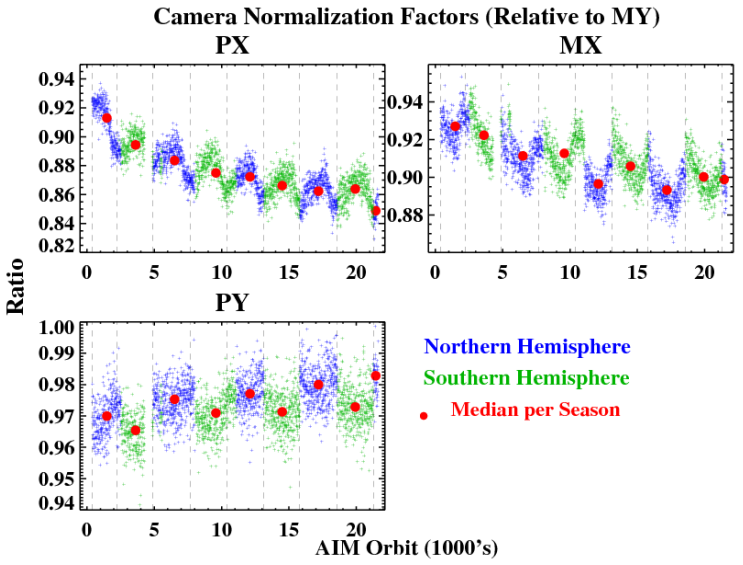

Figure 2.3-7. Camera normalization factors for the first five years of the CIPS mission. Blue (green) symbols represent Northern (Southern) Hemisphere data for each individual low-latitude scene. The red circles are the median value for each season, used in final definitive processing.

As of September 2011, due to constraints imposed by loss of satellite bitlock, CIPS is no longer making the "special_1a" subsolar measurements described above. However, the LL Flat images are suitable for use instead of the subsolar images for the purposes of calibration. While the viewing geometry is not as ideal, this data set has the advantage that there are many more images to work with, and they are available continuously throughout the year. This allows us to average many more Δ-flat images to reduce random error, and in principle opens up the possibility for doing time-dependent calibration during a season. Each LL Flat scene provides a self-consistent measurement of both the Δ-flat field for all four cameras, as well as the normalization factors. Also, beginning in September 2011 the CIPS measurement sequence was modified to obtain two LL Flat scenes every orbit, thereby increasing the data density significantly. All CIPS seasons from Southern Hemisphere 2011/2012 and later will use calibration obtained from this data source.

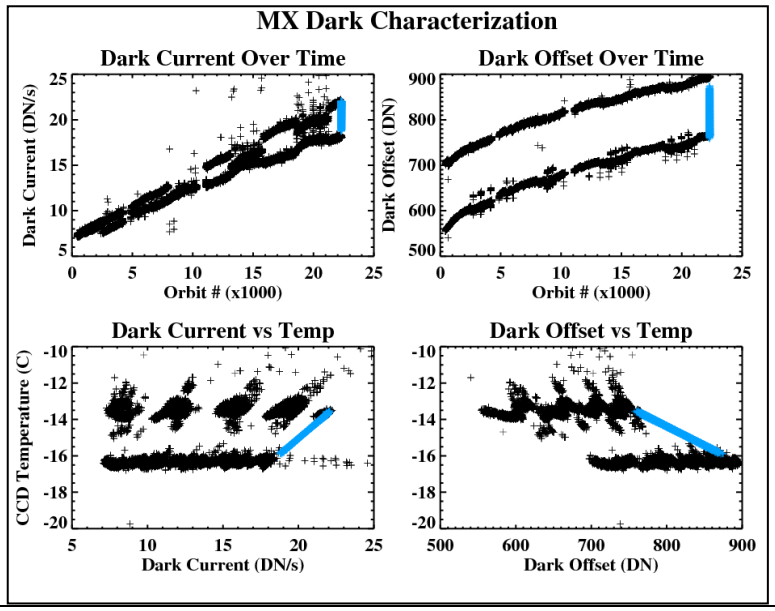

Figure 2.3-8. Trends of the dark current and dark offset for the MX camera.

2.3.9. Trends in calibration variables

Dark Trends

Figures 2.3-8 and 2.3-9 show mission trend plots of variables from the calibration process. Figure 2.3-8 shows trends in the dark current and dark offset from the dark dataset (black data points). The dark datasets, as discussed in section 2.3.3, are taken for each camera at the beginning and end of every third orbit before September 2011, and every orbit thereafter. Ten dark images per camera were taken each mission day before September 2011and 45 since then. As determined in laboratory measurements, the darks vary with CCD temperature. The CCD temperature warms ~3º over an orbit from usage between the first and last dark images. The two top plots show that the dark current and dark offset for the MX camera increased by ~10% over the mission. The two distinct lines in these plots are due to the dark variation with the CCD temperature. The dark current and dark offset are plotted against CCD temperature in the two bottom figures.

The blue data points represent the temperature-interpolated values from the most recent CIPS data in the time period shown. The dark images taken at the beginning and end of the orbit should bracket the interpolated data. This is a good check to make sure that the darks are interpolated correctly. We only show the MX camera because the other cameras are very similar. Although cameras are getting noisier it seems to be fairly systematic and the camera degradation appears to be very slow. More than four years into the mission the cameras are still very quiet and have good signal to noise.

2.3.10. Calibration Diagnostics

Figure 2.3-9 shows of the trend of single value calibration diagnostics for the MX camera. These variables are analyzed routinely to determine if the camera is behaving as expected. The High Voltage (per image), CCD temperature (per image), MCP Gain (corrects sensitivity for temperature and high voltage) and Nonlinearity correction are shown. The black points represent the values corresponding to the dark images. The blue points represent science image data from recent orbits. The operational Level 1A processing codes were modified in V4.20 to save out all

these critical single value diagnostic variables for every single CIPS image in the Level 1A data files. This makes it much easier than in previous data versions to routinely access these quantities and check for trends and anomalies.

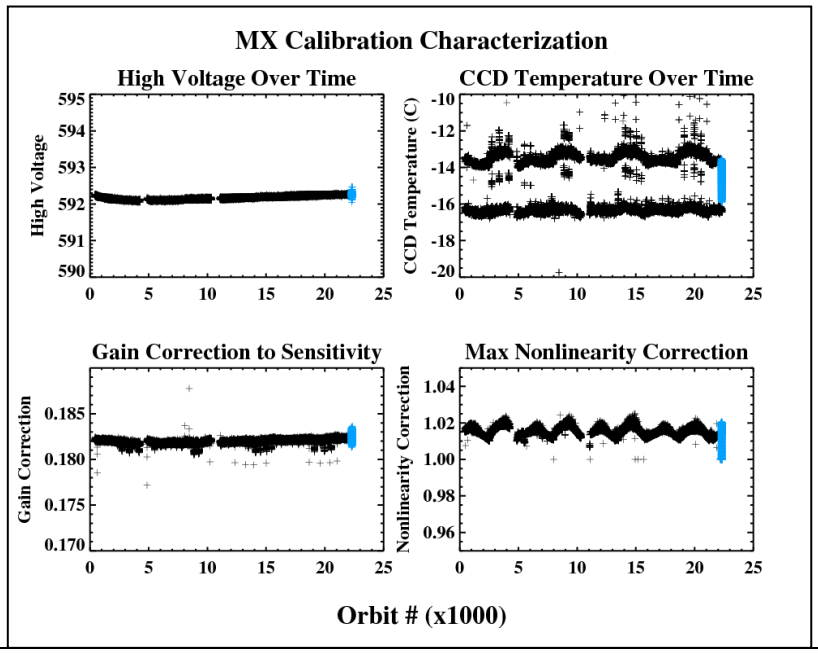

Figure 2.3-9. Similar to Figure 2.3-8, but here showing the time trends of high voltage, CCD temperature, gain correction, and non-linearity factors for the MX camera.

2.4. CIPS References

Bailey, S. M., G. E. Thomas, D. W. Rusch, A. W. Merkel, C. Jeppesen, J. N. Carstens, C. E. Randall, W. E. McClintock, and J. M. Russell III (2009), Phase functions of polar mesospheric cloud ice as observed by the CIPS instrument on the AIM satellite. Journal of Atmospheric and Solar–Terrestrial Physics 71 (3–4), 373–380.

Bates, D.R., Rayleigh scattering by air. *Planet. Space Sci.* 32, 785–790, 1984.

Baumgarten, G., A. Chandran, J. Fiedler, P. Hoffman, N. Kaifler, J. Lumpe, A. Merkel, C. E. Randall, D. Rusch, and G. Thomas, On the horizontal and temporal structure of noctilucent clouds as observed by satellite and lidar at ALOMAR (69N), *Geophys. Res. Lett.*, 39, L01803, doi:10.1029/2011GL049935, 2012.

Baumgarten, G., Fiedler, J., and Rapp, M. (2010), On microphysical processes of noctilucent clouds (NLC): observations and modeling of mean and width of the particle size-distribution, *Atmos. Chem. Phys.*, 10, 6661-6668, doi:10.5194/acpd-10-6661-2010.

Carstens, J. N., S. M. Bailey, J. D. Lumpe, and C. E. Randall (2013), Understanding uncertainties in the retrieval of polar mesospheric clouds from the cloud imaging and particle size experiment in the presence of a bright Rayleigh background, *J. Atmos. Sol. Terr. Phys.*, *104*, 197–212, doi:10.1016/j.jastp.2013.08.006.

DeLand, M. T., E. P. Shettle, G. E. Thomas, and J. J. Olivero (2003), Solar backscattered ultraviolet (SBUV) observations of polar mesospheric clouds (PMCs) over two solar cycles, J. Geophys. Res., 108(D8), 8445, doi:10.1029/2002JD002398.

Hervig, M.E., L.L. Gordley, M. Stevens, J.M. Russell, S. Bailey, and G. Baumgarten (2009),

Interpretation of SOFIE PMC measurements: Cloud identification and derivation of mass density, particle shape, and particle size, *J. Atmos. Solar-Terr. Phys.*, *71*, 316-330, doi:10.1016/j.jastp.2008.07.009.

Lumpe, J.D., S.M. Bailey, J.N. Carstens, C.E. Randall, D.W. Rusch, G.E. Thomas, K. Nielsen, C. Jeppesen, W.E. McClintock, A.W. Merkel, L. Riesberg, B. Templeman, G. Baumgarten, J.M. Russell, IlI (2013), Retrieval of polar mesospheric cloud properties from CIPS: algorithm description, error analysis and cloud detection sensitivity, *J. Atmos. Solar-Terr. Phys*, 104, 167-196, http://dx.doi.org/10.1016/j.jastp.2013.06.007.

McClintock, William, D.W. Rusch, G.E. Thomas, A.W. Merkel, M.R. Lankton, V.A. Drake, S.M. Bailey, and J.M. Russell III, The Cloud Imaging and Particle Size experiment on the Aeronomy of Ice in the Mesosphere mission: Instrument concept, design, calibration, and on-orbit performance, J. Atmos. Solar-Terr. Phys., doi:10.1016/j.jastp.2008.10.011, 2009.

McPeters, R.D. (1980), The behavior of ozone near the stratopause from two years of BUV observations. Journal of Geophysical Research 85, 4545–4550.

McPeters, R.D. and G. J. Labow, Climatology 2011: an MLS and sonde derived ozone climatology for satellite retrieval algorithms, JOURNAL OF GEOPHYSICAL RESEARCH, doi:10.1029/2011JD017006.

Mischenko, M. I., and L. D. Travis, Capabilities and limitations of a current FORTRAN implementation of the T-matrix method for randomly oriented, rotationally symmetric scatters, *J. Quant. Spectrosc. Radiat. Transfer*, 60, 309-324,1998.

Randall, C. E., et al. (2017), New AIM/CIPS global observations of gravity waves near 50–55 km, *Geophys. Res. Lett.*, 44, 7044– 7052, doi:10.1002/2017GL073943.

Thomas, G.E. and C. P. McKay (1985), On the mean particle size and water content of polar mesospheric clouds. *Planet. Space Sci. 33* (10), 1209–1224.

Warren, S. G. (1984), Optical constants of ice from the ultraviolet to the microwave, *Appl. Optics* 23, 11906-11,926.

3. The Solar Occultation For Ice Experiment (SOFIE)

3.1. SOFIE Overview

SOFIE conducts solar occultation measurements at 16 wavelengths (spectral bands) that are used to retrieve vertical profiles of temperature, O_3, H_2O, CO_2, CH_4, NO, and extinction due to PMCs and meteoric smoke at multiple wavelengths from 0.330 to 5.006 μm [*Gordley et al.*, 2009]. SOFIE performs 15 sunset and 15 sunrise measurements each day. The measurements offer high sensitivity due to the long atmospheric path length (~300 km) combined with the bright solar source and a precise electro-optical system. SOFIE provides ~1.6-km vertical resolution and the high precision allows retrievals on the over-sampled 200 m vertical grid. Multi-wavelength extinction measurements are used to determine an unprecedented variety of physical PMC properties including ice volume density, ice water content, particle shape, ice concentration and size, ice particle temperature, and the amount of meteoric smoke contained in ice [*Hervig et al.,* 2009; *Hervig and Gordley*, 2010; *Hervig et al.,* 2012]. SOFIE made the first observations of meteor smoke from satellite [*Hervig et al.*, 2009], which were most recently used to determine the chemical composition of meteoric smoke, and provide a new estimate of the meteoric influx into Earth's atmosphere [*Hervig et al.*, 2017b]. Before 2016, latitude coverage was from 65° to 82° in both hemispheres at local solar times near midnight during summer. As the AIM orbit changed, SOFIE coverage spanned tropical to polar latitudes in 2016, and in 2018 SOFIE sunrise/sunset latitudes switched hemispheres. A return to continuous coverage of polar latitudes occurred in 2020 (see Figure 3.1).

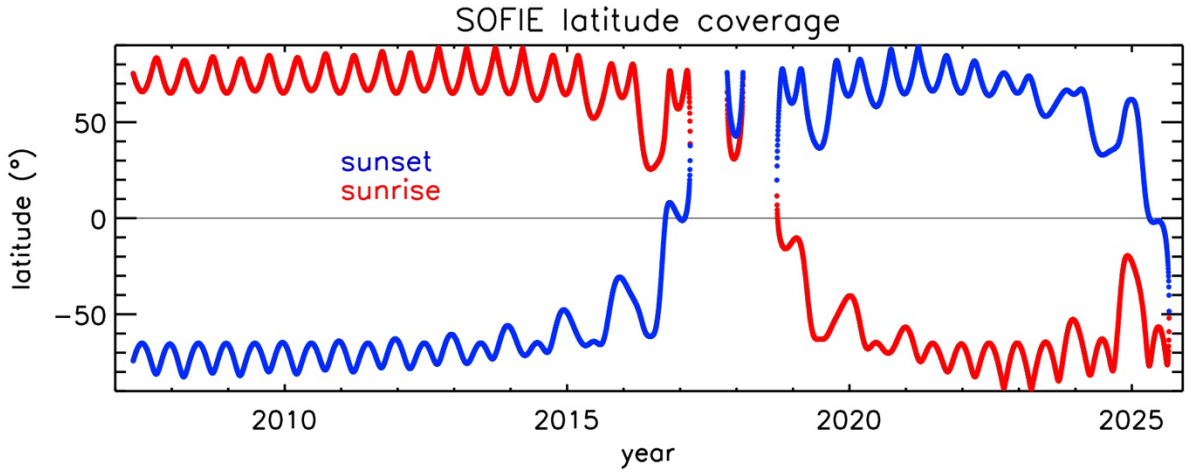

Figure 3.1. The latitude of SOFIE sunrise and sunset observations. Note that sunrise measurements were suspended in October 2020.

3.1.1. SOFIE Heritage

SOFIE draws heritage from the Halogen Occultation Experiment (HALOE), which conducted solar occultation measurements from the UARS satellite during 1991 - 2005 [*Russell et al.*, 1993].

3.1.2. SOFIE Product Description

Table 3.1.2 gives a detailed description of the SOFIE science retrieval products.

Table 3.1.2. SOFIE Version 1.3 Data Product Description.		
Product Measurement (Wavelength)	**Altitudes**[1]	**Status and Validation**
Temperature band 13 (4.324 μm) refraction (0.701 μm)	10 -102 km	The SOFIE temperature (T) product is based on T retrieved from refraction angle measurements at altitudes from the tropopause to ~50 km, and T retrieved from the 4.324 μm CO_2 band at altitudes from ~50 km to 105 km. V1.3 uses CO_2 from a recent version of WACCM (ref 2c) and atomic O from SABER. These changes can impact retrieved T(P) significantly above 70 km. Atomic O is important in the CO_2 NLTE model as it is one of the primary gases that quench excited states of CO_2 [*Marshall et al.*, 2011]. Validation of SOFIE temperatures indicates agreement with independent observations to within reported systematic uncertainties [*Stevens et al.,* 2012; *Sheese et al.*, 2012; *Garcia-Comas et al*., 2014; *Hervig et al.*, 2016b].
H_2O band 6 (2.618 μm)	17 - 95 km	H_2O is retrieved using band 6. Note that the SOFIE H_2O measurements are unaffected by PMC contamination. *Rong et al.* [2010] compared SOFIE V1.022 to MLS and ACE, and report differences within ~10% in the NH, and that SOFIE was low by ~20% in the SH. SOFIE V1.3 is similar. See also *Tschanz et al.* [2013] and *Khosrawi et al.* [2018].
O_3 band 1 (0.291 μm)	20 - 105 km	O_3 is retrieved above 55 km using band 1 (291 nm), and include a correction for PMC contamination based on an extrapolation of the band 2 (330 nm) PMC extinction in wavelength. These corrections occur after November 2009, when band 2 (came out of saturation. Band 2 measurements are used to retrieve O_3 below ~60 km, after November 2009. These results are merged with the band 1 profiles to form a product that covers ~20 - 105 km. *Smith et al.* [2013] compared SOFIE to SABER and report differences within ~0.2 ppmv at 60 - 10 km. *Rong et al.* [in prep] compared with ACE and found differences within ~1% for 55 - 93 km.
CH_4 band 11 (3.384 μm)	21 - 80 km	The CH_4 retrievals are currently useful below ~78 km. At higher altitudes, the signal-to-noise is low, and the retrievals are contaminated when PMCs are present. *Laeng et al.* [2015], compared SOFIE to MIPAS, and reported differences within 0.02 ppmv for 45-70 km, and an occasional high bias in SOFIE below ~30 km.

NO band 16 (5.316 μm)	35 - 149 km	NO is retrieved from band 16 measurements, which require a signal correction to remove a damped oscillation that is traced to varying detector temperatures. In V1.3 SOFIE NO is also reported as number density profiles (molecules cm^{-3}). For scientific studies using SOFIE NO see *Baily et al.* [2014] and *Hendrickx et al.* [2015]. *Gomez-Ramirez et al.* [2013], compared to ACE at 97-106 km: within ~15% in the NH, SOFIE low by 5-35% in the SH. *Hervig et al.* [2019] report a full error analysis, and compared SOFIE to MIPAS and ACE NO showing agreement to within 50% from ~40 - 140 km.
CO_2 band 13 (4.324 μm)	30 - 55	CO_2 retrievals were first implemented in V1.2, independently using bands 7 and 13. The results are valid at altitudes where temperature is retrieved from refraction angle measurements (30 - 55 km). CO_2 will be released to the public in V1.4. SOFIE CO_2 is within 2% of WACCM model results. Compared to SCIAMACY measurements, SOFIE is within 2% over 30-45 km. SOFIE sunrise and sunset measurements are not coincident, but CO_2 is well mixed and thus the rise - set comparisons are useful. The sunrise and sunset CO_2 are within 2% of each other.
UV Aerosol Extinction band 2 (0.330 μm)	17 - 95 km	The primary goal of this measurement is PMCs. Band 2 was saturated from launch until November 2009. By this point darkening of the optics had reduced the incoming UV light enough to bring the detector out of saturation. PMC extinction in band 2 is strong, and only slightly lower than the strongest IR bands (8 - 10). Use of these measurements for PMCs is discussed in *Hervig et al.* [2012]. V1.3 PMC extinctions and resulting PMC properties are similar to V1.2.
NIR Aerosol Extinction bands 3 & 4 (0.867 & 1.037 μm)	17 - 95 km	The primary goal of these measurements is PMCs. The NIR extinctions, $\beta(\lambda)$, can be very low, such that these measurements often do not respond to PMCs that are detected by the IR bands. While the NIR PMC extinction is best characterized using the high gain difference of bands 3 and 4 (channel 2), bright PMCs are well represented by bands 3 and 4. These measurements were used to characterize meteoric smoke in the upper stratosphere and mesosphere [*Hervig et al.*, 2009]. Note that this was accomplished by averaging the signals *before* retrieving extinction, in order to reduce the noise, and thus prevent a high bias in extinction when the transmissions are near unity. This step is required to use the extinctions for smoke studies.

NIR Aerosol Extinction channel 2 difference signal (extinction at 0.867 μm minus that at 1.037 μm wavelength)	41 - 110 km	The primary goal of this measurement is PMCs. This measurement is the difference of aerosol extinction at 0.867 μm minus that at 1.037 μm wavelength (band 3 - band 4). The difference signal experiences an electronic gain of 300, and thus is not digitization-limited like the component bands 3 and 4 measurements. Thus this is the recommended measurement for characterizing PMCs in the NIR. As of V1.2 the channel 2 dV extinction retrieval was reformulated to yield the exact 0.867 - 1.037 μm extinction difference. Previous versions used the theoretical ratio of 0.867/1.037 μm PMC extinction (2.0). Use of these measurements for PMCs is discussed in *Hervig et al.* [2009; 2012]. V1.3 PMC extinctions and resulting PMC properties are similar to V1.2.
IR Aerosol Extinction band 5 (2.462 μm)	17 - 110 km	*This measurement is not recommended for scientific use.* The band 5 extinctions are typically biased high relative to expectations based on the other PMC measurements. This problem is thought to be due to gaseous interference that is not being removed correctly, and/or signal drifts that are not properly removed.
IR Aerosol Extinction band 8 (2.939 μm)	17 - 110 km	The primary goal of this measurement is PMCs. This wavelength has one of the highest PMC signals, as it is located near the peak of the OH-stretch region of the ice spectrum. This is an excellent measurement for characterizing PMCs. Use of these measurements for PMCs is discussed in *Hervig et al.* [2009] and *Hervig and Gordley* [2010]. V1.3 PMC extinctions and resulting PMC properties are similar to V1.2.
IR Aerosol Extinction bands 9 & 10 (3.064 & 3.186 μm)	17 - 95 km	The primary goal of this measurement is PMCs. These wavelengths have the highest PMC signals of all of the SOFIE measurements. They were located near the peak of the OH-stretch region of the ice spectrum. These bands are used to identify PMCs in SOFIE profiles, and band 9 is the basis for determining ice mass density (and IWC). These are excellent measurements for characterizing PMCs. Use of these measurements for PMCs is discussed in *Hervig et al.* [2009; 2012] and *Hervig and Gordley* [2010]. V1.3 PMC extinctions and resulting PMC properties are similar to V1.2.
IR Aerosol Extinction band 12 (3.479 μm)	17 - 110 km	The primary goal of this measurement is PMCs. Band 12 extinctions are consistent with the other observations, considering the wavelength dependence expected for PMCs. V1.3 PMC extinctions are similar to V1.2.

IR Aerosol Extinction band 14 (4.646 μm)	17 - 110 km	*This measurement is not recommended for scientific use.* The band 14 extinctions are typically biased high relative to expectations based on the other IR measurements. This problem is thought to be due to gaseous interference that is not being removed correctly, or signal drifts that are not properly removed.
IR Aerosol Extinction band 15 (5.006 μm)	17 - 110 km	The primary goal of this measurement is PMCs. Band 15 extinctions are consistent with the other observations, considering the wavelength dependence expected for PMCs. V1.3 PMC extinctions are similar to V1.2.
PMC Physical Properties multi-wavelength extinctions: chan. 2 difference; 0.330, 2.939, 3.064, and 3.186 μm	PMC altitudes	The following PMC parameter retrievals are described in detail by *Hervig et al.* [2009; 2012] and. *Hervig and Gordley.* [2010]. All are determined vs. altitude, except the last three which are from vertical integrals. • Ice layer top altitude (km) • Altitude of peak 3.064 μm extinction (Z_{max}) (km) • Ice layer bottom altitude (km) • Ice volume density ($\mu m^3\ cm^{-3}$) • Ice mass density ($g\ km^{-3}$) • Axial ratio of oblate & prolate spheroids • Ice temperature, ice-T (K) • Axial ratio of oblate spheroid, retrieved simultaneously w/ ice-T • Gaussian size distribution parameters (assuming pure ice): concentration (cm^{-3}), median radius (nm), width (nm) • Effective radius (nm) • Volume fraction of meteoric smoke in ice • Gaussian size distribution parameters and effective radius retrieved assuming ice-smoke mixture • Vertical ice water column abundance, or IWC ($g\ km^{-2}$) • Vertical optical depths (OD) for all wavelengths • Gaussian size distribution parameters retrieved from OD
Aerosol Extinction in the stratosphere General statements for all wavelengths.	> ~17 km	SOFIE reports aerosol extinctions for various wavelengths at altitudes from roughly 17 - 95 km. These results are currently not suitable for studies of the stratospheric aerosol layer. This limitation is due primarily to incomplete removal of gaseous interference, deficits in the signal drift corrections, and treatment of the FOV and solar refraction at low altitudes. While the deficiencies are generally understood, the focus of SOFIE extinctions is PMCs and improvements directed at stratospheric aerosol measurements are of a lower priority.

[1]The tropopause altitude at polar latitudes is ~9 km. PMC are detected at altitudes from roughly 80 - 92 km.

3.2. SOFIE Theoretical Description

SOFIE measures vertical profiles of limb path atmospheric transmission within 16 spectral bands between 0.29 and 5.32 μm wavelength. Occultation measurements are accomplished by monitoring solar intensity as the satellite enters or exits the Earth's shadow (spacecraft sunrise or sunset). The ratio of solar intensity measured through the atmosphere (V, endoatmospheric) to the intensity measured outside the atmosphere (V_0, exoatmospheric) yields broad band atmospheric transmission, $\tau = V/V_0$, which is the basis for retrieving the desired geophysical parameters. Because the endoatmospheric and exoatmospheric intensities are measured using the same electro-optical system, absolute response errors are nearly eliminated in the resulting atmospheric transmission measurements.

SOFIE performs broadband differential absorption measurements using eight channels. Each channel consists of two broadband radiometer measurements, one located in a wavelength region of strong absorption (V_S) and one in a spectrally adjacent region of weaker absorption (V_W) (see Table 2-1). SOFIE also measures the radiometer difference signal, which is amplified by an electronic gain, $G_{\Delta V}$,

$$\Delta V = (V_w - V_s)\, G_{\Delta V} \tag{3-1}$$

As demonstrated below, the difference signal is a nearly direct measure of the strong band integrated extinction. While a simple radiometer measurement can be sufficient to retrieve gas mixing ratios in the lower mesosphere and stratosphere, SOFIE seeks to characterize the tenuous regions extending into the lower thermosphere. At these altitudes, atmospheric densities and gaseous abundances are low and the corresponding signals can be overwhelmed by a variety of measurement errors. However, common mode errors are nearly eliminated in the difference signal measurements. This benefit is realized because a variety of solar, atmospheric, and instrumental effects are nearly equal and positively correlated in the strong and weak bands, and therefore removed by electronically differencing the band pairs. Another benefit is the electronic gain applied to the difference signals, which allows digitization-limited measurements to achieve a precision consistent with the detector noise.

The measured signal for a hypothetical single ray observation (i.e. perfectly resolved spatially) can be written as an integral in wavelength (λ):

$$V = C\int \Gamma(\lambda)\, S(\lambda)\, \tau(\lambda)\, d\lambda \tag{3-2}$$

where $\Gamma(\lambda)$ is the instrument spectral response function, $S(\lambda)$ is the solar source function, $\tau(\lambda)$ is atmospheric transmission, and C is an instrument response constant. We define the band-integrated transmission as

$$\tau = V / V_0 \tag{3-3}$$

For a band pair comprising a SOFIE channel, the measurements are mathematically balanced during data analysis so that the weak and strong exoatmospheric signal are equal, $V_{0,W} = V_{0,S}$. As a result ΔV divided by V_0 yields the transmission difference:

$$\Delta V / V_0 = (V_W - V_S) / V_0 = \tau_W - \tau_S \tag{3-4}$$

For optically thin conditions (3-2) can be approximated by:

$$V = C\int I(\lambda)\, S(\lambda)\, (1-\sigma(\lambda))\, d\lambda \tag{3-5}$$

where $\sigma(\lambda)$ is the limb path optical depth and $\tau(\lambda) = \exp(-\sigma(\lambda)) \approx 1 - \sigma(\lambda)$. From (3-3) $\tau \approx 1 - \sigma$, where over-bars denote a band average. In the absence of clouds $\sigma_W << \sigma_S$, and (3-4) becomes

$$\Delta V / V_0 = \tau_W - \tau_S = \sigma_S - \sigma_W \approx \sigma_S \tag{3-6}$$

In the presence of clouds $\sigma_S = \sigma_{Sg} + \sigma_{Sc}$ and $\sigma_W = \sigma_{Wc}$ where subscripts "g" and "c" refer to gas and cloud components of the optical depth, respectively. It follows that

$$\Delta V / V_0 = \sigma_{Sg} - (\sigma_{Wc} - \sigma_{Sc}) \tag{3-7}$$

As a result, for optically thin conditions and approximately equal PMC extinction in band pairs, the difference signal is nearly proportional to the integrated gas extinction, and therefore a nearly direct measure of the target gas. In practice the signals are fully modeled with detailed monochromatic optical depth calculations along the observation path, then spectrally integrated over the source function and the relative spectral response function. These single ray simulations are performed for various view angles and then integrated over the field-of-view (FOV) and spatial solar source function to rigorously simulate signals during the retrieval process. The above discussion illustrates how the difference signal can dramatically reduce errors in the gas retrieval due to the uncertainty of contaminant ice extinction, while enhancing the dynamic range of the gas measurement.

PMC extinction, defined as optical cross section per unit volume, is retrieved from SOFIE radiometer measurements at 11 wavelengths as summarized in Table 3.6. Figure 3.2 illustrates the position of the 16 SOFIE bands with respect to a typical PMC extinction spectrum. Note that the signal is due entirely to scattering at wavelengths less than ~1.5 μm and to absorption at wavelengths greater than ~2.5 μm. Four bands were designed to target PMCs and the remaining PMC measurements are from the gas channel weak bands. At mesospheric altitudes, the IR gas channel weak band signals are due primarily to PMCs. Thus PMC extinction can be retrieved without knowledge of the interfering gaseous signals. In addition, CH_4 concentrations are extremely small at PMC altitudes, so the strong band signal is dominated by PMCs and can be used to retrieve cloud extinction. The band averaged PMC extinction can be treated as monochromatic (using the band center wavelength) with negligible error.

SOFIE provides difference signal measurements of PMCs from channels 2 and 5. With the optically thin assumption, the PMC difference signal can be written as

$$\Delta V / V_0 = \tau_{Wc}\, \tau_{WI} - \tau_{Sc}\, \tau_{SI} \approx \sigma_{Sc} + \sigma_{SI} - \sigma_{Wc} - \sigma_{WI} \tag{3-8}$$

where the subscript "I" refers to interference. The retrieval of PMC extinction from ΔV requires knowledge of the wavelength dependence of PMC extinction between the weak and strong bands. For channel 2, $\sigma_{Sc} / \sigma_{Wc} = 2.0 \pm 0.05$ and is nearly insensitive to particle size and shape. Both weak and strong band interference in channel 2 is due only to Rayleigh scatter. The band 3 / band 4 Rayleigh optical depth ratio determined according to *Bodhaine et al.* [1999] is 2.056 and invariant in temperature and pressure. Thus, the channel 2 difference signal becomes

$$\Delta V / V_0 = \sigma_{Wc} + 1.056\, \sigma_{WI} \tag{3-9}$$

which is the basis for retrieving PMC extinction from channel 2. For channel 5 σ_{WI} and σ_{SI} are both nearly zero so that

$$\Delta V / V_0 = \sigma_{Sc} - \sigma_{Wc} \tag{3-10}$$

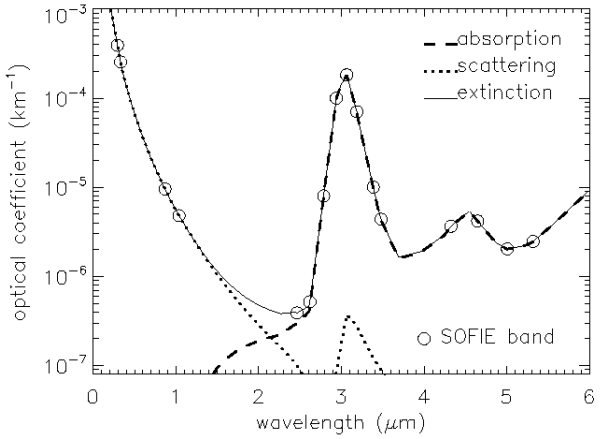

Figure 3.2. PMC scattering, absorption, and extinction spectra modeled using the average PMC size distribution from *von Cossart et al.* [1999]. The position of SOFIE bands is indicated.

3.3. SOFIE Forward Model

The measurement retrievals (i.e. Level 2) determine the geophysical parameters of temperature, gas mixing ratios, and aerosol extinctions from the SOFIE signals. These retrievals rely on the ability to simulate SOFIE measurements. The signal simulations must describe the radiative transfer of sunlight through the limb of the Earth's atmosphere, and then account for instrumental effects. Atmospheric transmissions are simulated using rigorous line-by-line radiative transfer calculations [*Gordley et al*., 1994] with appropriate gaseous line parameters. The radiative transfer calculations assume a spherically symmetric atmosphere.

To account for instrument effects, the simulated transmissions are integrated spatially over the SOFIE FOV response and the measured solar source function, and spectrally over the instrument RSR curve and relative solar spectrum [*Kurucz*, 1995]. The simulated band and source averaged transmissions are then converted to counts based on the measured exoatmospheric signals, and nonlinearity is applied to the simulated V and ΔV signals based on the coefficients in Table 3.6. For the ΔV signals, the weak and strong band signals are modeled as above, and ΔV is determined from the simulated V_W and V_S. Simulated signals are compared to the measurement, and the target gas mixing ratio, Q, is adjusted based on the derivative $\delta\tau/\delta Q$, which considers the previous attempt to match the measurement. Iteration continues at a given altitude until the measured signal is reproduced to within the noise. The retrievals assume an isothermal and evenly mixed upper boundary. This has a minor impact on results due to the extremely weak extinction at altitudes above the start of retrieval. The exceptional fidelity and S/N of the data allows a direct "onion peel" retrieval on the 200 m vertical grid defined in level1 processing. However, operationally each profile is separated into seven individual profiles at 1.4 km spacing which are processed independently. The resulting seven profiles are combined and smoothed with a 0.8 km full width Gaussian to reduce random error, and final retrieval products are reported on the uniform 200 m vertical grid.

3.4. SOFIE Inversion

The following is a description of the methods used in the level 1 and level 2 data processing.

3.4.1. Level 1

Level 1 processing registers all data with absolute times and zenith angles. Ephemeris information is used to determine the SOFIE FOV line of sight position versus time in Earth coordinates. SOFIE detector and sun sensor data are put on a uniform 200 m altitude grid for ease of use.

Solar Limb Darkening Curves. SLDCs are measured using exoatmospheric solar scans as described above. These data are used to generate partial two dimensional maps of solar intensity in sun sensor coordinates sufficient for use in level 2 processing when spatially integrating simulated transmissions over the FOV and solar source.

Auxiliary data. Independent temperature/pressure profiles from National Centers for Environmental Prediction (NCEP) analyses are used in the registration of SOFIE profiles in absolute altitude. For this purpose, data are taken from the NCEP grid point closest to the location and time of a SOFIE measurement. Thermospheric temperatures required in signal simulations above the upper limit of SOFIE temperature retrievals (currently 95 km) are taken from the MSIS 2000 model [*Hedin,* 1991]. MSIS is initialized using current solar flux information from the National Oceanic and Atmospheric Administration.

Signal conditioning. Time offsets due to the multiplexer sampling (from 0 to 37.5 ms) and electronic filtering (0.1 s) are removed from all radiometer and difference signals. Background signals are subtracted from the radiometer signals. Electronic gain is removed from the difference signals through division by the known $G_{\Delta V}$. To simplify their use in level 2 processing, a balance correction is applied to the ΔV, V_W, and V_S signals so that the data is equivalent to an exoatmospheric condition of $\Delta V = 0$ and $V_{W0} = V_{S0}$.

SOFIE signals can change slowly during an event for a variety of reasons, including thermal changes within the CSM optics and FOV movement on the solar image. Signal drift caused by FOV movement is removed explicitly by adjusting V_0 using pointing information from the sun sensor with the measured SLDC. After the pointing effects are removed, residual signal drift remains due to secondary effects such as beam movement across the detectors. The residual drift is typically small and has long time constants. It is removed by a linear fit in time at altitudes well above the atmosphere, and extrapolating the residual into atmospheric measurement time.

Altitude registration. SOFIE has three methods of registering transmission profiles. The current operational method uses NCEP temperature and pressure versus altitude to simulate 4.324 μm CO_2 transmission profiles. The initial SOFIE tangent point altitude profile is determined using orbital ephemeris data and FOV position knowledge. This provides the relative angle between measurements to within ± 0.2 arcsec. Altitude registration is then accomplished by adjusting the absolute position of the SOFIE altitude profile so that the measured and simulated CO_2 transmissions match at altitudes between 35 and 45 km. The second method which is the final operational approach in V1.4, employs an identical procedure, but uses measured refraction angle profiles determined from the sun sensor solar extent measurements. These are compared to a modeled refraction angle profile calculated using the NCEP T and P versus altitude, over 25-35

km. This approach has the distinct advantage of eliminating the need for an assumed (modeled) CO_2 mixing ratio profile.

Refraction angle temperature retrievals. During an occultation event, solar rays are refracted by the Earth's atmosphere towards higher densities (towards Earth). Sun sensor measurements of vertical solar extent (E) are used to determine the atmospheric refraction angle versus altitude. Atmospheric refraction angles (θ) are related to solar extent by

$$\theta_t = \theta_{t-\Delta t} + (E_0 - E_t) \tag{3-11}$$

where subscripts refer to time. θ_t is the refraction angle for a ray emanating from the bottom edge of the solar image. Δt is the time required for the un-refracted elevation angle to change by an angle equal to the un-refracted solar angular extent (E_0), which is measured above the atmosphere. The recursive process begins with measurements above the atmosphere (where $\theta = 0$). Once the refraction angle versus time is known, the tangent point altitude corresponding to the apparent location of the sun (impact altitude, Z_I) can be determined from

$$Z_I = (R_E + Z_{SC}) \cos(\Phi - \theta) - R_E \tag{3-12}$$

where R_E is Earth radius, Z_{SC} is spacecraft altitude, and the declination angle, Φ, is the angle between the spacecraft local horizontal plane and the non-refracted spacecraft-sun vector. Altitude dependence of refraction angle is directly related to the atmospheric density profile. Assuming hydrostatic equilibrium a measured refraction angle profile can therefore be used to retrieve temperature versus pressure [*Ward and Herman*, 1998]. SOFIE determines refraction angles with better than 0.2 arcsec precision, and relative impact altitude spacing to ~ 3 meters. Note that equation 14, to our knowledge, has not been used before. This recursive formulation provides refraction angle profiles that depend only on the knowledge of Δt (which is accurately known from orbital ephemeris) and the observed solar extent as a function of time. As a result, the need for platform attitude knowledge is effectively eliminated. The refraction angle measurement accuracy becomes equivalent to the accuracy to which the change in solar extent can be measured. Because the technique requires only knowledge of the change in E, absolute measurement errors are nearly eliminated. Measured refraction angles are used to retrieve temperatures at altitudes below about 50 km and above tropospheric cloud tops. Polar stratospheric clouds are not expected to affect the refraction angle measurements, although tropospheric clouds are anticipated to be a problem.

3.3.2. Level 2

Level 2 processing retrieves the geophysical parameters of temperature, gas mixing ratios, and aerosol extinctions from the SOFIE signals. These retrievals rely on the ability to simulate SOFIE measurements. The signal simulations must describe the radiative transfer of sunlight through the limb of the Earth's atmosphere, and then account for instrumental effects. Atmospheric transmissions are simulated using rigorous line-by-line radiative transfer calculations [*Gordley et al.*, 1994] with appropriate gaseous line parameters. The radiative transfer calculations assume a spherically symmetric atmosphere.

The simulated transmissions are integrated spatially over the SOFIE FOV response and the measured solar source function, and spectrally over the instrument RSR curve and relative solar spectrum [*Kurucz*, 1995]. The simulated band and source averaged transmissions are then converted to counts based on the measured exoatmospheric signals, and nonlinearity is applied to

the simulated V and ΔV signals based on the coefficients in Table 3.6. For the ΔV signals, the weak and strong band signals are modeled as above, and ΔV is determined from the simulated V_W and V_S. Simulated signals are compared to the measurement, and the target gas mixing ratio, Q, is adjusted based on the derivative $\delta\tau/\delta Q$, which considers the previous attempt to match the measurement. Iteration continues at a given altitude until the measured signal is reproduced to within the noise. The retrievals assume an isothermal and evenly mixed upper boundary. This has a minor impact on results due to the extremely weak extinction at altitudes above the start of retrieval. The exceptional fidelity and S/N of the data allows a direct "onion peel" retrieval on the 200 m vertical grid defined in level 1 processing. However, operationally each profile is separated into seven individual profiles at 1.4 km spacing which are processed independently. The resulting seven profiles are combined and smoothed with a 0.8 km full width Gaussian to reduce random error, and final retrieval products are reported on the uniform 200 m vertical grid.

Temperature/CO_2 Retrievals. SOFIE retrieves temperature/pressure and CO_2 mixing ratios simultaneously using measurements from channels 4 and 7. The approach assumes hydrostatic equilibrium and works from low to high altitude. Because of the high degree of in-orbit inter-calibration of channels required for accurate CO_2 retrievals, CO_2 is not included in the first release of SOFIE data. CO_2 mixing ratios from the WACCM model, which is based on the CAM3 model [*Collins et al.* 2003], are used to retrieve temperature and. Future releases are planned to include retrieved CO_2.

CO_2 absorption in channel 7 is in local thermodynamic equilibrium (LTE) throughout the stratosphere and lower mesosphere but is significantly impacted in the polar summer by non-LTE processes in the upper mesosphere and lower thermosphere. In the upper mesosphere the lower state population of several significant bands are enhanced by absorption of upwelling radiation and in the lower thermosphere the excitation from upwelling radiation and thermal collisions is more than offset by thermal quenching and emission to space. The net effect of non-LTE processes in the polar summer upper mesosphere and lower thermosphere is enhanced absorption below the mesopause and reduced absorption at higher altitudes. Figure 3.3.2 shows a reference temperature profile that was used to simulate a band 13 transmission profile including non-LTE effects, and the temperature profile that is retrieved when assuming LTE. The results indicate that ignoring non-LTE when using band 13 can result in retrieved temperatures that are biased warm by over 10 K near the mesopause and biased cold by over 10 K at higher altitudes. SOFIE retrievals include a complete representation of non-LTE effects.

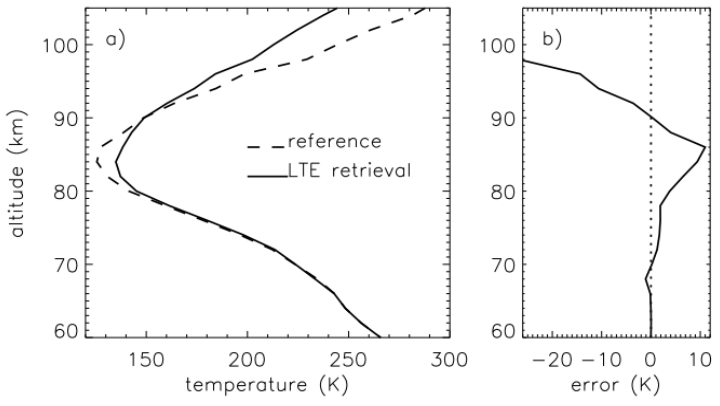

Figure 3.3.2. a) Reference temperature profile used to simulate band 13 transmission versus altitude including non-LTE effects, and the temperature profile that was retrieved from the simulated transmissions when assuming LTE. b) The retrieval error for assuming LTE, as the difference between the retrieved and reference profiles.

Optical Cross Sections. Except for O_3 and molecular (Rayleigh) scattering, all gas molecules are modeled using line parameters from the HITRAN (2006) data base. Rayleigh scattering, an important contribution in bands 1-4, is modeled using the expression of *Bodhaine et al.* [1999], and combined with molecular densities calculated using SOFIE temperature profiles to determine molecular extinction. Ozone transmission is modeled using the HITRAN 2004 cross sections which are based on *Bass and Paur* [1985] and cover temperatures from 200 to 300 K. In band 1, the O_3 cross sections vary (approximately linearly) by less than 10% between 200 and 300 K. Linear extrapolation to summer mesosphere temperatures (150 K) suggests less than 5% changes from the 200 K cross sections. Because the change in cross section is apparently small, and the temperature extrapolation is uncertain, the current algorithm interpolates for temperatures between 200 and 300 K but does not attempt to extrapolate in temperature. In band 2, the O_3 cross sections change by 10 to over 100% from 200 to 300 K, varying with a second or third order dependence on temperature. While temperature dependence is likely a significant effect in band 2, the cross sections are more than two orders of magnitude smaller than band 1, rendering them an insignificant effect on the ozone retrievals. The treatment of low temperature O_3 cross sections will be refined in upcoming SOFIE data versions.

3.5. SOFIE Error Analysis and Corrections

SOFIE uncertainty analysis considers error mechanisms that can be categorized as due either to the SOFIE measurements, or to the signal simulations used in the retrievals. Simulation uncertainties include modeling errors, the representation of instrument characteristics (e.g., relative spectral response (RSR)), and the description of interfering gases and aerosols. The relevant validation papers contain detailed error analysis for the retrieved species (see Section 3.6.2 for details).

3.6. SOFIE Calibration

SOFIE was calibrated in the laboratory under vacuum at the predicted nominal operational temperature (-20°C), and at the predicted cold (-35°C) and hot (5°C) operational temperature limits. Temperature measurements on orbit show mean CSM temperatures of roughly -16°C with variations of about 0.5 to 1°C over the course of an orbit, well within the range of ground calibration temperatures. Radiative calibration sources included a solar emulator blackbody (SEB) which achieved temperatures up to ~3000K. Radiance from the SEB was equivalent to 28 to 46% of the exoatmospheric solar signal in bands 5-16. The SEB provided about 0.1% of the expected exoatmospheric solar signal in bands 1 and 2, and 8% for bands 3 and 4. Bands 1-4 were therefore stimulated with alternate sources including a xenon lamp. The Sun was viewed in the laboratory by directing the solar image into the SOFIE aperture using external pointing mirrors. Atmospheric transmissions on a cloud-free day ranged from zero in bands 1, 6, 7, and 13 to 0.99 in bands 3 and 4. A benefit of the CSM ND filter was realized during calibration because irradiance from the SEB in bands 5-16 without the ND filter was equivalent to full-sun radiance levels expected on-orbit with the ND filter installed, allowing calibration over the full dynamic range. The ground calibration results are described in detail in *Gordley et al.* [2009]. Table 3.6 gives the baseline calibration results. Some sub-sections below contain additional results when the calibrations were updated.

3.6.1. Noise and Background

Radiometer background signals were characterized in the laboratory using measurements with the aperture cover closed. These results show background levels ranging from 11 to 20 counts. In-orbit measurements taken prior to opening the aperture cover show background levels that are nearly identical to the laboratory results. System noise levels for the radiometers (η_V) and difference signals ($\eta_{\Delta V}$) were characterized using measurements with the aperture closed, and while viewing a radiative source. Because the effective bandpass of the data is ~2 Hz, noise is defined as the response standard deviation of the mean determined at 0.5 second intervals from the 20 Hz measurements. For truly random noise that is below the digitization limit, the expected η_V for randomly varying signals is 0.3 counts. The 2 Hz (10 sample average) radiometer noise determined in the laboratory while viewing the SEB is on the order of 0.2 counts, indicating that the true radiometer 2 Hz noise level is below the V measurement digitization limit. On-orbit sun center measurements from over 100 days in 2007 confirm the laboratory results, indicating noise values from 0.13 to 0.2 counts (see Table 3.6). True radiometer signal-to-noise (S/N) values (V/η_V) are therefore in excess of ~1.6×10^5.

While the radiometer measurements (V) do not resolve the detector noise, the noise is resolved by the ΔV measurements because the signals are electronically amplified by a gain ($G_{\Delta V}$) of 30 to 300 prior to digitization. The ΔV S/N, defined as $G_{\Delta V} V_0 / \eta_{\Delta V}$, was also determined from laboratory and in-orbit measurements with the aperture cover closed. The results indicate similar performance pre and post-launch (Table 3.6), with S/N ranging from 2.7×10^5 in channel 8 to over 40×10^5 in channel 2. While this provides an estimate of the system dark noise and confirm that no significant post-launch changes occurred, it does not characterize true performance when fully illuminated. Therefore, the ΔV S/N was assessed using in-orbit exoatmospheric sun center measurements from over 100 days in 2007. These results indicate S/N ranging from 1.9×10^5 in channel 8 to 27×10^5 in channel 2. While slightly lower than the cover-closed measurements, the sun center ΔV S/N values are at or in excess of requirements.

Table 3.6. SOFIE calibration results, from ground lab testing and analysis of on-orbit data.

Chan.	Band / Target[1]	Back-ground[2], Lab / On-orbit (counts)	ΔV S/N[2], Lab / On-orbit (×10[5])	V noise[3], On-orbit (counts)	FOV Width[4] (arcmin) vertical / horizontal	Out-of-Band Energy (%)	Nonlinearity (%) ± uncertainty (%)	Nonlinearity Constant, *K* (10^{-6} counts^{-1}) ±uncertainty (%)
1	1 / O_3 s	15.5 / 16.4	21 / 19	0.14	2.08 / 5.08	1.62	0	0
	2 / O_3 w	12.4 / 13.2		0.18	2.15 / 5.43	0.11	0	0
2	3 / PMC s	15.9 / 15.7	59 / 49	0.13	2.05 / 5.90	2.67	0	0
	4 / PMC w	13.4 / 13.6		0.13	2.04 / 5.90	1.33	0	0
3	5 / H_2O w	17.4 / 17.6	4.2 / 3.6	0.16	1.99 / 4.54	1.14	6.3 ± 0.3	1.79 ± 5.4
	6 / H_2O s	16.3 / 16.6		0.14	2.03 / 5.37	0.91	5.8 ± 0.3	1.56 ± 5.8
4	7 / CO_2 s	17.7 / 17.5	3.9 / 3.9	0.14	2.14 / 5.20	0.26	30.9 ± 0.2	9.58 ± 0.7
	8 / CO_2 w	16.4 / 16.2		0.20	2.10 / 6.17	0.66	29.7 ± 0.4	8.55 ± 1.3
5	9 / PMC s	19.2 / 19.3	3.0 / 2.5	0.19	2.03 / 4.15	0.24	2.9 ± 0.2	0.80 ± 8.2
	10 / PMC w	18.9 / 19.3		0.13	1.88 / 5.76	0.16	6.5 ± 0.2	1.60 ± 4.5
6	11 / CH_4 s	19.2 / 18.5	5.2 / 6.8	0.12	2.32 / 6.04	0.34	6.7 ± 0.2	1.74 ± 3.6
	12 / CH_4 w	18.6 / 18.8		0.13	1.90 / 6.00	0.29	8.0 ± 0.2	2.56 ± 2.8
7	13 / CO_2 s	14.9 / 13.4	6.0 / 6.0	0.15	2.15 / 6.36	0.03	17.7 ± 0.4	5.01 ± 2.2
	14 / CO_2 w	15.6 / 15.2		0.11	2.25 / 6.17	0.23	11.4 ± 0.3	3.15 ± 2.7
8	15 / NO w	11.6 / 11.4	2.7 / 2.7	0.12	2.17 / 5.97	0.17	7.1 ± 0.2	1.93 ± 2.8
	16 / NO s	15.4 / 13.6		0.18	2.14 / 5.26	0.16	7.8 ± 0.2	2.20 ± 2.7

[1]s indicates strongly absorbing band, w denotes weakly absorbing band.

[2]determined from aperture closed measurements

[3]determined from on-orbit sunrise sun center measurements at 145-155 km altitude from May 23 – September 15, 2007

[4]FOV width is the separation between half-power points (FWHM).

3.6.2. Response Linearity

The PC MCT detectors in bands 5-16 exhibit response nonlinearity ranging from 2 to 30% at radiance levels consistent with an exoatmospheric solar view. The response of a nonlinear system (V_M) can be defined as the product of the linear response (V_L) and a nonlinear term (f), $V_M = V_L f(V_M)$. SOFIE nonlinearity was calibrated by stimulating the instrument over its dynamic range with the SEB while cycling a CaF_2 window (transmission $\tau_W \approx 0.93$) through the beam to induce a small signal change of known magnitude. This measurement of window transmission (τ_M) as a function of V_M contains the effects of response nonlinearity and is the basis for

characterizing the nonlinear term. *Hervig et al.* [2007] discuss the calibration of IR detector nonlinearity, and determined that the nonlinear term can be described by

$$f(V_M) = 1 - KV_M \tag{3-13}$$

where K is a constant. This expression produces a linear relationship between τ_M and V_M, over useful measurement ranges, consistent with observed performance during SOFIE calibration. Calibrations using the SEB were completed prior to installation of the CSM ND filter to obtain radiance levels consistent with an in-orbit exoatmospheric solar view and the ND filter installed. An example of the measured CaF_2 window transmission versus response is shown in Figure 3.6.2, where a linear fit to τ_M versus V_M is overlain. Results as in Figure 3.6.2 were used to analytically determine K, as described by *Hervig et al.* [2007]. The calibration results are summarized in Table 3.6, where nonlinearity is defined as $100[1 - f(V_0)]$ (%) using in-orbit measurements of V_0. Calibrations completed with the ND filter installed offered less dynamic range, but confirmed the results in Table 3.6. Because the calibration results describe nonlinearity in terms of the measured response, application of the calibration must account for differences in the balance attenuator setting for a given measurement (G) and in the calibration configuration (G_{cal}).

$$f(V_M) = 1 - K\, V_M\, G_{cal} / G \tag{3-14}$$

In all calibration results presented here G_{cal} was set to 0.83.

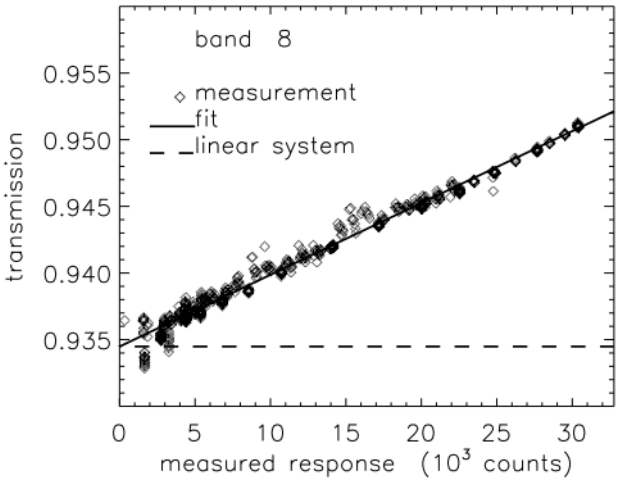

Figure. 3.6.2. Nonlinearity calibration results for band 8. The data were obtained without the flight ND filter installed using the SEB for stimulus. a) Measured filter transmission versus response and a linear fit to these data, consistent with the description of nonlinearity in (10). The transmission measured by an ideal linear system is also shown.

3.6.3. Field of View

The FOV response functions were calibrated using several procedures. The first was by scanning a point source image across the SOFIE FOV using a precise steering mirror. The FOV widths were defined as the distance between half-power points and the boresight center is defined as the integrated centroid. Horizontal (vertical) averages of point source response data were used to determine vertical (horizontal) FOV response functions. FOV functions determined from point source data at cold, nominal, and hot science temperatures indicate no temperature dependence in either the FOV width or position. An example of vertical FOV response derived from the point source measurements is shown in Figure 3.6.3-1a for channel 6 (bands 11 and 12). Figure 3.6.3-1b shows the FOV mismatch for channel 6, determined as the difference of the FOV functions

after they are normalized to equal area. The FOV mismatch is important for interpreting ΔV signals when scanning across spatially abrupt features such as the solar edge or cloud layers. Mismatch is explicitly incorporated in the forward signal simulations during data processing.

The vertical and horizontal FOV dimensions are determined from the point source scan results as the distance between half power points, often known as full width half-maximum (FWHM). The vertical FOV dimensions are shown in Figure 3.6.3-2, and summarized in Table 3.6 for each band. Results for bands 3-16 are from the point source measurements, and from the UV knife edge tests for bands 1-2. The average FOV dimensions for all bands are 2.09 ± 0.11 arcmin in elevation and 5.58 ± 0.62 arcmin in azimuth, which corresponds to 1.60 ± 0.08 km in elevation and 4.28 ± 0.48 km in azimuth at the 83 km tangent point. The point source results were confirmed using knife edge tests where an effective far-field rectangular image of source radiation was scanned vertically and horizontally across the SOFIE FOV using a precision steering mirror. Off-axis rejection characterized by slowly shuttering a far field source revealed insignificant light contamination outside of the FOV dimensions determined from the point source calibrations. All SOFIE FOV response function data files are available on the SOFIE webpage (sofie.gats-inc.com).

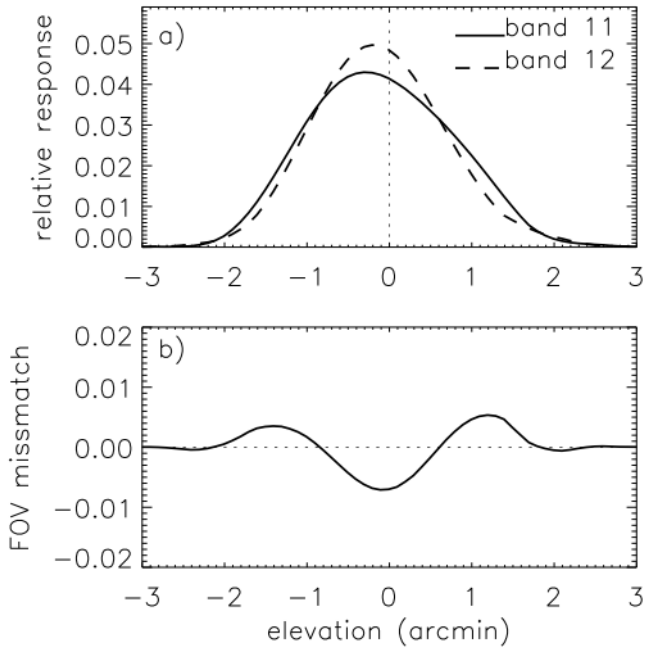

Figure 3.6.3-1. a) Vertical FOV relative response functions for bands 11 and 12 (channel 6). b) The band pair FOV mismatch function, determined as the difference of the FOV response curves.

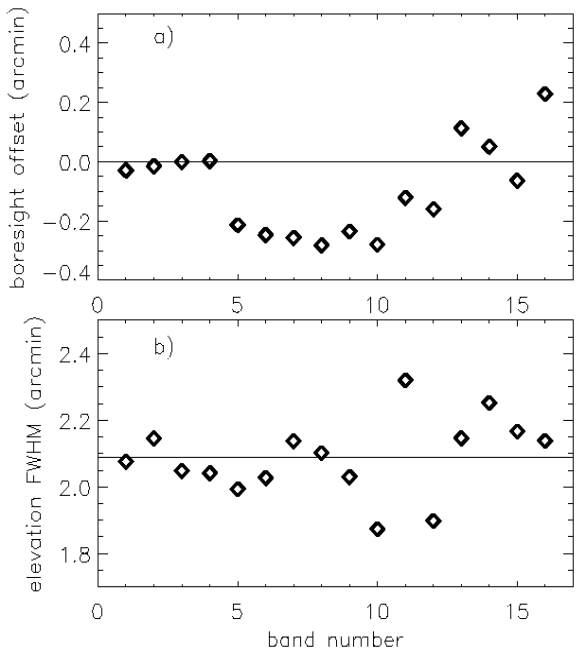

Figure 3.6.3-2. a) FOV elevation boresight location of each band relative to band 3. b) the FOV width (full-width half-maximum) in elevation for each band. The mean for all bands is indicated by a horizontal line.

The FOV boresight positions for each band were determined as the separation relative to the band 3 FOV location. This convention was chosen to provide a simplified calibration of the science FOV - sun sensor boresight, which is also described as relative to the band 3 FOV. FOV boresight positions were determined from the laboratory point source and knife edge scans, based on the FWHM locations (Version 1.1 in Table 3.6.3). Subsequent analysis (Version 1.2) determined the FOV boresight position based on the response weighted centers (i.e., FOV integral 50% points). Note that in the SOFIE results positive angles are towards space (negative towards Earth).

The FOV boresight positions were determined on-orbit using measurements during complete vertical and horizontal scans of the solar disk, conducted well above the atmosphere. These solar scans were conducted with relatively slow slew rates to minimize time lags in the detector response. The analysis showed differences in the FOV boresight locations between sunrise (SR) and sunset (SS). The most recent boresights results (Version 1.4) from the analysis of on-orbit solar scans are given in Table 3.6.3.

Table 3.6.3. SOFIE FOV boresight offsets, relative to band 3 (arcmin).				
Band	**V1.0**	**V1.1**	**V1.4**	
			SS	**SR**
1	-0.03	-0.06	-0.030	-0.007
2	-0.01	-0.04	0.004	0.003
3	0.00	0.00	0.000	0.000
4	0.00	0.00	-0.041	-0.039
5	-0.21	-0.22	-0.420	-0.314
6	-0.25	-0.23	-0.241	-0.142
7	-0.26	-0.25	-0.120	-0.034
8	-0.28	-0.27	-0.067	0.009
9	-0.23	-0.20	-0.281	-0.187
10	-0.28	-0.26	-0.206	-0.102
11	-0.12	-0.15	-0.034	0.007
12	-0.16	-0.15	0.024	0.067
13	0.11	0.10	0.084	0.006
14	0.05	0.04	0.067	0.009
15	-0.06	-0.07	-0.040	-0.042
16	0.23	0.21	0.130	-0.017

3.6.4. Science FOV - Sun Sensor Boresight

The science FOV alignment relative to the sun sensor was determined in the laboratory by directing the solar emulator blackbody (SEB) through the MIC1 collimator and into the SOFIE aperture. The beam was scaned in azimuth and elevation using the MIC1 mirror to find the peak in SOFIE science detector response The MIC1 aperture was then imaged using the FPA with extended integration time. Because the SEB source only weakly illuminated the FPA, the images were spatially decimated by a factor of 8. The SEB image center was located on the FPA images, and taken as the location corresponding to the peak in the band 3 response. These measurements have a fair amount of uncertainty and subsequent on-orbit measurements (described below) are preferred.

Elevation boresight: pixel 632 (-15 arcmin from FPA center)

Azimuth boresight: pixel 528 (+2 arcmin from FPA center)

On-orbit Solar Scan Analysis (known as Version 1.1)

The science FOV alignment relative to the sun sensor is determined in-orbit by scanning the FOV over the solar image in azimuth and elevation, while viewing above the atmosphere. Noting the solar image location on the sun sensor FPA when the band 3 measurement response peaks, or reaches an edge, establishes alignment of the FOV and sun sensor. The image center location is determined by the onboard solar tracking algorithm, and verified through analysis on the ground. The relative alignment was found to be consistent with results from ground calibration, and appears to be stable. Note that the analysis did not account for the 0.1 second delay in the detector data due to the electronic filter. Also, there is also an issue with how the azimuth edges are determined that could lead to erroneous azimuth edge location values when there is significant slew in the azimuth direction. The right azimuth edge is determined 0.01 seconds before the left azimuth edge, and then another 0.04 seconds elapses before the right azimuth edge is determine again. This problem could be contributing to the difference in azimuth location here as compared to the laboratory result.

Elevation boresight: pixel 636.16

Azimuth boresight: pixel 501.75

On-orbit Cruiciform Solar Scan Analysis (Version 1.4):

Solar scans are performed on-orbit with each event to characterize the spatial dependence of solar intensity. The solar disc is scanned (while above the atmosphere) from the bottom to the nominal FOV location (boresight) and then over a 1 arcmin box encompassing the boresight location, known as the cruciform. The cruciform scans were used in analysis as described above to determine the science - sun sensor boresight location. A statistically averaged FOV boresight was then determined as the average for thousands of events. The analysis that the boresight location is difference between SR and SS, in elevation but not in azimuth. These calibration results are used in the latest (V1.3) SOFIE processing.

SS Elevation boresight: pixel 639.5997

SS Azimuth boresight: pixel 518.4688

SR Elevation boresight: pixel 638.4785

SR Azimuth boresight: pixel 518.4688

3.6.5. Sun Sensor Tracking Performance

Solar tracking performance was tested in the laboratory by monitoring the solar image directed into the SOFIE aperture using external tracking mirrors. Tracking precision, defined as the 2 Hz standard deviation of mean solar position averaged over 0.5 seconds, was determined to be 0.70 arcsec in elevation and 0.54 arcsec in azimuth. Due to scintillation effects in the lower atmosphere during ground testing, this performance was expected to improve in-orbit. The in-orbit precision has now been verified to be less than 0.2 arcsec in azimuth and elevation.

3.6.6. Spectral Response

End-to-end relative spectral response (RSR) was characterized using a step-scan Fourier Transform Spectrometer. The output beam from the interferometer was observed by SOFIE,

making the SOFIE output the RSR interferograms. Because this beam did not fill the SOFIE aperture, multiple measurements were performed at slightly different input positions with negligible change in RSR results. RSR curves for bands 1-16 at nominal temperature are shown in Figure 3.6.6-1. Calibration included the in-band and out-of-band RSR at -35, -20, and 5°C. The temperature dependence in bandpass position and width (full width half maximum, FWHM) are shown in Figure 3.6.6-2 as the measured change per °C. The changes in band center and FWHM are generally smaller than about 0.1 cm^{-1} $°C^{-1}$. The exception is band 1 where the center and FWHM change by about 1 cm^{-1} $°C^{-1}$. However, the band center shift and FWHM change are only about 0.08% of the 1332 cm^{-1} band width. In bands 2-16, the band center shift is less than 0.01% of the FWHM and the FWHM change is less than 0.05% of the FWHM. Temperature dependence in SOFIE RSR is handled in the foreword model by capturing the temperature dependence of the upper and lower half power points and adjusting the RSR position and width accordingly. Out-of-band (OOB) spectral response was characterized over the wavelength limits of the detector response. The total energy contribution (I_T) was determined by integrating the solar spectrum [*Kurucz*, 1995] over the complete RSR curve (in-band and OOB). The relative in-band energy (I_B) was determined for wavelengths within ± 1.5 FWHM of band center. The relative OOB energy, defined as $100(I_T - I_B)/I_B$ (%), is less than 3% in all cases (Table 3.6). The OOB portion of the RSR is included in the forward model spectral integrals when needed, as determined from simulations.

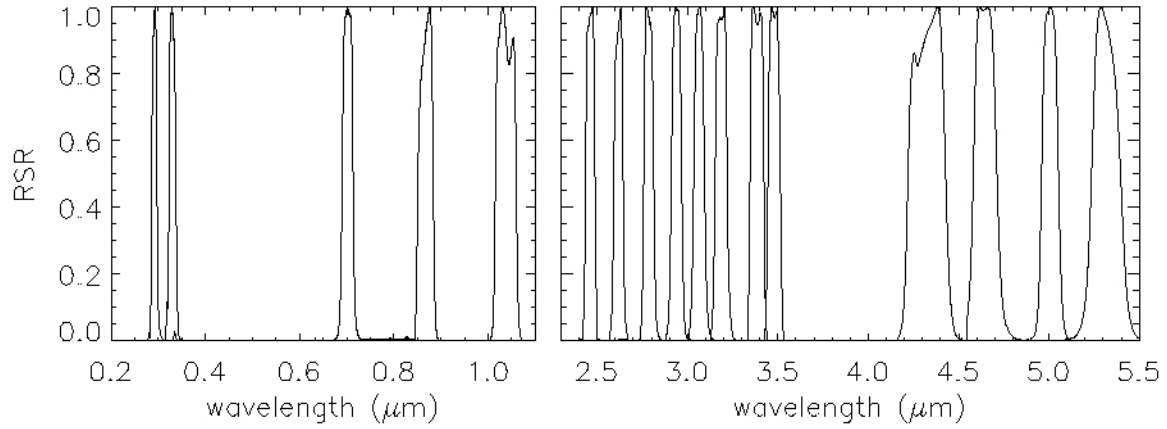

Figure 3.6.6-1. Relative spectral response for bands 1-16 measured at -20°C. A curve for the sun sensor (0.7 μm) based on a combination of the individual component RSRs is also shown.

The sun sensor RSR was derived using component-level measurements of the flight spare ND filter and bandpass filter, and manufacturer measurements of the FPA RSR. The primary sun sensor function of solar tracking does not require stringent RSR calibration. Secondary functions including stratospheric O_3 retrievals do require RSR knowledge.

All SOFIE RSR data files are available on the SOFIE webpage (sofie.gats-inc.com).

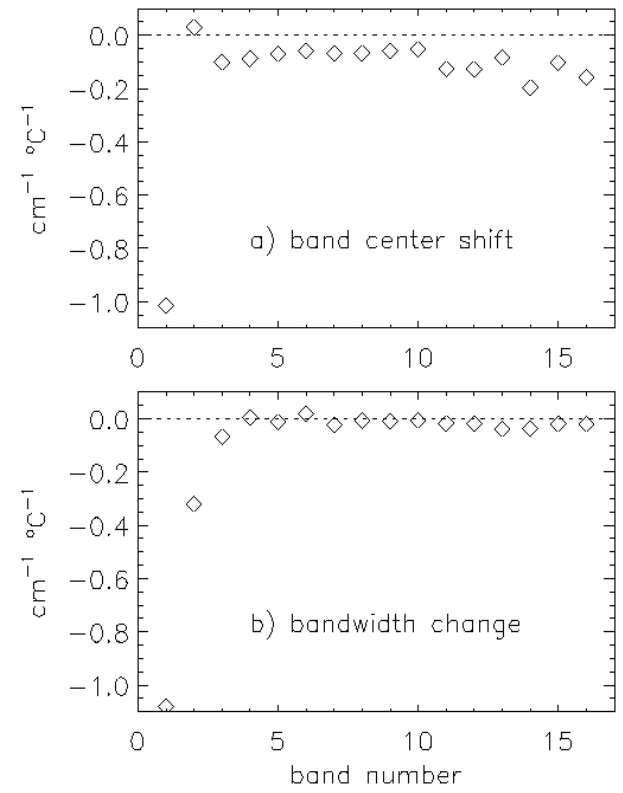

Figure 3.6.6-2. Temperature sensitivity of a) band center location and b) bandwidth, shown as the change per °C for bands 1-16.

3.6.7. Time Response

The time response of the radiometer signals was determined from component modeling, and validated by inducing a rapid signal change. This was accomplished by illuminating the aperture and either rapidly moving the incoming beam or quickly shuttering the beam. The time response for each band was as expected, within the test uncertainty.

3.6.8. Difference Signal Gain

Knowledge of the ΔV gain ($G_{\Delta V}$) is important because its uncertainty directly impacts the atmospheric absorption determined using the difference signal measurements. Because $G_{\Delta V}$ is a direct product of the electronics configuration, the initial values are by design (Table 3.6.8). $G_{\Delta V}$ was subsequently determined in the laboratory by changing the weak band attenuator, G_W, between two settings while viewing the SEB. This induces changes in V_W (δV_W) and ΔV ($\delta \Delta V$) that are used to determine the value of $G_{\Delta V}$:

$$G_{\Delta V} = \delta \Delta V \,/\, \delta V_W \tag{3-15}$$

Because V_W , V_S and ΔV are all measured with the same ADC for a given channel, results are identical if V_S is used. This ground results were also verified in-orbit, using a solar view above the atmosphere, with less than 1% uncertainty (V1.2 in Table 3.6.8).

Table 3.6.8. SOFIE difference signal gain calibration results.			
Channel	**$G_{\Delta V}$ Version 1.0 (By Design)**	**$G_{\Delta V}$ Version 1.1 (Lab Results)**	**$G_{\Delta V}$ Version 1.2 (On-orbit Results)**
1	30	30.0	29.80
2	300	302.8	297.33
3	96	96.7	96.29
4	110	109.8	110.39
5	120	120.1	121.08
6	202	202.8	202.66
7	110	110.6	109.65
8	300	299.9	296.84

3.6.9. Solar Source Function

Solar scans are performed on-orbit with each event to characterize the spatial dependence of solar intensity, known as the solar limb darkening curve (SLDC), in each bandpass. The SLDCs are used in data processing to correct signal changes resulting from unwanted movement of the FOV, and to account for changes in the solar source due to refraction of the solar image observed at tangent altitudes below about 50 km. Because solar intensity decreases away from sun center, FOV drift will result in a decrease in measured intensity that would be falsely attributed to the atmosphere if not modeled. The signal model includes integration of the FOV over the SLDC.

To characterize the SLDC for each event, the solar disc is scanned (while above the atmosphere) from the bottom to the nominal FOV location and then over a 1 arcmin box encompassing that location. Because spacecraft pointing stability is typically better than 5 arcsec during an occultation, FOV movements are small compared to the FOV dimensions. The measured source function is therefore smooth on the scale of the pointing movement, making the correction for pointing-induced signals very accurate.

3.7. SOFIE Validation

SOFIE science data products have been extensively validated in the peer reviewed literature. Validation of SOFIE temperature measurements indicates agreement with independent observations to within reported systematic uncertainties [*Stevens et al.,* 2012; *Sheese et al.*, 2012; *Garcia-Comas et al*., 2014; *Hervig et al.*, 2016]. Comparisons with other observations show agreement to within mutual uncertainties for H_2O [*Rong et al.*, 2010; *Tschanz et al.*, 2013; *Khosrawi et al.,* 2018], O_3 [*Smith et al.*, 2013; *Das et al.*, 2022], CH_4 [*Laeng et al*., 2014; *Rong et al.*, 2016], and NO [*Gómez-Ramírez et al.,* 2013; *Hervig et al.*, 2019]. SOFIE PMC results are a standard in the community, and comparisons show that SOFIE is consistent with ground based lidar [*Hervig et al.*, 2009a; *Hervig et al.*, 2016], radar [*Hervig et al.*, 2010; *Kirkwood et al.*, 2010; *Li et al.*, 2010], and other satellite measurements [*Bailey et al.*, 2015; *Hervig and Stevens*, 2014; *Garcia-Comas et al*., 2016; *Hervig et al.*, 2016]. See also Table 3-1 for more detail.

3.8. SOFIE References

Bailey, S. M., G. E. Thomas, M. E. Hervig, J. D. Lumpe, C. E. Randall, J. N. Carstens, B. Thurairajah, D. W. Rusch, J. M. Russell III, L. L. Gordley (2015), Comparing Nadir and Limb Observations of Polar Mesospheric Clouds: The Effect of the Assumed Particle Size Distribution, *J. Atmos. Solar-Terr. Phys.*, doi:10.1016/j.jastp.2015.02.007.

Bass, A. M., and R. J. Paur, The ultraviolet cross-sections of ozone: II results and temperature dependence, *Atmospheric ozone*, Dordrecht: *Reidel*, p. 611, 1985.

Bodhaine, B. A., N. B. Wood, E. G. Dutton, and J. R. Slusser, "On Rayleigh Optical Depth Calculations", *J. Atmos. Ocean. Tech.*, *16*, 1854-1861, 1999.

Collins, W. D., P. J. Rasch, B. A. Boville, J. J. Hack, J. M. McCaa, D. L. Williamson, B. Briegleb, C. M. Bitz, S. -J. Lin, and M. Zhang, The formulation and atmospheric simulation of the Community Atmosphere Model: CAM3, *J. Climate*, in press, 2006.

Das, S., Bailey, S. M., Thurairajah, B., Hervig, M., Marshall, B. T., and Russell J. M. III (2022), SMLT Ozone from SOFIE and Other Instruments – Validation and Seasonal Climatology, in prep.

García-Comas, M., López-Puertas, M., Funke, B., Jurado-Navarro, Á. A., Gardini, A., Stiller, G. P., Clarmann, T. v., and Höpfner, M., (2016), Measurements of Global Distributions of Polar Mesospheric Clouds during 2005–2012 by MIPAS/Envisat, Atmos. Chem. Phys. Discuss., doi:10.5194/acp-2016-116.

Garcia-Comas et al., (2014), MIPAS temperature from the stratosphere to the lower thermosphere: Comparison of vM21 with ACE-FTS, MLS, OSIRIS, SABER, SOFIE and lidar measurements, *Atmos. Meas. Tech., 7*, 3633–3651, doi:10.5194/amtd-7-6651-2014.

Gomez-Ramirez, D., J. W. C. McNabb, J. M. Russell III, M. E. Hervig, L. E. Deaver, G. Paxton, and P. F. Bernath (2013), Empirical correction of thermal responses in the SOFIE nitric oxide measurements and initial data validation results, *Appl. Optics*, 52, 2950–2959.

Gordley, L. L., M. Hervig, C. Fish, J. M. Russell III, S. Bailey, J. Cook, S. Hansen, A. Shumway, G. Paxton, L. Deaver, T. Marshall, J. Burton, B. Magill, C. Brown, E. Thompson, and J. Kemp (2009), The Solar Occultation For Ice Experiment (SOFIE), *J. Atmos. Solar-Terr. Phys.*, *71*, 300-315, doi:10.1016/j.jastp.2008.07.012.

Gordley, L.L., J. Burton, B. T. Marshall, M. McHugh, L. Deaver, J. Nelsen, J. M. Russell, and S. Bailey (2009), High precision refraction measurements by solar imaging during occultation: results from SOFIE, *Applied Optics*, *48*, 4814-4825, doi:10.1364/AO.48.004814.

Hedin, A. E., Extension of the MSIS thermosphere model into the middle and lower atmosphere, *J. Geophys. Res.*, *96*, 1159, 1991.

Hervig, M., L. Gordley, M. McHugh, E. Thompson, B. Magill, and L. Deaver (2007), On-orbit calibration of HALOE detector linearity, *Appl. Opt., 46*, 7811-7816.

Hervig, M.E., L.L. Gordley, M. Stevens, J.M. Russell, S. Bailey, and G. Baumgarten (2009), Interpretation of SOFIE PMC measurements: Cloud identification and derivation of mass density, particle shape, and particle size, *J. Atmos. Solar-Terr. Phys.*, *71*, 316-330, doi:10.1016/j.jastp.2008.07.009.

Hervig, M.E., L.L. Gordley, J.M. Russell, and S. Bailey, SOFIE PMC measurements during the northern summer of 2007 (2009), *J. Atmos. Solar-Terr. Phys.*, *71*, 331-339, doi:10.1016/j.jastp.2008.08.010.

Hervig, M. E., M. H. Stevens, L. L. Gordley, L. E. Deaver, J. M. Russell, and S. Bailey (2009), Relationships between PMCs, temperature and water vapor from SOFIE observations, *J.*

Geophys. Res., 114, D20203, doi:10.1029/2009JD012302.

Hervig, M. E., L. L. Gordley, L. E. Deaver, D. E. Siskind, M. H. Stevens, J. M. Russell III, S. M. Bailey, L. Megner, and C. G. Bardeen (2009), First satellite observations of meteoric smoke in the middle atmosphere, *Geophys. Res. Letters*, doi:10.1029/2009GL039737.

Hervig, M. E., M. Rapp, R. Latteck, and L. L. Gordley (2010), Observations of mesospheric ice particles from the ALWIN radar and SOFIE, *J. Atmos. Solar-Terr. Phys.*, doi:10.1016/j.jastp.2010.08.002.

Hervig, M. E., and L. L. Gordley (2010), The temperature, shape, and phase of mesospheric ice from SOFIE observations, *J. Geophys. Res.*, 115, D15208, doi:10.1029/2010JD013918.

Hervig, M. E., L. E. Deaver, C. G. Bardeen, J. M. Russell, S. M. Bailey, and L. L. Gordley (2012), The content and composition of meteoric smoke in mesospheric ice particles from SOFIE observations, J. *Atmos. Solar-Terr. Phys.*, doi:10.1016/j.jastp.2012.04.005.

Hervig, M. E., D. E. Siskind, M. H. Stevens, and L. E. Deaver (2013), Inter-hemispheric comparison of PMCs and their environment from SOFIE observations, *J. Atmos. Solar-Terr. Phys.*, doi: 10.1016/j.jastp.2012.10.013.

Hervig, M. E., and M. H. Stevens (2014), Interpreting the 35-year SBUV PMC record with SOFIE observations, *J. Geophys. Res.*, doi:10.1002/2014JD021923.

Hervig, M. E., D. E. Siskind, S. M. Bailey, J. M. Russell III (2015), The influence of PMCs on water vapor and drivers behind PMC variability from SOFIE observations, *J. Atmos. Solar-Terr. Phys.*, doi:10.1016/j.jastp.2015.07.010.

Hervig, M. E., U. Berger, and D. E. Siskind (2016), Decadal variability in PMCs and implications for changing temperature and water vapor in the upper mesosphere, *J. Geophys. Res. Atmos., 121*, doi:10.1002/2015JD024439.

Hervig, M. E., M. Gerding, M. H. Stevens, R. Stockwell, S. M. Bailey, J. M. Russell, G. Stober (2016), Mid-latitude mesospheric clouds and their environment from SOFIE observations, *J. Atmos. Solar-Terr. Phys.*, doi:10.1016/j.jastp.2016.09.004.

Hervig, M. E., Brooke, J. S. A., Feng, W., Bardeen, C. G., Plane, J. M. C. (2017), Constraints on meteoric smoke composition and meteoric influx using SOFIE observations with models, *J. Geophys. Res. Atmospheres, 122*, doi:10.1002/2017JD027657.

Hervig, M. E., C. G. Bardeen, D. E. Siskind, M. J. Mills, R. Stockwell, (2017), Meteoric smoke and H_2SO_4 aerosols in the upper stratosphere and mesosphere, *Geophys. Res. Letters, 44*, doi:10.1002/2016GL072049.

Hervig, M. E., Siskind, D. E., Bailey, S. M., Merkel, A. W., DeLand, M. T., & Russell, J. M., III (2019), The missing solar cycle response of the polar summer mesosphere. *Geophysical Research Letters, 46*. https://doi.org/ 10.1029/2019GL083485.

Hervig, M. E., B. T. Marshall, S. M. Bailey, D. E. Siskind, J. M. Rusell III, C. Bardeen, K. A. Walker, and B. Funke (2019), Validation of SOFIE nitric oxide measurements, *Atmos. Meas. Tech. Discuss.*, https://doi.org/10.5194/amt-2019-56.

Hervig, M. E., Plane, J. M. C., Siskind, D. E., Feng, W., Bardeen, C. G., & Bailey, S. M. (2021). New global meteoric smoke observations from SOFIE: Insight regarding chemical composition, meteoric influx, and hemispheric asymmetry. *Journal of Geophysical Research: Atmospheres, 126*, e2021JD035007. https://doi. org/10.1029/2021JD035007.

Hervig, M. E., D. Malaspina, V. Sterken, L. B. Wilson III, S. Hunziker, S. M. Bailey (2022), Decadal and annual variations in meteoric flux from Ulysses, Wind, and SOFIE observations, *J. Geophys. Res. Space Physics,* in review.

Khosrawi, F, et al. (2018), The SPARC water vapour assessment II: Comparison of stratospheric and lower mesospheric water vapour time series observed from satellites, *Atmos. Meas. Tech. Discuss.*, in review, doi.org/10.5194/amt-2018-33.

Kirkwood, S., M. Hervig, E. Belova, and A. Osepian (2010), Quantitative Relation between PMSE and Ice Mass Density, *Ann. Geophys.*, *28*, 1333-1343, doi:10.5194/angeo-28-1333-2010.

Kurucz, R. L., "The solar spectrum: atlases and line identifications, Laboratory and Astronomical High Resolution Spectra," in Proceedings of *Astron. Soc. of the Pacific Conf. Series 81*, A.J. Sauval, R. Blomme, and N. Grevesse, eds., pp. 17-31, 1995.

Li, Q., M. Rapp, J. Rottger, R. Latteck, M. Zecha, I. Strelnikova, G. Baumgarten, Mark Hervig, C. Hall, and M. Tsutsumi (2010), Microphysical parameters of mesospheric ice clouds derived from calibrated observations of polar mesosphere summer echoes at Bragg wavelengths of 2.8 m and 30 cm, *J. Geophys. Res., 115*, D00113, doi:10.1029/2009JD012271.

Laeng, A., J. Plieninger, T. von Clarmann, U. Grabowski, G. Stiller, N. Glatthor, F. Haenel, S. Kellmann, M. Kiefer, A. Linden, S. Lossow, L. Deaver, A. Engel, M. Hervig, I. Levin, M. McHugh, S. Noel, G. Toon, K. Walker (2015), Validation of MIPAS IMK/IAA methane version V5R_CH4_222 profiles, *Remote Sensing of Environment*, doi:10.5194/amtd-8-5565-2015.

Marshall, B. T., L. E. Deaver, R. E. Thompson, L. L. Gordley, M. J. McHugh, M. E. Hervig, and J. M. Russell III (2011), Retrieval of temperature and pressure using broadband solar occultation: SOFIE approach and results, *Atmos. Meas. Tech. Discuss.*, *3*, 5743-5794, doi:10.5194/amtd-3-5743-2010.

Rong, P., J. M. Russell III, B. T. Marshall, D. E. Siskind, M. E. Hervig, L. L. Gordley, P. F. Bernath, and K. A. Walker (2016), Version 1.3 AIM SOFIE measured methane (CH_4): Validation and Climatology, *J. Geophys. Res. Atmos., 121*, doi:10.1002/2016JD025415.

Rong, P., J. M. Russell III, L. L. Gordley, M. E. Hervig, L. Deaver, D. Siskind, P. F. Bernath, and K. A. Walker (2010), Validation of v1.022 mesospheric water vapor observed by the SOFIE instrument onboard the AIM satellite, *J. Geophys. Res.*, 115, D24314, doi:10.1029/2010JD014269.

Russell, J. M. III, L. L. Gordley, J. H. Park, S. R. Drayson, W. D. Hesketh, R. J. Cicerone, A. F. Tuck, J. E. Frederick, J. E. Harries, and P. J. Crutzen (1993), The Halogen Occultation Experiment, *J. Geophys. Res*., *98*, 10,777-10,797.

Sheese, P. E., Strong,K., Llewellyn, E. J., Gattinger, R. L., Russell III, J. M., Boone, C. D., Hervig, M. E., Sica, R. J., and Bandoro, J. (2012), Validation of OSIRIS mesospheric temperatures using satellite and ground-based measurements, *Atmos. Meas. Tech. Discuss.*, 5, 5493-5526, doi:10.5194/amtd-5-5493-2012.

Smith, A. K., V. L. Harvey, M. G. Mlynczak, B. Funke, M. Garcia-Comas, M. Hervig, M. Kaufmann, E. Kyrola, M. Lopez-Puertas, I., McDade, C. E. Randall, J. M. Russell III, P. E. Sheese, M. Shiotani, W. R. Skinner, M. Suzuki, K. A. Walker, (2013), Satellite observations of ozone in the upper atmosphere, *J. Geophys. Res.*, 118*,* 5803–5821*, doi:10.1002/jgrd.50445.*

Stevens, M. H., L. E. Deaver, M. E. Hervig, J. M. Russell III, D. E. Siskind,P. E. Sheese, E. J. Llewellyn, R. L. Gattinger, J. Höffner, B. T. Marshall (2012), Validation of Upper Mesospheric and Lower Thermospheric Temperatures Measured by the Solar Occultation For Ice Experiment, *J. Geophys. Res*., *117*, D16304, doi:10.1029/2012JD017689.

Tschanz, B., Straub, C., Scheiben, D., Walker, K. A., Stiller, G. P., and Kämpfer, N. (2013): Validation of middle-atmospheric campaign-based water vapour measured by the ground-

based microwave radiometer MIAWARA-C, *Atmos. Meas. Tech.*, 6, 1725-1745, doi:10.5194/amt-6-1725-2013.

Ward, D. M. and Herman, B. M. (1998), Refractive sounding by use of satellite solar occultation measurements including an assessment of its usefulness to the stratospheric aerosol and gas experiment program, *Appl. Optics, 37*, 8306–8317.

4. The Cosmic Dust Experiment (CDE)

4.1. CDE Overview

A number of techniques have been used to measure the cosmic dust influx into our atmosphere, including high-powered large- array (HPLA) radars [*Mathews et al.*, 2001; *Janches and ReVelle*, 2005; *Sparks and Janches*, 2009], optical observations [*Ho ̈rz et al.*, 1975; *Leinert*, 1975] and in situ dust detectors [*Love and Brownlee*, 1993; *Tuzzolino et al.*, 2001a; *Schwanenthal*, 2004]. HPLA radar offers a unique window on micron-sized dust flux measurements by analyzing the meteor head echoes generated by dust particles undergoing ablation in Earth's upper atmosphere. Recent work has attempted to refine the physical description of ablating particles and their detection via radar [*Fentzke and Janches*, 2008], yet such measurements are by nature limited to observations at specific terrestrial latitudes. In situ dust detectors, such as the Long Duration Exposure Facility (LDEF) [*Love and Brownlee*, 1993] and the Space Dust (SPADUS) instrument aboard the ARGOS spacecraft [*Tuzzolino et al*., 2001a], have measured the terrestrial cosmic dust influx; however, significant uncertainty remains in the spatial and size distributions and variability thereof. The estimates for the flux of particles o 10 mm in radius show disagreement on an order of magnitude, highlighting the difficulties of measuring the sub-millimeter dust flux.

Dust grains with radii on the order of 100 μm dominate the mass influx of cosmic material into the terrestrial atmosphere. These grains ablate to sub-nanometer-sized particles at an altitude of approximately 80–90 km, and re-condense to nanometer-sized smoke particles [*Hunten et al.*, 1980; *Kalashnikova et al.*, 2000; *Rapp*, 2009]. The presence of these particles has been identified as a factor in various middle atmospheric phenomena, including PMC [*Turco et al.*, 1982; *Rapp and Thomas*, 2006], Polar Mesosphere Summer Echoes (PMSE) [*Cho and Kelley*, 1993; *Cho and Rottger*, 1997; *Rapp and Lubken*, 2001; *Lubken and Rapp*, 2001] and the formation of metallic layers [*Plane*, 2003]. Ablation products from micrometeorites can also play a role in stratospheric physics [*Turco et al*., 1981; *Murphy et al*., 1998; *Cziczo et al.*, 2001]. Cosmic dust particles are a leading candidate for the creation of condensation nuclei (CN) for PMC and are believed to be responsible for creating electron bite-outs in the local plasma density, leading to PMSE. Models have shown that the eventual distribution of smoke particles in the mesosphere is highly sensitive to the amount and variability of the cosmic dust influx [*Megner et al.*, 2008; *Bardeen et al*., 2008], which were verified by AIM/SOFIE observations of meteoric smoke [*Hervig et al.*, 2009]. An accurate, temporally and spatially resolved measurement of the terrestrial cosmic dust input is important in determining the role and extent of cosmic dust forcing on mesospheric phenomena.

4.1.1. CDE Heritage

CDE is nearly identical to the Student Dust Counter (SDC) onboard the New Horizons mission to Pluto [*Horányi*, 2008; *Poppe et al*., 2010] and PVDF detectors have been previously flown on several spacecraft, including the Cassini mission to Saturn [*Srama et al*., 2004], the ARGOS mission around Earth [*Tuzzolino et al.*, 2001a] and the STARDUST mission to comet 81P/Wild [*Tuzzolino et al.*, 2004].

4.1.2. CDE Product Description

Level 1 data consists of time of impact, pulse-height, and engineering & housekeeping data.

Level 2 data consists of time of impact, and the derived mass[g] of the detected dust particle.

Level 3 data describe total meteoric mass per orbit, and impact rates per mass bin.

Level 4 data contain meteoroid influx (# y^{-1} m^{-2}), as monthly means in each hemisphere.

4.2. CDE Theoretical Description

CDE consists of 14, 28 μm thick PVDF detectors coated with 100 nm of aluminum–nickel and mounted to an external panel facing the zenith direction. Twelve of the detectors are exposed to space (referred to as the 'science' detectors), while two detectors are covered by aluminum cases and mounted to the underside of the instrument panel in order to detect background signals ('reference' detectors). When a dust particle impacts a detector, the AlNi layer is punctured and a crater is formed in the polarized PVDF, generating a fringing electric field around the crater [*Poppe et al.*, 2010]. This fringing electric field causes a change in the charge density on the AlNi plate, which is measured by an accompanying electronics box mounted to the inside of the AIM spacecraft. The total number of electrons, N, generated by an impacting dust particle was empirically fit based on experimental calibration data [*Simpson and Tuzzolino*, 1985; *Tuzzolino*, 1992; *James et al.*, 2010] and is given by:

$$N = (1.2\text{x}10^{15} + 6.7\text{x}10^{12}\ T)\ v^{2.88}\ m^{1.052} \quad (4\text{-}1)$$

where v [km/s] is the impactor speed, m [g] is the impactor mass and T [°C] is the detector temperature. Since the charge is dependent on both the particle mass and velocity, it is assumed that the incoming particles are on radial trajectories with velocities equal to the Earth escape velocity. While previous work has shown that micrometeorites can enter the Earth's atmosphere at speeds significantly higher than the terrestrial escape velocity at 80–140 km [*Janches et al.*, 2003, 2006; *Sulzer*, 2004; *Janches and Chau*, 2005], we follow previous work and assume the terrestrial escape velocity at CDE's orbit (600 km) [*Hunten et al.*, 1980; *Love and Brownlee*, 1991; *Kalashnikova et al*., 2000]. The escape velocity is vectorially added to the spacecraft velocity to calculate the dust impact speed. While space debris is present in the near-Earth environment, such particles would not significantly contribute to the CDE dataset. This is due to the fact that orbital debris are mainly circular orbits and therefore, would strike CDE at approximately 90° [*Tuzzolino et al.*, 2001a, 2001b], outside CDE's sensitive range of impact angles of <45° [Horányi, 2008].

Using equation (4-1), the measured impact amplitude and the calculated impact velocity are used to determine the grain mass. CDE has a 1-s time resolution, a total surface area of 0.11 m^2 and can resolve dust grain masses within a factor of two for mass, $10^{-11} < m < 5\text{x}10^{-9}$ g. CDE cannot resolve particle mass for grains with $m > 5\text{x}10^{-9}$ g, yet still records an impact for these grains. The measured grain masses are converted into grain radii by assuming a spherical grain shape and a density of 2500 kg m^{-3} [*Jessberger et al*., 2001].

PVDF sensors are known to be susceptible to generating spurious signals, due to their piezo- and pyroelectric properties [*Nalwa*, 1995]. For this reason, as in the case of SDC, we use the two underside-mounted detectors as noise-monitoring channels. The measured event rate on the science detectors is due to dust impacts and noise, while the rate on the reference detectors is due to noise only. The final dust flux is calculated by subtracting the reference event rate from the science event rate and normalizing by observation time and instrument area.

4.3. CDE Forward Model / Retrieval Algorithms

In order to obtain the cosmic dust flux signal out of the raw CDE data, an adhoc yet rigorous algorithm was developed to recognize noise and remove it from the data. The noise reduction algorithm for CDE consists of two main parts, referred to as 1st Order (O1) and 2nd Order (O2). The O1 algorithm applies a series of four basic filters to the data to remove the most obvious noise events.

1. Temporal coincidence: the temporal coincidence filter removes any events occurring simultaneously ($\Delta t < 1s$) across one or multiple channels. The anticipated dust flux is low enough that the probability of two dust particles impacting simultaneously is negligible and therefore, any two coincident events are assumed to be noise.

2. Spatial coincidence: the spatial coincidence filter removes any events that occur within 0.25° of another hit on consecutive orbits. This filter was motivated by the unique nature of noise lines seen in the CDE data, which appear consistently in latitude over long periods of time and the low probability that two dust impacts on sequential orbits would be at the same point in SZ

3. Northern hemisphere filter: the northern hemisphere filter removes all events generated during the northern hemisphere portion of the orbit contaminated by the noise discussed in Section 4.5. The amount of noise in this period ($-10° < \alpha < +60°$) is so great that the data cannot be reduced.

4. Mask filter: the mask filter removes anomalous periods of data corresponding to easily recognizable instrument artifacts, such as internal CDE calibrations and special experiments conducted by the CIPS instrument which disrupt CDE measurements.

Events removed by the O1 filters listed above are collectively termed coincident events, while all events remaining are called candidate hits. Figure 4-1 shows all events for channel 8 for 50 days, while Figure 4-2 shows the candidate hits for the same channel during the same period.

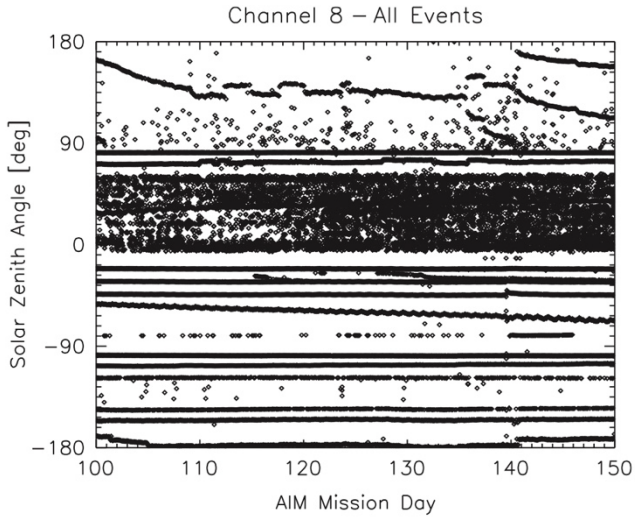

Figure 4-1. Time versus solar zenith angle for all events on channel 8 for 50 consecutive days.

The 2nd Order noise algorithm for CDE is of a finer nature than the 1st Order. Upon investigation of the candidate hits, lines were still visually identifiable (see Figure 4-2, $\alpha \sim -120°$), implying that the O1 filters were not thoroughly removing the line noise. Thus, the main goal of

the O2 reduction code is to remove noise line events that are not removed in the O1 analysis, by comparing all candidate hits to the characteristics of the individual lines identified as noise by O1. The first step is to identify, group, and characterize the coincident events belonging to each individual noise line. The lines are very regular spatially (see Figure 4-1), facilitating the use of SZA as an index for discerning an individual line. Additionally, each event on the instrument, whether dust or noise, is given an equivalent mass based on the amplitude of the signal generated. Using these amplitudes, the differential mass distribution for each individual line is computed. The analysis of the line noise amplitude distributions shows that a single line often has multiple, independent amplitude peaks. An example of the amplitude distribution of one line on channel 8 is shown in Figure 4-3. The mean and standard deviation in mass for all Gaussian mass peaks for each line are computed. Additionally, the mean and standard deviation in SZA are computed for the entire line. The combination of the SZA mean and standard deviation and the Gaussian fits to the noise amplitude distribution is used to characterize each line uniquely.

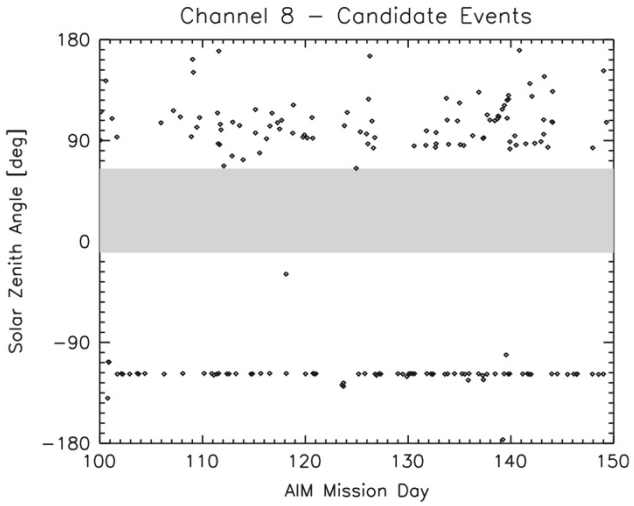

Figure 4-2. Candidate hits on channel 8 for the same time period as Figure 3-1. The Northern Hemisphere noise region has been grayed out for reference. A noise line in the candidate data is still evident at a solar zenith angle of -120°.

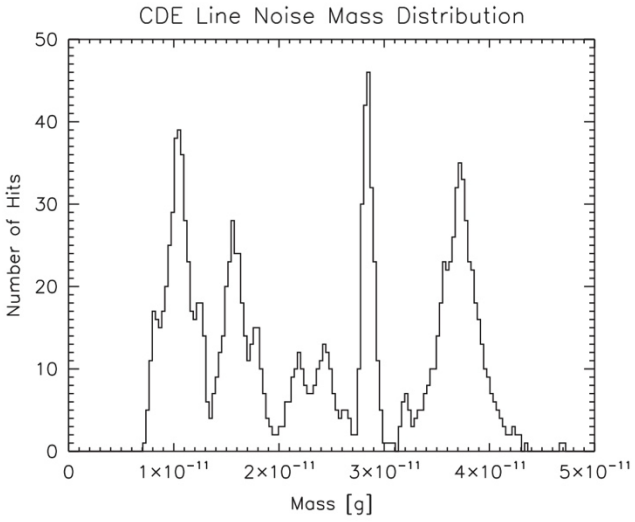

Figure 4-3. Mass distribution for a single noise line on channel 8. Note the presence of several independent Gaussian peaks in the mass distribution.

In order to distinguish between candidate hits that are noise events from candidate hits that are more likely dust impacts, each candidate hit is compared to the characteristics of the nearest line. This comparison is made by using the location and noise amplitude fits of each line. The average and standard deviation of the SZA of the nearest line are used to determine the number of deviations in SZA that the candidate hit is from the nearest line. This value, σ_{SZA}, given by the equation.

$$\sigma_{SZA} = | \alpha_{hit} - \alpha_{avg} | / \sigma_{line,SZA} \quad (4\text{-}2)$$

where α_{hit} is the solar zenith angle of the candidate hit, α_{avg} is the average solar zenith angle of the nearest noise line and $\sigma_{line,SZA}$ is the standard deviation of the solar zenith angle of the line. Similarly, the mass of the candidate hit is compared to the mass distribution of the line, yielding the deviation for the candidate hit mass from the center of the nearest Gaussian mass peak of the line, σ_{mass}, given by

$$\sigma_{mass} = | m_{hit} - m_{avg} | / m_{line,SZA} \quad (4\text{-}3)$$

where m_{hit} is the mass of the candidate hit, m_{avg} is the average mass of the nearest noise line and $m_{line,SZA}$ is the standard deviation of the noise line mass amplitude. An overall index for the candidate hit is obtained by adding the two independent characteristics, σ_{SZA} and σ_{mass}, in quadrature:

$$\sigma_{tot} = (\sigma^2_{SZA} + \sigma^2_{mass})^{1/2} \quad (4\text{-}4)$$

This value is calculated for all the candidate hits, thereby assigning each a probability of belonging to a particular noise line rather than begin a dust impact. Events with low σ_{tot} values are more likely noise, while events with large σ_{tot} values are more likely to be dust impacts.

Once the σ_{tot} parameter has been calculated for all candidate hits, a cutoff in σ_{tot} must be established for each channel, where hits with σ_{tot} values lower than the cutoff are considered noise and hits with σ_{tot} values higher than the cutoff are considered dust impacts. To obtain the σ_{cut} for each channel, the flux for each channel is computed as a function of σ_{cut}, where hits with σ_{tot} values below σ_{cut} are excluded from the calculation. A fit is made to the cumulative flux curve for each channel with the sum of two different functions, one representing the expected noise distribution and the other representing the expected dust distribution as a function of σ_{tot}. For the noise, the distribution is assumed to be Gaussian with respect to σ_{tot}:

$$\Gamma_{noise} = \exp(-\sigma^2_{tot}) \quad (4\text{-}5)$$

The dust is assumed to be independent of the σ_{cut} parameter, and thus the distribution should be a negatively sloped line:

$$\Gamma_{dust} = a - b\,\sigma_{tot} \quad (4\text{-}6)$$

The sum of these two distribution functions is fit to the flux from each channel as a function of σ_{tot}. An example of this type of fit is shown in Figure 4-4 for channel 2. The σ_{cut} value for each channel is determined by the location where the noise portion of the fit falls below 10% of the dust distribution. The candidate hits with $\sigma_{tot} < \sigma_{cut}$ are removed and the remaining hits are identified as the true dust influx signal.

The non-standard nature of the noise algorithm used to extract the dust signal prevents a classical error analysis. Therefore, a detailed study was undertaken of the noise algorithm to

quantify its reliability. Our algorithm has four free critical parameters: (1) the number of days around a candidate hit with which to compare to the nearest noise line; (2) the relative weighting between the σ_{SZA} and σ_{mass} values when calculating σ_{tot}; (3) the number of bins surrounding a peak in the mass distribution with which a Gaussian curve is fit; and (4) the number of relative deviations above the mean mass of a line needed to qualify data as a mass peak. A Monte Carlo analysis was used to verify the sensitivity of our results to these parameters. One hundred random quartets of the parameters were generated and repeatedly run through the entire analysis code. Figure 4-5 shows the total flux for grains with radius, r 4 1:5 mm, as a function of each of the four input parameters, indicating no correlation of the dust flux with any of the parameters. Therefore, the spread in the reported flux values is simply indicative of the statistical accuracy of the algorithm.

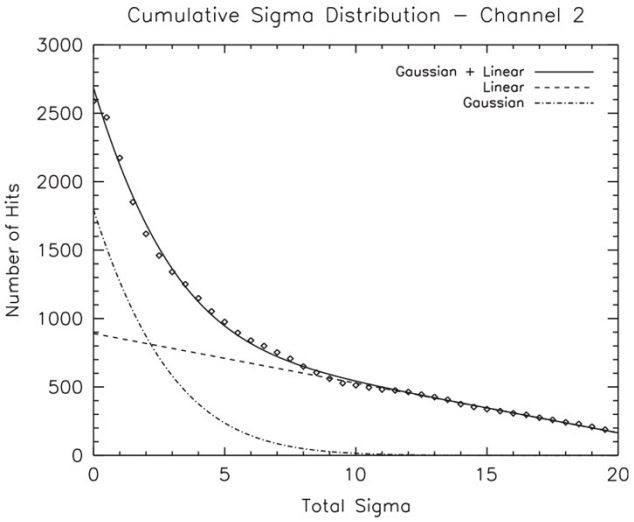

Figure 4-4. Cumulative flux for channel 2 as a function of σ_{tot}. Also shown is the sum of the Gaussian and linear fits, as well as the individual linear and Gaussian terms.

Having eliminated the major noise sources via the algorithms presented above, the leftover events across all channels were considered to be dust impacts on the detectors. While the noise reduction has necessarily introduced additional error in the analysis, the measurement of the terrestrial cosmic dust influx, along with any associated spatial and/or temporal variability, was undertaken and is discussed below.

4.5. CDE Error Analysis and Corrections

Two separate hypotheses were generated to explain the presence of the Northern Hemisphere noise: (1) the pyroelectric nature of the PVDF detectors caused a DC current to flow into the analog electronics, which was then interpreted as false hits, or (2) the detectors were heated during the sunlit portion of the orbit, causing the detector capacitance to increase drastically (shown as a function of temperature in Figure 4-6). Capacitance mis-match between the PVDF detector and the CSA input capacitance is known to cause elevated levels of noise in the detector electronics [*Radeka,* 1974; *Spieler*, 2005; *Horányi*, 2008].

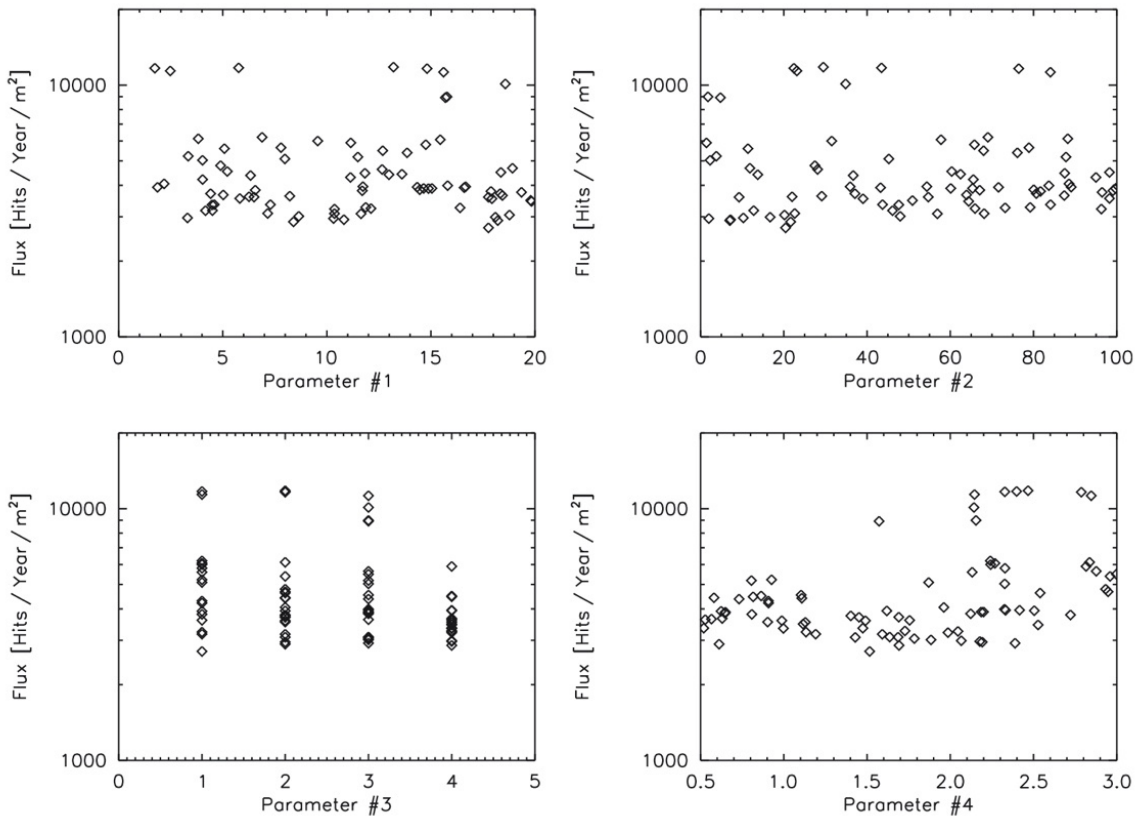

Figure 4-5. Globally averaged influx for r > 1.5 μm as a function of the four parameters studies in the Monte Carlo algorithm analysis. The parameters are: (1) the number of days around a candidate hit with which to compare to the nearest noise line; (2) the relative weighting between the σ_{lat} and σ_{mass} values; (3) the number of bins surrounding a peak in the mass distribution with which a Gaussian curve is fit; and (4) the number of relative deviations above the mean mass of a line needed to qualify data as a mass peak. Note the discrete nature of parameter 3.

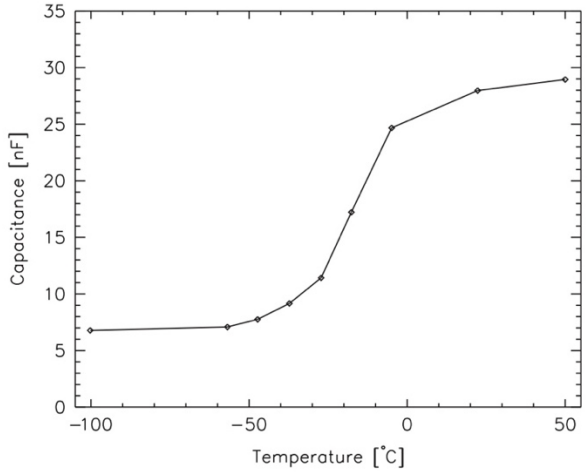

Figure 4-6. The capacitance of a 28 mm PVDF detector as a function of temperature.

In order to investigate and distinguish between these hypotheses, a spare flight detector was mounted to a 0.25 inch aluminum plate that was heated by electric heaters or cooled by thermoelectric coolers and a chiller in order to simulate the orbital thermal environment. The temperature of the detector was measured by using a thermistor attached to the back of the detector. The detector was run through an extended series of heating and cooling cycles to simulate on-orbit temperatures (~ -35 °C < T < ~ 35 °C) while the count rate was simultaneously measured. Figures 4-7 and 3-8 show the measured hit rate as a function of the temperature and the temperature derivative, respectively. As is clearly seen, the noise rate is highly correlated with the detector temperature (and therefore, the detector capacitance) and uncorrelated with the derivative of the temperature. From these results, we conclude that the presence of the northern hemisphere noise is due to the increasing capacitance mis-match between the PVDF detector and the CSA input capacitance. This issue was unfortunately overlooked in the design transfer from the Student Dust Counter, which operated at much colder detector temperatures (T ~ -95 °C), to the Cosmic Dust Experiment, with detector temperatures of -35 °C < T < ~ 35 °C.

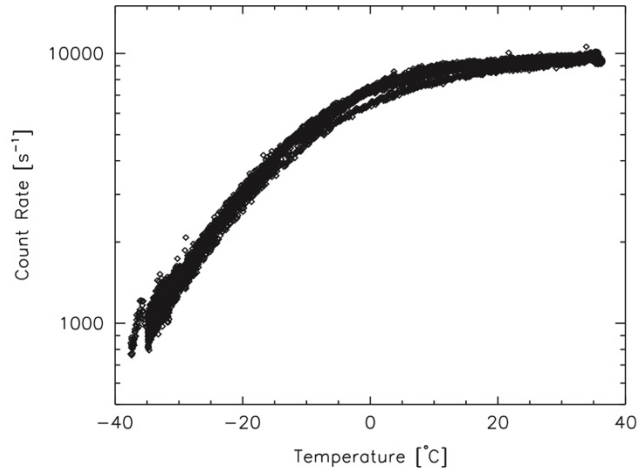

Figure 4-7. The hit rate as a function of detector temperature, demonstrating the highly correlated nature of the count rate with the temperature.

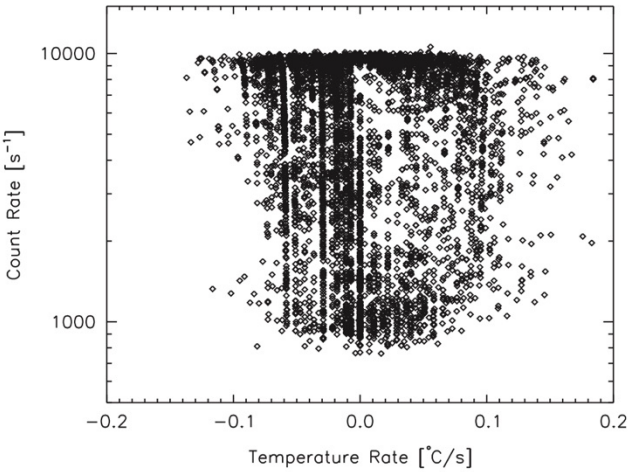

Figure 4-8. The hit rate as a function of the derivative of the detector temperature, demonstrating the uncorrelated nature of the count rate with the derivative of the temperature.

4.6. CDE Calibration

PVDF dust detectors have been extensively tested and calibrated in laboratory experiments [*Simpson et al.*, 1989b] at the Munich and Heidelberg dust accelerators. The available calibration data for 28μm PVDF films are available from *Tuzzolino* [1996]. PVDF films can also be tested using short duration (<μs) laser pulses (λ=337nm). During the Phase A study period, we were able to perform preliminary testing on the 28 μm PVDF film to verify the performance and correct operation of electronics and characterize the overall noise of detector and electronics. During Phase B, we will mount a single patch of the detector on a prototype structure identical to the spacecraft where CDE will be located, using the same methodology employed for flight. This will be taken to the Heidelberg (MPI-Kernphysik, Germany) dust accelerator for final testing and calibration. In Heidelberg the calibration will be performed using both dust impacts and laser pulses. Cross calibrating using both methods enables us to test and calibrate the compliment of flight detectors at LASP with laser pulses only.

4.7. CDE Validation and Results

The flux for each individual channel for grains with radius, r > 1.5 μm are shown in Figure 4-9. The average flux across science detectors is 4.975.5 $\pm 10^3$ m^{-2} yr^{-1} (note that channels 7 and 14 are the background channels and that during this time period, channel 14 measured no impacts with radius, r > 1.5 μm). The variation among channels is indicative of the variation in noise patterns affecting each channels. The average flux measured can also be compared to previous flux measurements as in Figure 4-10. Despite the large amounts of noise across all detectors on the instrument, the reduced data show an averaged flux that is consistent with previous measurements.

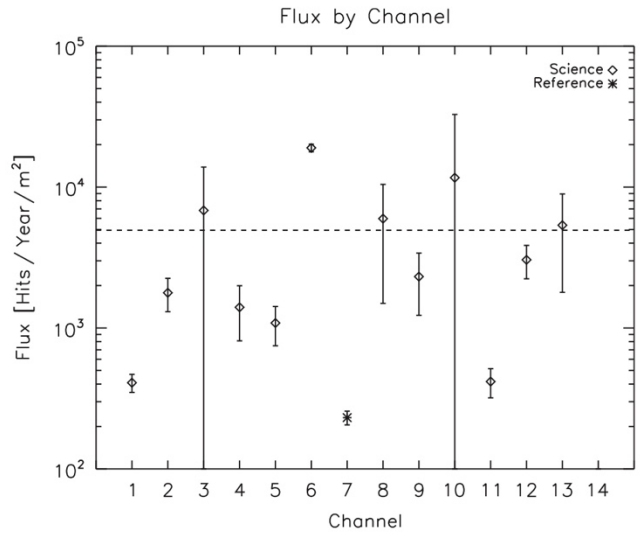

Figure 4-9. Globally averaged influx for each channel for r > 1.5 μm. Science and reference channels are displayed as diamonds and stars, respectively, and the average flux across channels is shown as a dashed line. The error bars represent the variability from the Monte Carlo analysis for each individual channel. Note that channel 14 did not record any hits.

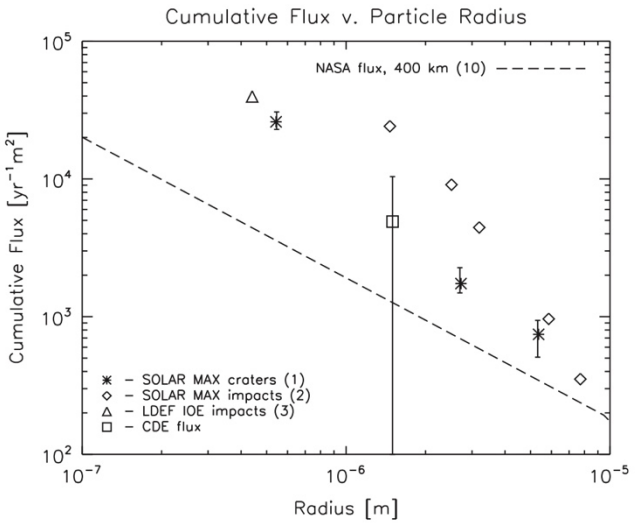

Figure 4-10. Comparison of the mean CDE flux for grains, r > 1.5 μm with previous terrestrial dust measurements. References in the legend: (1) NASA/JSC; (2) *Laurance and Brownlee* [1986]; (3)—Simon et al.; (4) *Bernhard et al.*; (5) *Humes*; (6) *Goldstein and Randolph* (1992); (7) *Thompson et al.* [1992]; (8) *Stansbery et al.* [1995].

One of the main goals of CDE was to measure the temporal and spatial variability of the cosmic dust input. Figure 4-11. shows the globally averaged flux for r > 1.5 μm at monthly intervals. While the error bars remain relatively high, there is evidence of variability throughout the year on the order of a factor of two. Shown in Figure 4-12, the northern hemisphere flux shows a peak around the time of the fall equinox, when the northern hemisphere is most pointed in the Earth's ram direction. Conversely, the southern hemisphere flux shows the beginning of a peak near the vernal equinox, however, the full annual cycle could not be presented due to the safing of the AIM spacecraft in February 2008.

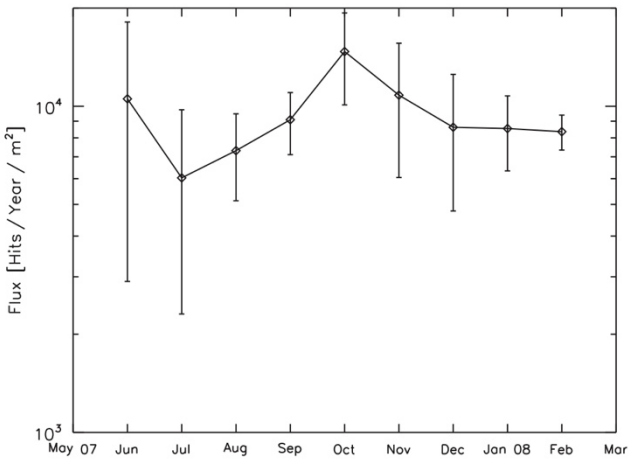

Figure 4-11. Monthly averaged dust fluxes for particles with radius r > 1.5 μm, between June 2007 and February 2008. The error bars represent variability from a Monte Carlo analysis.

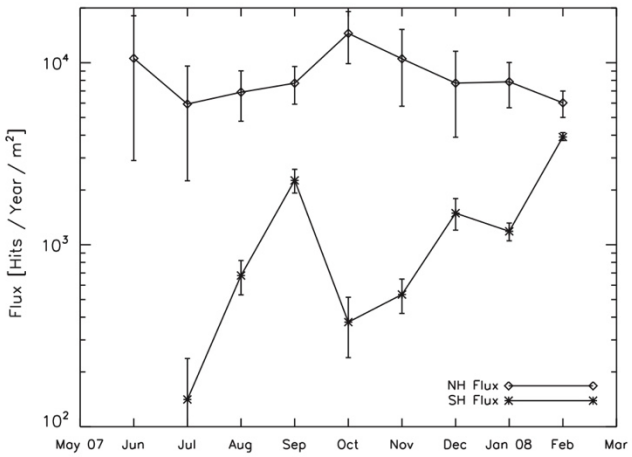

Figure 4-12. Dust flux time series for the northern and southern hemispheres. (Note that no flux was measured in the southern hemisphere in June 2007.)

The spatial variability of the terrestrial cosmic dust influx is detailed in Figure 4-13, where the flux is plotted against the solar zenith angle, α, in 30° bins. The solar zenith angle is measured from the sub-solar point, with 90° and -90° representing the north and south ecliptic poles, respectively. The northern hemisphere noise discussed earlier has prevented analysis of any data within the region, $-10° < \alpha < 60°$. The data show a distinct anisotropy between the northern and southern hemispheres, with the flux entering the northern hemisphere at least an order of magnitude higher than that in the southern hemisphere. This is possibly due to observational limitations, in that the data presented here do not encompass an entire year. It is possible that the southern hemispheric time series peaks during the vernal equinox and thereby balances out the observed latitudinal anisotropy. Previous work including both observation and modeling has predicted such large- scale variability in the sporadic micrometeorite background [*Janches et al.*, 2006]. Unfortunately, due to the limited observation time, CDE cannot confirm or deny such a model, although the data do outline a picture consistent with previous work.

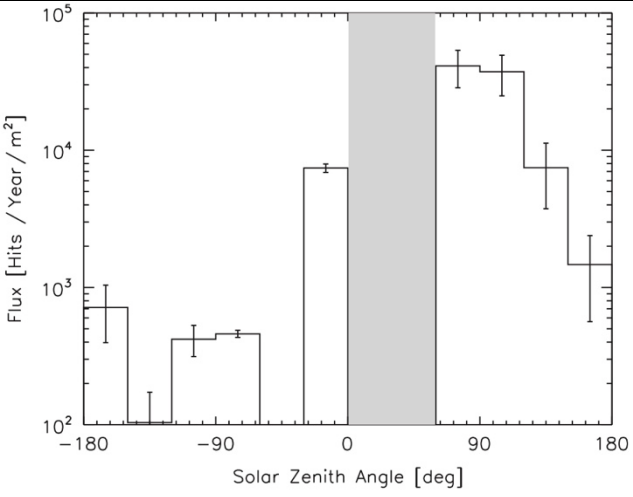

Figure 4-13. Temporally averaged latitudinal flux distribution for particles with radius $r > 1.5$ μm, between June 2007 and February 2008. The error bars represent variability from the Monte Carlo analysis. Saturation from noise events prevented analysis between $-10° < \alpha < 60°$, shown as the grayed portion in the plot.

4.7.1 CDE Comparison with Wind/WAVES

The WAVES instrument on NASA's Wind spacecraft has observed meteoroid ("cosmic dust") impacts in the near-Earth space environment (within $2x10^6$ km) since 1994 [*Malaspina and Wilson*, 2016]. Wind detects dust with radii from ~0.1 - 11 μm [*Malaspina et al.*, 2014], with an average radii thought to be ~1 μm, and thus the measurements are comparable to CDE which detects r > 1.5 μm. CDE Southern Hemisphere (SH) observations during June 2007 - February 2008 are compared to Wind in Figure 4-14. CDE is in reasonable agreement with Wind, having similar meteoroid flux magnitude, and also shows an annual variation that is roughly consistent with Wind. Both CDE and Wind are observing particles with similar radii, although there is some uncertainty regarding the sizes detected for both instruments. Additionally, the comparisons are at different distances from Earth, with CDE in low Earth orbit and Wind near the first Lagrange point (~180 Earth radii), and these difference account for some variations in meteoroid flux.

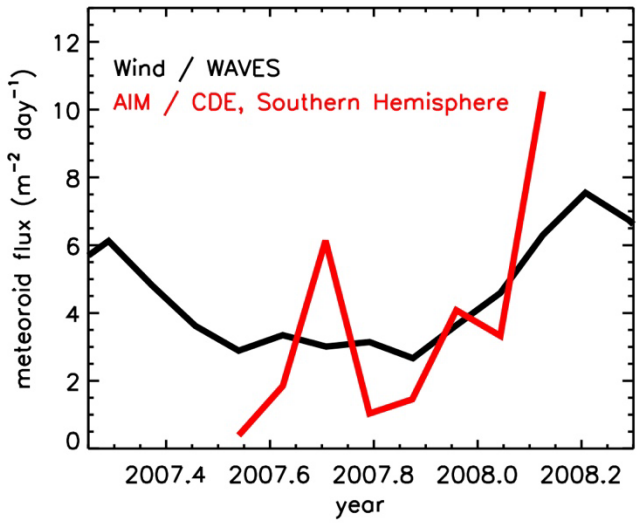

Figure 4-14. Comparison of meteoroid influx from CDE in the SH, with measurements from NASA's HSO Wind spacecraft / WAVES instrument. Wind was near the first Lagrange point during this period.

4.8. CDE References.

Bernhard, R.P., See, T.H., Ho¨rz, F., In: LDEF: 69 Months in Space, pp. 551–573. Cho, J.Y.N., Kelley, M.C., 1993. *Rev. Geophys. 13*, 243–265.

Cho, J. Y. N., and J. Röttger (2001), An updated review of polar mesosphere summer echoes: Observation, theory, and their relationship to noctilucent clouds and subvisible aerosols, *J. Geophys. Res., 102*, 2001-2020, 1997.

Cziczo, D.J., Thomson, D.S., Murphy, D.M. (2001), Ablation, Flux, and Atmospheric Implications of Meteors Inferred from Stratospheric Aerosol, *Science, 291*, 1772–1775, DOI: 10.1126/science.1057737.

Fentzke, J. T., and Janches, D. (2008), A semi-empirical model of the contribution from sporadic meteoroid sources on the meteor input function in the MLT observed at Arecibo, *J. Geophys. Res., 113*, A03304, doi:10.1029/2007JA012531.

Gabrielli, P., C. Barbante, J. M. C. Plane, et al., Meteoritic smoke fallout over the Holocene epoch revealed by iridium and platinum in Greenland ice, *Nature*, 432, 1011, 2004.

Gleghorn, G., Asay, J., Atkinson, D., Flury, W., Johnson, N., Kessler, D., Knowles, S., Rex, D., Toda, S., Veniaminov, S., 1995. Orbital Debris: A Technical Assessment. National Academy Press.

Goldstein, R.M., Randolph,L.W. 1992. IEEE Trans. Microwave Theory Tech. 40, 1077–1080.

Gordley, L. L., M. Hervig, C. Fish, J. M. Russell III, S. Bailey, J. Cook, S. Hansen, A. Shumway, G. Paxton, L. Deaver, T. Marshall, J. Burton, B. Magill, C. Brown, E. Thompson, and J. Kemp, The Solar Occultation For Ice Experiment (SOFIE) (2009), *J. Atmos. Solar-Terr. Phys.*, *71*, 300-315, doi:10.1016/j.jastp.2008.07.012.

Horányi, M., Hoxie, V., James, D. et al. (2008), The Student Dust Counter on the New Horizons Mission, *Space Sci Rev 140*, 387–402. https://doi.org/10.1007/s11214-007-9250-y

Humes, D.H., In: LDEF: 69 Months in Space, pp. 287–322.

Hunten, M. D., R. P. Turco, O. B. Toon (1980), Smoke and Dust particles of meteoric origin in the mesosphere and stratosphere, *J. Atmos. Sci., 37*, 1342-1357.

Horz, F., Brownlee, D.E., Fechtig, H., Hartung, J.B., Morrison, D.A., Neukum, G., Schneider, E., Vedder, J.F., Gault, D.E. (1975), Lunar microcraters: Implications for the micrometeoroid complex, *Planet. Space Sci. 23*, 151–172.

James, D., Hor*á*nyi, M., Hoxie, V. (2010), Polyvinylidene fluoride dust detector response to particle impacts, *Rev. Sci. Instrum.*, 81, DOI: 10.1063/1.3340880.

Janches, D., and J. L. Chau, Observed diurnal and seasonal behavior of the micrometeor flux using the Arecibo and Jicamarca radars, *J. Atmos. Solar Terr. Phys.*, *67*, 1196-1210, 2005.

Janches, D., and D. O. ReVelle, The Initial Altitude of the Micrometeor Phenomenon: Comparison between Arecibo radar observations and theory, *J. Geophys. Res.*, *110*, art. no.-A08307, 2005.

Janches, D., Nolan, M.C., Meisel, D.D., Mathews, J.D., Xhou, Q.H., Moser, D.E. (2003), On the geocentric mictrometeor velocity distribution, *J. Geophys. Res., 108*, 1,222, 10.1029/2002JA009789.

Janches, D., C. J. Heinselman, J. L. Chau, A. Chandran, and R. Woodman, Modeling the micrometeor input function in the upper atmosphere observed by high power and large aperture radars, *J. Geophys. Res.*, *111*, doi:10.1029/2006JA011628, 2006.

Jessberger, E.K., Stephan, T., Rost, D., Arndt, P., Maetz, M., Stadermann, F.J., Brownlee, D.E., Bradley, J.P., Kurat, G., 2001. In: Gru¨n, E., Interplanetary Dust, Springer-Verlag. Kalashnikova, O., Horányi, M., Thomas, G.E., Toon, O.B., 2000. Geophys. Res. Lett. 27, 3293–3296.

Laurance, M.R., and Brownlee, D.E. (1986), The flux of meteoroids and orbital space debris striking satellites in low Earth orbit, *Nature 323*, 136–138.

Leinert, C. (1975), Zodiacal light - A measure of the interplanetary environment, *Space Sci. Rev. 18*, 281–339.

Love, S.G., and Brownlee, D.E. (1991)), Heating and thermal transformation of micrometeoroids entering the Earth's atmosphere, *Icarus 89*, 26–43.

Love, S. G., and D. E. Brownlee (1993), A direct measurement of the terrestrial mass accretion rate of cosmic dust, *Science*, *262*, 550-553.

Lübken, F.-J., and M. Rapp, Modelling of particle charging in the polar summer mesosphere: Part 2 – Application to measurements, *J. Atmos. Solar-Terr. Phys., 63*, 771–780, 2001.

Malaspina, D. M., M. Horányi, A. Zaslavsky, K. Goetz, L. B. Wilson III, and K. Kersten (2014),

Interplanetary and interstellar dust observed by the Wind/WAVES electric field instrument, *Geophys. Res. Lett.*, *41*, 266–272, doi:10.1002/2013GL058786.

Malaspina, D. M. and L. B. Wilson III (2016), A database of interplanetary and interstellar dust detected by the Wind spacecraft, *J. Geophys. Res. Space Physics*, *121*, 9369–9377, doi:10.1002/2016JA023209.

Mathews, J. D., D. Janches, D. D. Meisel, and Q. H. Zhou, The micrometeoroid mass flux into the upper atmosphere: Arecibo results and a comparison with prior estimates, *Geophys. Res. Lett.*, *28*, 1929, 2001.

Megner, L, D. E. Siskind, M. Rapp, and J. Gumbel (2008), Global and temporal distribution of meteoric smoke; a 2D simulation study, *J. Geophys. Res., 113*, D03202, doi:10.1029/2007JD009054.

Murphy, D. M., Thompson, D. S. & Mahoney, M. J., In situ measurements of organics, meteoric material, mercury, and other elements in aerosols at 5 to 19 kilometers, *Science* **282**, 1664-1669 (1998).

Nalwa, H.S., 1995. Ferroelectric Polymers. Marcel Dekker, Inc.

Plane, J.M.C. (2003), Atmospheric Chemistry of Meteoric Metals, *Chem. Rev., 103*, 4963–4984, https://doi.org/10.1021/cr0205309.

Poppe, A., James, D., Jacobsmeyer, B., Horányi, M., 2010. Geophys. Res. Lett. 37.

Poppe, A., Jacobsmeyer, B., James, D., Horányi, M., 2010. Nucl. Instrum. Methods A622, 583–587.

Poppe, A., James, D., Horányi, M. (2011), Measurements of the terrestrial dust influx variability by the Cosmic Dust Experiment, Planetary and Space Sci., 59, 319-326, doi:10.1016/j.pss.2010.12.002.

Radeka, V., 1974. IEEE Trans. Nucl. Sci. 21.

Rapp, M. (2009), Charging of mesospheric aerosol particles: The role of photodetachment and photoionization from meteoric smoke and ice particles, *Ann. Geophys., 27*, 2417–2422.

Rapp, M. and Lubken, F.-J., Modeling of particle charging in the polar summer mesosphere: part 1 – general results, *J. Atmos. Sol. Terr. Phys.*, 63, 759-770, 2001.

Rapp, M., and G. E. Thomas, Modeling the microphysics of mesospheric ice particles: Assessment of current capabilities and basic sensitivities, *J. Atmos. and Solar-Terrestrial Phys.*, doi:10.1016/j.jastp.2005.10.015, 2006.

Rusch, D.W., et. al., The cloud imaging and particle size experiment on the aeronomy of ice in the mesosphere mission: Cloud morphology for the northern 2007 season, Journal of Atmospheric and Solar-Terrestrial Physics (2009),doi:10.1016/j.jastp.2008.11.005.

Russell, J. M. III, S. M. Bailey, M. Horányi, L. L. Gordley, D. W. Rusch, M. E. Hervig, G. E. Thomas, C. E. Randall, D. E. Siskind, M. H. Stevens, M. E. Summers, M. I. Taylor, C. R. Englert, P. J. Espy, W. E. McClintock and A. W. Merkel, Aeronomy of Ice in the Mesosphere (AIM): Overview and early science results, *J. Atmos. Solar-Terr. Phys.*, doi:10.1016/j.jastp.2008.08.011, 2009.

Schwanenthal, J.P., 2004. Debris in-orbit evaluator (DEBIE) calibration and data analysis. Ph.D. Thesis, The Open University.

Simon, C.G., Mulholland, J.D., Oliver, J.P., Cooke, W.J., Kassel, P.C., In: LDEF: 69 Months in Space, pp. 693–703.

Simpson, J.A., Tuzzolino, A.J. (1985), Polarized polymer films as electronic pulse detectors of cosmic dust particles, *Nucl. Instrum. Methods A 236*, 187–202.

Sparks, J. J., and Janches, D. (2009), Latitudinal dependence of the variability of the micrometeor altitude distribution, *Geophys. Res. Lett., 36*, L12105, doi:10.1029/2009GL038485.

Spieler, H., 2005. Semiconductor Detector Systems. Oxford University Press, New York.

Srama, R., et al. (2004), The Cassini Cosmic Dust Analyzer, *Space Sci. Rev. 114,* 465–518.

Stansbery, E.G., Kessler, D.J., Tracy, T.E., Matney, M.J., Stanley, J.F. (1995), Space Debris – The Short Term Orbital Evolution in the Earth Gravity Field, *Adv. Space Res. 16*, 5–16.

Sulzer, M. P. (2004), Meteoroid velocity distribution derived from head echo data collected at Arecibo during regular world day observations, *Atmos. Chem. Phys., 4*, 947–954, https://doi.org/10.5194/acp-4-947-2004, 2004.

Thompson, T.W., Goldstein, R.M., Campbell, D.B. (1992), Radar detection of centimeter-sized orbital debris: Preliminary Arecibo observations at 12.5-CM wavelength, *Geophys. Res. Lett. 19*, 257–259, https://doi.org/10.1029/91GL02772.

Turco, R. P., O. B. Toon, P. Hamill, and R. C. Whitten (1981), Effects of meteoric debris on stratospheric aerosols and gases, *J. Geophys. Res., 86(C2),* 1113–1128, doi:10.1029/JC086iC02p01113.

Turco, R. P., O. B. Toon, R. C. Whitten, R. G. Keesee, and D. Hollenbach, Noctilucent Clouds: Simulation studies of their genesis, properties and global influences, *Planet Space Sci.*, *11*, 1147-1181, 1982.

Tuzzolino, A.J. (1992), PVDF copolymer dust detectors: particle response and penetration characteristics, *Nucl. Instrum. Methods A 316*, 223–237.

Tuzzolino,A.J.,etal. (2001a), The Space Dust (SPADUS) instrument aboard the Earth-orbiting ARGOS spacecraft: I—instrument description, *Planet Space Sci, 49*, 689–703, https://doi.org/10.1016/S0032-0633(01)00012-5.

Tuzzolino, A.J., et al. (2001b), The Space Dust (SPADUS) instrument aboard the Earth-orbiting ARGOS spacecraft: II–results from the first 16 months of flight, *Planet. Space Sci., 49*, 705–729, https://doi.org/10.1016/S0032-0633(01)00013-7.

Tuzzolino, A.J., et al. (2004), Dust Measurements in the Coma of Comet 81P/Wild 2 by the Dust Flux Monitor Instrument, *Science, 304*, 1776–1780.